Redox processes of heme proteins and metalloporphyrins studied by vibrational spectroelectrochemistry

vorgelegt von
Master of Science in Biophysics (M. Sc.)
Patrycja Kielb
geboren in Rzeszów, Polen

von der Fakultät II – Mathematik und Naturwissenschaften
der Technischen Universität Berlin
zur Erlangung des akademischen Grades

Doktor der Naturwissenschaften
- Dr. rer. nat. -

genehmigte Dissertation

Promotionsauschuss

Vorsitzende: Prof. Johannes Teichert
Berichter: Prof. Peter Hildebrandt
Berichterin: Prof. Inez M. Weidinger
Berichter: Prof. Arne Thomas

Tag der wissenschaftlichen Aussprache: 06 Juli 2017

Berlin 2017

ABSTRACT

Heme proteins belong to the most abundant and widely used metallo-proteins throughout the biosphere. Their biocatalytic, electron transporting and oxygen-binding functions are ubiquitous in many life-sustaining reactions. The structure of a heme cofactor and the nature of the heme pocket are determinants of the protein's role and its involvement in metabolic pathways. Immobilized on an electrode, heme proteins often exhibit satisfactory direct electron transfer between the heme and the electrode surface as a prerequisite for potential applications in biolelectronic devices. Synthetic metalloporphyrins constitute an alternative approach for developing efficient electrocatalysts.

Elucidating relationships between structural and redox properties of protein-bound and protein-free hemes is the key task for understanding the molecular functioning and eventually optimizing electrocatalytic performance. In this respect, electrochemical methods together with surface enhanced vibrational spectroscopic techniques represent particularly powerful techniques which were applied in this work for analysing structure-function relationships of two different heme proteins and synthetic cobalt porphyrins.

The hexameric tyrosine-coordinated heme protein (HTHP), for which peroxidase- and catalase-like activity was reported previously, was studied by resonance Raman (RR) and surface enhanced RR (SERR) spectroscopy. The results revealed three different heme redox transitions in the immobilised state. The most negative one is similar to the only transition of the structurally identical six hemes determined in solution. The two more positive redox potentials observed in the immobilised state could be rationalised in terms of qualitatively different modes of interactions with the adsorbens, which may eventually lead to the release of hemes from the protein. This observation as well as structural similarities with heme carrier proteins such as HasA or HmbR point to heme transport as an alternative or additional function.

Cellobiose dehydrogenase (CDH) is a flavocytochrome, catalyzing the oxidation of various carbohydrates. It has been shown that catalytic activity increased upon addition of Ca^{2+} ions. The influence of this effect on the electron transfer rates and structural changes of the heme cofactor and the protein backbone was studied by SERR and surface enhanced infrared absorption (SEIRA) spectroscopy together with electrochemical methods. Addition of Ca^{2+} ions shifted the catalytic turnover signal to more negative potentials while SERR measurements revealed an offset between the potential of heme reduction and catalytic current. Comparing SERR and SEIRA data it was proposed that binding of Ca^{2+} to the heme induces protein reorientation such that the electron transfer pathway of the catalytic FAD center to the electrode can bypass the heme cofactor.

Cobalt hangman porphyrins were analysed by RR and SERR spectroscopies *operando* under catalytic conditions. To understand the role of the hanging group for proton supply, complexes with either a carboxylic acid or ester hanging group were compared. The experimental spectro-electrochemical investigations were accompanied by theoretical calculations, revealing symmetry lowering of the porphyrin during the catalysis. Specifically, the results point to a catalytic Co^{III}-H state intermediate, providing novel insight into the catalytic mechanism.

ZUSAMMENFASSUNG

Hämproteine gehören zu den am häufigsten vorkommenden und am weitesten verbreiteten Metalloproteinen in der Biosphäre. Ihre Funktion als Biokatalysatoren, Elektronentransporter und Sauerstoffträger ist ubiquitär in lebenserhaltenden Prozessen, wobei die Struktur des Häm-Kofaktors und die Beschaffenheit der Bindungstasche maßgeblich ihre Rolle und Mitwirkung in Stoffwechselvorgängen bestimmen. Im immobilisierten Zustand bieten Hämproteine häufig einen sehr guten direkten Elektrontransfer zwischen Häm und Elektrode und somit die Grundvoraussetzung für potentielle bioelektronische Anwendungen. Eine Alternative für die Entwicklung effizienter elektrokatalytischer Systeme bilden synthetische Metalloporphyrine.

Um die Funktionsweise von proteingebundenen und proteinfreien Hämen auf molekularer Ebene zu verstehen und ihre elektrokatalytische Leistung zu optimieren, ist es von zentraler Wichtigkeit, die Zusammenhänge zwischen Struktur und Redoxeigenschaften zu untersuchen. Hierfür stellt insbesondere die Kombination von elektrochemischen Methoden und oberflächenverstärkter Schwingungsspektroskopie eine leistungsfähige Herangehensweise dar, welche in dieser Arbeit angewendet wurde, um Struktur-Funktions-Beziehungen zweier Hämproteine und eines synthetischen Kobaltporphyrins zu untersuchen.

Das hexamere Tyrosin-koordinierte Hämprotein (HTHP), für welches zuvor peroxidase- und katalaseähnliche Aktivitität gezeigt wurde, wurde hier mit Hilfe der Resonanz-Raman (RR) und oberflächenverstärkten RR (SERR – engl. surface-enhanced RR) Spektroskopie untersucht. Hierbei wurden drei Redoxübergänge im immobilisierten Zustand beobachtet, von denen der negativste mit dem Übergang der sechs strukturell identischen Hämgruppen in Lösung übereinstimmt. Die positiveren Redoxpotentiale des immobilisierten Proteins konnten qualitativ verschiedenen Bindungsmodi und Wechselwirkungen mit dem Adsorbens zugeordnet werden, welche schließlich zum Freisetzen des Häms führen können. Die strukturelle Ähnlichkeit mit Hämproteinen HasA und HmbR weist auf eine alternative oder zusätzliche Funktion als Hämtransporter hin.

Die Cellobiosedehydrogenase (CDH) ist ein Flavocytochrom, welches die Oxidation verschiedener Kohlenwasserstoffe katalysiert. Der Einfluss von aktivitätserhöhenden Ca^{2+}-Ionen auf Elektronentransfer und Struktur des Häm-Kofaktors wurde mit Hilfe von SERR, oberflächenverstärkter Infrarotabsorption (SEIRA – engl. surface-enhanced infrared absorption) und elektrochemischen Methoden untersucht. Ca^{2+}-Ionen verschoben das katalytische Umsatzsignal zu negativeren Potentialen, so dass SERR-Experimente einen Versatz des Potentials der Hämreduktion hierzu zeigten. Basierend auf SERR und SEIRA Daten wurde vorgeschlagen, dass Ca^{2+}-Bindung zu einer Reorientierung des Proteins führt und der Elektrontransfer vom katalytischen FAD-Zentrum zur Elektrode den Häm-Kofaktor umgehen kann.

Kobalt-Hangman-Porphyrine mit einer Carboxylat- oder Ester-„hanging group“ wurden mit RR und SERR Spektroskopie unter katalytischen Bedingungen untersucht, um die Rolle dieser Gruppe als Protonlieferant zu verstehen. Mit Hilfe von theoretischen Berechnungen konnte eine Symmetrieerniedrigung während der Katalyse demonstriert werden. Insbesondere erbringt diese Arbeit den Nachweis für einen katalytischen Co^{III}-H Zwischenzustand und somit neue Erkenntnisse über den katalytischen Mechanismus.

PUBLICATIONS

Parts of this work are:

1. Reproduced with permission from **Kielb, P.**, Utesch, T., Kozuch, J., Jeoung, J-H., Dobbek, H., Mroginski, M. A., Hildebrandt, P., Weidinger, I. M. Switchable Redox Chemistry of the Hexameric Tyrosine-Coordinated Heme Protein **2017** *J Phys Chem B*, 121, 3955-3964. Copyright 2017 American Chemical Society. Preprint version.
(Chapter 4.1)
DOI: 10.1021/acs.jpcb.7b01286

   Contributions:
   P. Kielb designed and performed the experiments, especially the UV-Vis, RR, SERR and electrochemical measurements, carried out the data analysis, and wrote the first draft of the paper.
   J-H. Jeoung purified the protein and T. Utesch carried out the molecular dynamics simulations
   All authors equally contributed to the discussion of the results and interpretation.
   P. Kielb, T. Utesch, I. Weidinger and P. Hildebrandt wrote the manuscript.

1. Reproduced with permission from **Kielb, P.**, Sezer, M., Katz, S., Lopez, F., Schulz, C., Gorton, L., Ludwig, R., Wollenberger, U., Zebger, I., Weidinger, I. M. Spectroscopic Observation of Calcium-Induced Reorientation of Cellobiose Dehydrogenase Immobilized on Electrodes and Its Effect on Electrocatalytic Activity **2015** *ChemPhysChem*, 16, 1960-1968. Copyright 2015 Wiley-VCH Verlag GmbH & Co. KGaA. Preprint version.
(Chapter 4.2)
DOI: 10.1002/cphc.201500112

   Contributions:
   P. Kielb designed and performed the experiments, especially UV-Vis, RR, SERR & electrochemistry and SEIRA measurements, carried out the data analysis, and wrote the first draft of the paper.
   R. Ludwig purified the protein.
   All authors equally contributed to the discussion of the results and interpretation.
   P. Kielb and I. Weidinger wrote the manuscript.

Other publications:

1. Kielb, P., Wrzolek, P., Goetz, R., Horch, M., Ly, K.H., Kozuch, J., Schwalbe, M., Weidinger, I.M., *in preparation*

2. Sezer, M., Kielb, P., Kuhlmann, U., Mohrmann, H., Schulz, C., Heinrich, D., Schlesinger, R., Heberle, J.,Weidinger, I.M. *J Phys Chem B* **2015**, 119, 9586-9591

3. Neumann, B., Kielb, P., Rustam, L., Fischer, A., Weidinger, I.M., Wollenberger, U., *ChemElectroChem* **2017**, 4, 1-8

OTHER CONTRIBUTIONS

1. 9th International Conference on Porphyrins and Phtalocyanins, Nanjing, China, July 2016
   Kielb, P., Wrzolek, P., Goetz, R., Ly, K.H., Schwalbe, M., Weidinger, I.M, *Spectroelectrochemistry of biomimetic cobalt hangman complexes during electrocatalytic hydrogen formation and relevance of -COOH group*,
   Poster presentation

2. EMBO Conference on Biocatalysis, Oulu, Finnland, June 2016
   Kielb, P., Wrzolek, P., Goetz, R., Ly, K.H., Schwalbe, M., Weidinger, I.M, *Spectroelectrochemistry of biomimetic cobalt hangman complexes during electrocatalytic hydrogen formation and relevance of -COOH group*,
   Poster presentation

3. 16th European Conference on the Spectroscopy of Biological Molecules, Bochum, Germany, September 2015
   Kielb, P., Gorton, L., Ludwig, R., Zebger, I., Wollenberger, U., Weidinger, I. M., *Combined SERR, SEIRA and electrochemistry to study the influence of calcium on catalysis of cellobiose dehydrogenase immobilized on electrodes*,
   Poster presentation

4. 8th International Conference on Advanced Vibrational Spectroscopy, Vienna, Austria, July 2015
   Kielb, P., Gorton, L., Ludwig, R., Zebger, I., Wollenberger, U., Weidinger, I. M., *Combined SERR, SEIRA and electrochemistry to study the influence of calcium on catalysis of cellobiose dehydrogenase immobilized on electrodes*,
   Oral presentation

5. ICIQ-UniCat Summer School, Berlin, July 2015
   Kielb, P., Gorton, L., Ludwig, R., Zebger, I., Wollenberger, U., Weidinger, I. M., *Combined SERR, SEIRA and electrochemistry to study the influence of calcium on catalysis of cellobiose dehydrogenase immobilized on electrodes*,
   Poster presentation

6. SERS Round Table Meeting, Duisburg, Germany, March 2015
   Kielb, P., Gorton, L., Ludwig, R., Zebger, I., Wollenberger, U., Weidinger, I. M., *Combined SERR, SEIRA and electrochemistry to study the influence of calcium on catalysis of cellobiose dehydrogenase immobilized on electrodes*,
   Oral presentation

7. Workshop of Bioelectronics, Erice, Italy, May 2014
   Kielb, P., Gorton, L., Ludwig, R., Zebger, I., Wollenberger, U., Weidinger, I. M., *Combined SERR, SEIRA and electrochemistry to study the influence of calcium on catalysis of cellobiose dehydrogenase immobilized on electrodes*,
   Poster presentation

Contents

ABBREVIATIONS

RR	resonance Raman
SERR	surface enhanced resonance Raman
DET	direct electron transfer
HTHP	hexameric tyrosine-coordinated heme protein
CDH	cellobiose dehydrogenase
FAD	flavin adenine dinucleotide
HET	heterogeneous electron transfer
ET	electron transfer
ORR	oxygen reduction reaction
HER	hydrogen evolution reaction
UV-Vis	ultraviolet-visible
HOMO	highest occupied molecular orbital
LUMO	lowest unoccupied molecular orbital
IR	infrared
SEIRA	surface enhanced infrared absorption
SER	surface enhanced resonance
LPR	localized plasmon resonance
5cHS	five coordinated high spin
6cHS	six coordinates high spin
6cLS	six coordinated low spin
SAM	self-assembled monolayer
MUA	11-mercaptoundecanoic acid
MPA	3-mercaptopropionic acid
CV	cyclic voltammetry
PDADMAC	Polydiallyldimethylammonium chloride
ATR	attenuated total reflection
CG	coarse grained
MD	molecular dynamics
IET	internal electron transfer
GO	glucose oxidase
HRP	horse radish peroxidase
ADH	alcohol dehydrogenase
SOD	superoxide dismutase
NHE	normal hydrogen electrode
DMF	dimethylformamide
SCE	saturated calomel electrode
DFT	density functional theory
FTIR	Fourier transform infrared

I. INTRODUCTION

Heme proteins are ubiquitous in many life-sustaining reactions. They exhibit a great variety of function which is a result of their tunable redox chemistry. The heme structure provides broad possibilities of binding and a redox conversion of substrates or transporting electrons. It has been shown through many examples that the structure of the heme cofactor and its surrounding are key features defining the protein's function. In immobilized state, heme proteins often establish the direct electron transfer (DET) between an electrode and the cofactor. This possibility is especially attractive in investigating heme enzymes used in the development of biodevices in which high DET rates with preserved biocatalytic activity are prerequisites for satisfactory biosensors or biofuel cells. Nowadays, extensive research on porphyrins resulted not only on expanded knowledge of natural heme proteins but also powered biomedical and technological applications. However, despite promising examples, the application of enzymes in industrial processes is often challenging. Hence, synthetic, biomimetic compounds mimicking active sites of enzymes were developed to bypass cheaper and more stable alternatives.

Understanding structure-function relationship of heme proteins requires the use of several techniques to determine the detailed structure of the heme group and the functionality of the protein. Among different methods used in molecular biophysics to elucidate structural information, vibrational spectroscopy stands out for its sensitivity, high resolution and the possibility of investigaiting biomolecules in their native environment. Furthermore, by immobilizing heme proteins, combining electrochemical methods with surface enhanced vibrational spectroscopy provides a unique way of detecting the heme redox-related structural changes. Electrochemical techniques give valuable information about electrocatalytic performance and potential of a redox couple. Surface enhanced resonance Raman (SERR) techniques offer a way of determining a vibrational pattern of the porphyrin macrocycle of respective redox states. Like RR, SERR selectively probes only the porphyrin modes which carry the information about iron coordination, oxidation and spin state. The structure of the heme and thus its porphyrin modes can be further influenced by interactions of second coordination sphere formed by distal amino acids and water molecules. The heterogenous electron transfer rate (HET) between heme and an electrode surface can be obtained in time-resolved combined SERR and electrochemical experiments. Finally, surface enhanced infrared absorption spectroscopy probes the protein backbone amide modes and thus possible changes of the secondary structure.

In this work, the combination of electrochemical and surface enhanced vibrational methods has been employed to analyse two different heme proteins: hexameric tyrosine coordinated heme protein HTHP and cellobiose dehydrogenase CDH, and synthetic cobalt hangman porphyrin compounds.

In the first part of this work the combination of methods is used to determine the redox-centered structural changes of the heme cofactors in the hexameric tyrosine coordinated heme protein (HTHP). The protein crystal structure was investigated previously and revealed barrel-shaped hexameric structure with six solvent exposed hemes distributed symmetrically over a ring within the protein. Previous electrochemical experiments have shown DET with the electrode and a peroxidase- and a catalase-like activity. In this work, further detailed potential-dependent spectroscopic studies were undertaken to elucidate the correlation between heme structure and the protein function.

In the second part of this work the investigations focus on the influence of ionic strength and calcium ions on the catalytic performance and heterogeneous electron transfer (HET) rate of cellobiose dehydrogenase (CDH) from *Myriococcum thermophilum* (*Mt*CDH). CDH is a flavocytochrome constituted by a large FAD-containing domain and a smaller heme-containing domain. It oxidizes a variety of carbohydrates and was found to play a significant role in a wood degradation. Due to its high substrate specificity and partially exposed heme cofactor promising a good electron transfer with a potential electron acceptor like electrode surface, it was recognized as a good biocatalyst in the development of biosensors. It was previously shown, that calcium ions may significantly increase the catalytic rate of lactose oxidation, when immobilized on the electrode. Increased ionic strength conditions may result in higher protein flexibility when electrostatically attached to the surface and thus provide proper protein orientation for ET rates. In this work, investigations were undertaken to specify the effect of calcium ions on the HET rate between heme and the electrode and monitor overall protein structural dynamics.

The third part of this work focuses on investigating synthetic cobalt hangman porphyrins during electrocatalytic hydrogen evolution reaction. Metal porphyrins gained a particular interest in recent years as promising electrocatalysts which can overcome drawbacks of the use of biocatalysts in technological applications. Hangman porphyrins represent a catalytic center comprising the metal site responsible for redox chemistry and functional hanging group positioned just above the metal ion serving as proton relay. Their tunable redox properties are particularly useful in performing proton-coupled electron transfer reactions. Cobalt as a metal center offers the possibility of being at low oxidation states from which the proton can be

reduced to hydrogen. Electrochemical measurements have shown that the compounds can work at different potentials. In this work, complementary studies investigate the structure of compounds and their intermediates under catalytic conditions.

II. THEORETICAL PART

2.1 Heme proteins and porphyrins

The most known protein cofactors are hemes. Their structure comprises the porphyrin macrocycle consisting of four pyrrole rings connected to each other by methine bridges. (Figure 2.1). [1] Two pyrrole rings carry propionic acid side chains, whereas the other two bear vinyl groups. In the classical nomenclature, which will be used throughout this dissertation, carbons of pyrrolic rings are labeled α and β and the 'interpyrrolic' methine positions are named *meso*.[2] Although in biosynthetic pathways, this structure is converted into different porphyrin derivatives, they are all based on the type of porphyrin isomer depicted in Figure 2.1.[1]

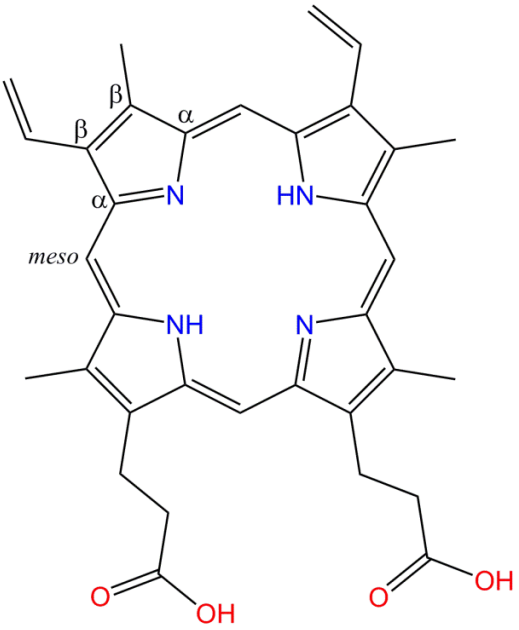

Figure 2.1 Structure of protoporphyrin IX.

Such a macrocyclic structure implies the possibility of metalation of different atoms, which are coordinated by four pyrrolic nitrogens.[3] In natural biological molecules, the protoheme incorporates an iron ion in case of cytochromes, a magnesium ion in chlorophylls, or a cobalt ion in vitamin B_{12}. Metal coordination provides the possibility of chelated metal redox chemistry and enzymatic catalysis. In addition, the peripheral positions of the macrocycle can be substituted with various side-chains. For instance, cytochrome *b* is a protoheme (as in the figure), in cytochrome *a* one of the vinyl group is converted into formyl, whereas in cytochrome *c* the two vinyl groups are used for covalent linkages to cysteine side, leading to thioether functional groups. In heme proteins, the different types of hemes are related to specific functions.[4,5] For instance, in the group of cytochromes a, cytochrome c oxidase is the most

famous protein containing heme a and a_3 being directly involved in process of cellular respiration taken place in the membrane of mitochondria. Cytochromes b are widely spread in both plants and animals and their functions are quite different. Some of them are electron carriers like cytochrome b_5, anothers play a significant role in metabolism or drug detoxication like cytochrome P450 or oxygen transport like myoglobin and hemoglobin. Cytochromes c are biologically significant in many metabolic pathways requiring an electron transport, like cellular respiration, photosynthetic processes, nitrate or sulphate reduction.

In synthetic chemistry, porphyrin complexes offer an impressive array of applications as models for biological electron transport or biocatalytic reactions. The metal core serves as reactive active center responsible for performing a desired reaction (Fig. 1.2). Additional substituents at C_{meso} positions of pyrrole rings can further tune the redox properties of a compound, whereas substituents at C_{β} positions can modify their molecular flexibility.[6]

2.1.1 Redox chemistry of porphyrins and their application in catalysis

Metalloporphyrins offer an array of rich redox chemistry. Upon metal coordination by the porphyrin, two protons from pyrrolic nitrogens are removed leaving the porphyrin with two negative charges. When the metal ions are chelated, a center for electron acceptance/donation is generated and the total net charge of compound changes. Different porphyrin derivatives can incorporate different metal atoms like Co, Fe, Zn, Mg. Depending on the oxidation state, they further axially coordinate ligands resulting in a formation of either pentacoordinated complexes with a square-pyramidal structure or hexacoordinated complexes with octahedral structure.[7] Many parameters affect the redox properties of metalloporphyrins and thus can tune the redox potential of the macrocycle involved in the catalytic reaction. The most important ones are: the nature of axial ligands that coordinate the metal center, the second coordination sphere of the porphyrin pocket and its electrostatic interactions, porphyrin solvation and peripheral substituents.[8–10] In the case of heme proteins, where the protein fold provides an additional key factor for constituting the redox properties, the range of redox potentials is spanned from +0.2 V to -0.6 V [11]. The structural parameters that control the redox potential can be generally divided into three levels of heme environment (Figure 2.2). The first coordination sphere includes proximal axial ligations and porphyrin substituents. For instance, the former often determines the type of catalyzing reaction and thus, frequently hexacoordinated His/His or His/Met low spin heme protein are involved in electron transport, Tyr coordination is preserved

in catalases and heme transporting proteins and Arg ligands in peroxidases [8,11–1314]. Porphyrin substituents can differ in different types of cytochromes (a, b and c) as discussed before. Additionally, peripheral substituents at meso carbon position might preferably tune redox properties of metal center or induce porphyrin deformations.[15,16] The second sphere involves the heme pocket. It consists of distal amino acids and creates a proper electrostatic or hydrophobic environment. Hydrogen bond interactions are also often crucial to control redox properties. Additionally, the presence of neighboring amino acids may provide an additional proton relay for proton-coupled electron transfer reactions. The porphyrin solvation is another important factor which was found to affect the reduction potential.[17] Finally, the overall heme pocket environment with its polar and nonpolar interactions ensures heme functionality.[10] For instance, when hydrophobic residues present in heme pocket of human myoglobin and cytochromes are substituted, the redox potential may change by 400 mV.[18]

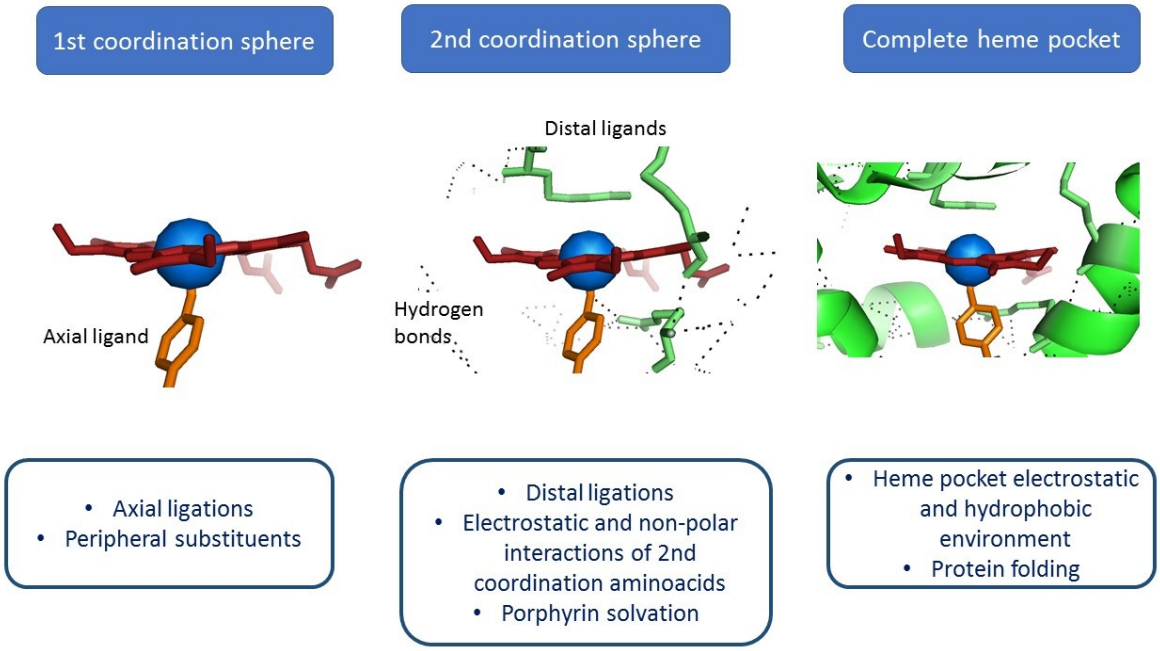

Figure 2.2 Parameters influencing redox chemistry of heme proteins (case, HTHP, pdb id: 2OYY) divided into three levels: first and second coordination sphere of the porphyrin macrocycle and complete heme pocket. Strucutral features constituting each level are listed.

Among various heme enzymes, we can distinguish between those participating in oxidative and others in reductive redox reactions. Enzymes catalyzing oxidation reactions could be in general divided into oxygenases and peroxidases. The first group uses oxygen to oxidize substrates, whereas the second group uses hydrogen peroxide.[4] In the first class, cytochrome P450 is a good example of an enzyme, in which oxygen binds to the ferrous (Fe^{2+}) cysteine-coordinated heme and thus leads to the formation of an oxo intermediate. This intermediate is

later transformed into so called compound I which oxygenates the substrate.[19] This reaction found a particular interest in applications for drug metabolism and gained great interest in medical research.[20] In the second group, peroxidases utilize hydrogen peroxide to oxidize different substrates. The mechanism occurs also via formation of compound I and hydrogen peroxide is reduced to water, either in a peroxidatic reaction or upon addition of an additional hydrogen peroxide.[21] In the class of reductive enzymes, cytochrome c oxidase is a good example of an enzyme catalyzing oxygen reduction. The reaction requires four electrons and four protons to achieve a fully reduction to water. The process bears the risk of forming highly reactive oxygen species, therefore a very precise machinery of electron and proton delivery must be achieved, which is afforded by the proper arrangement of hemes versus protein backbone.[22–24]

Up to now, extensive research on porphyrins resulted not only in an expanded knowledge of cytochromes but also promoted their use in biomedical and technological applications. Prospects of biocatalytic reactions were used in the development of bio-devices like biosensors or biofuel cells. In the first case, a biological recognition element is directly connected to a signal transducer, which then determines the concentration of an analyte. Similarly, in the latter case, enzymes catalyzing a certain reaction provide an electron source, which can be further exploited in a fuel cell.[25–28] However, using cytochromes in bioelectronic devices is asscociated with some drawbacks. Particularly, active sites are often buried deeply inside the protein hindering electronic communication with an electrode. In the field of biosensors, heme proteins gained a strong interest as they can provide direct electron transfer with the electrode in so called third class of biosensors.[29] Hence synthetic, biomimetic compounds mimicking active sites of enzymes without protein matrix were developed to bypass these disadvantages. Hangman porphyrin complexes are particularly interesting providing rationally designed structures with metal center responsible for electron transfer and functional hanging group positioned just above metal center providing a proton relay.[30,31] Small size of these compounds and lack of additional surrounding structure are key features which allow establishing good electronic communication with an electrode in an electrode-attached state. The Hangman motif is especially attractive for promoting proton-coupled electron transfer reactions.[32,33] Depending on the redox transitions of chelated metals in hangman construct they can be efficient for different reactions, like oxygen reduction reaction (ORR), hydrogen evolution reaction (HER), CO_2 reduction or water oxidation.[33–37] The most common metals that are inserted in these constructs are iron, cobalt, copper and nickel. A similar concept is used in Pacman constructs, which consist of two bifacial metalloporphyrins. The motif was inspired by the structure of

cytochrome c oxidase active site consisting of a heme-copper center. Such a compound was particularly studied for the oxidation reactions which require proper subsequent electron delivery.[38,39]

Another example of syntethic metalloporphyrins are catalysts with ruthenium, iron or manganese, which are efficient to mediate C-H oxidations with high selectivity and good yields.[40]

2.2 Absorption Spectroscopy

Upon absorption of light by molecules, electrons can be promoted from the electronic ground to the excited state, if the energy of incident photons equals the energy difference between these two electronic states. Subsequently, electrons from the excited state can either return to the ground state by emitting heat or radiation of energy equal or smaller (fluorescence) than the absorbed radiation.[4142] The amount of absorbed light by the sample is determined by ratio of incident and radiated light intensity, using Beer-Lambert law (2.1), where A denotes absorbance, I_0 intensity of incident light, I intensity of the transmitted light, ε is absorbance coefficient, c concentration of the sample, and l corresponds to the thickness of the sample.

$$A = log\frac{I_0}{I} = \varepsilon cl \tag{2.1}$$

Absorption spectra of hemes exhibit a very characteristic pattern and act as a tool of predicting basic parameters of iron oxidation or coordination state. Altering the heme environment results in altering the electronic energy levels of the molecule with consequences for the absorption spectra (Figure 2.3).

The porphyrin macrocycle is a highly conjugated system with 22 π-electrons, but only 18 of these are included in electron delocalization. This number confirms Hückel's 4n + 2 aromaticity rule. Porphyrins are colored with a very high extinction coefficients for the main π-π^* porphyrin electronic transition.[43] The absorption spectrum of heme consists of characteristic Soret (at *ca.* 400 nm) and Q (at *ca.* 550 nm) bands (Figure 2.3). The first one is the result of the transition to the second excited state ($S_0 \rightarrow S_2$) whereas the second one refers to the transition to first excited state ($S_0 \rightarrow S_1$). Soret band transitions are much more intense than Q bands and it can be explained on basis of the Gouterman Four-Orbital model.[44] In this

theory, electronic transitions in the porphyrin arise from mixing of two HOMO and two LUMO states into new states of higher (Soret band) and lower (Q band) energy and oscillator strength.

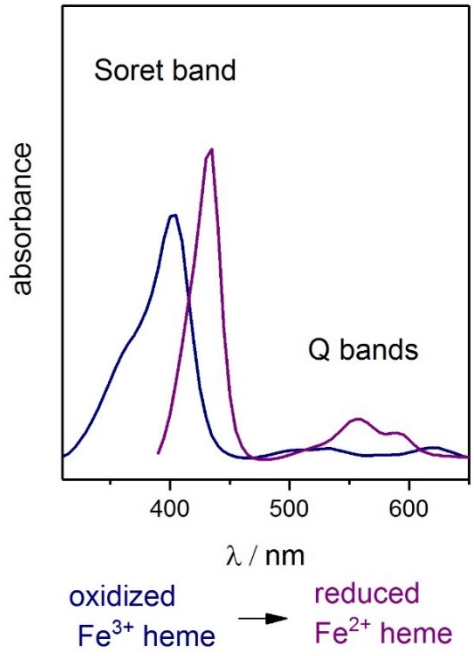

Figure 2.3 Absorbance spectra of HTHP heme protein showing electronic transitions of oxidized and reduced porphyrin macrocycle.

2.3 Vibrational Spectroscopy

Vibrational spectroscopy is a technique providing a detailed information about studied molecule's chemical and physical nature.[45] Vibrational transition can be excited in two ways, either by employing infrared absorption spectroscopy or Raman spectroscopy. In the first case, the molecule is exposed to a continuum of IR radiation and only photons are absorbed which are matching a specific transition. Raman spectroscopy is based on inelastic scattering of monochromatic light by the molecule.[46]

2.3.1 Molecular vibrations as harmonic oscillations

Molecular vibrations can be explained based on classical mechanics using a concept of harmonic oscillators where two point masses representing atoms are connected to each other by a spring representing a chemical bond. In this manner, the molecular vibration is expressed as a spring's oscillation. Displacement (motion) of an atom from its equilibrium position x_0 is driven by experiencing a restoring force F_x, depicted in Figure 2.4. This force is proportional to the displacement x and is governed by equation (2.2), where *k* is the force constant of the spring.

Figure 2.4 Harmonic oscillator. F_x represents restoring force and x_0 represents an initial position of an atom.

$$\vec{F}_x = -k\vec{x} \tag{2.2}$$

The motion of atoms in response to this restoring force can be expressed based on Newton's laws. Total energy E of the system is conserved which means that at any time summation of kinetic T and potential energy V of the atoms equals zero (2.3). The total net force acting on the atom in an inertial frame is equal to zero.

$$\frac{dE}{dt} = \frac{dT}{dt} + \frac{dV}{dt} = \frac{1}{2}\frac{d\dot{x}^2}{dt} + \frac{1}{2}k\frac{dx^2}{dt} = 0 \tag{2.3}$$

This is expressed as second derivative of displacement of an atom with respect to time and is called Newton's equation of motion (2.4), where μ represents the reduced mass of two atoms.

$$\frac{d^2x}{dt^2} + \frac{k}{\mu}x^2 = 0 \tag{2.4}$$

A solution of this equation is given by the trigonometrical function 2.5 with the circular frequency ω dependence on the force constant of the spring k and the reduced mass (2.6).

$$x = Acos(\omega t + \varphi) \tag{2.5}$$

$$\omega = \sqrt{\frac{k}{\mu}} \tag{2.6}$$

The frequency divided by speed of light c defines frequency ν in wavenumbers (cm^{-1}). Integration into equation 2.6 leads to the following expression (2.7).

$$\tilde{\nu} = \frac{\omega}{2\pi c}\sqrt{\frac{k}{\mu}} \tag{2.7}$$

This formula explains how the frequency of the oscillation is proportional to the strength of the bond and reversely proportional to the reduced mass of atoms.

2.3.2 Normal modes and Internal Coordinates

It is easy to imagine the harmonic oscillation of two atoms governed by Newton's laws of motion, where atoms move forward and backward with respect to each other. The situation gets already more complicated if we consider a triatomic nonlinear molecule like water. In such a model not all of the possible displacements of atoms to all three, x,y,z directions in the Cartesian system, are correlated with the vibration of the bond. In general, each atom has 3 degrees of freedom. For a nonlinear molecule, three of them refer to translation and another three to rotation of the molecule. Therefore, a nonlinear molecule with N atoms exhibits 3N-6 vibrational degrees of freedom, whereas a linear molecule contains 3N-5 vibrational degrees of freedom. These oscillations constitute to different patterns of atomic motions as well-defined collective vibrations called normal modes. Hence, normal modes are specific and characteristic of a given molecule.

For each 3N degrees of freedom applying Newton's equation of motion leads to 3N frequency solutions for circular frequency ω corresponding to 3N frequencies (2.8), where q_i refers to mass-weighted Cartesian displacement coordinate (2.9).[47]

$$q_i = A_i cos(\sqrt{\omega} t + \varphi) \tag{2.8}$$

$$q_i = \sqrt{m_i}\Delta x_i \tag{2.9}$$

Although coordinates in the Cartesian system are well defined, for the purpose of extracting all information of a certain normal mode, they are transformed into normal coordinates Q_k via orthogonal transformation (2.10), where l_{ik} is a transformation coefficient. This leads to the transformed Newton's equation of motion (3.10)

$$Q_k = \sum_{i=1}^{3N} l_{ik} q_i \tag{2.10}$$

$$Q_k = K_k \cos(\sqrt{\omega_k} t + \varphi) \tag{2.11}$$

In order to express coordinates of molecules and their vibrations in an intuitive manner, where a character of the vibration can be defined as an expression of their structural parameters like bond lengths or angles, normal coordinates are transformed into internal coordinates. In this system, displacement of each atom α is defined by a vector ρ_α which is related to internal coordinate S_t according to (2.12).

$$S_t = \sum_{\alpha}^{N} \overrightarrow{s_{t\alpha}} * \overrightarrow{\rho_\alpha} \tag{2.12}$$

For a molecule with 3N-6 degrees of freedom, a complete set of stretching, bending, out-of-plane deformations and torsional coordinates sum up to a total of 3N-6 independent normal modes. In order to obtain solutions of Newton's law of motion, secular equations are derived as expression for kinetic and potential energy involving so-called FG matrix elements. The final frequencies are given by (2.13).

$$\tilde{\nu} = \frac{1}{2\pi c} \sqrt{\omega} \tag{2.13}$$

2.3.3 Infrared Spectroscopy

Infrared spectroscopy measures vibrational modes of atoms as a result of direct absorption of photons that match the energy difference between the vibrational ground and excited state (see Figure 2.6). The mechanism is based on the interaction between the electric field vector of the radiation and the electrical dipole moment $\widehat{\mu_q}$ of the molecule (2.14), where e_α denotes charge of an atom α and r_α represents its Cartesian vector.

$$\widehat{\mu_q} = \sum_{\alpha} e_\alpha \cdot r_\alpha \tag{2.14}$$

However, for a vibrational mode to become IR visible, the transition dipole moment M_{ij} for a certain molecule (Eq. 2.15), which integrates all possible orientations in the Cartesian system, must change.

$$M_{ij} = \left\langle \psi_i \middle| \widehat{\mu_q} \middle| \psi_j \right\rangle \tag{2.15}$$

This implies two selection rules for IR activity of a normal mode. First, there must be a change in dipole moment $\widehat{\mu_q}$ associated with the normal mode and second, the vibrational quantum numbers i, j must differ by 1 within the harmonic approximation.

2.3.4 Raman Spectroscopy

The 'Raman effect' was first discovered in 1928 by Raman and Krishnan.[48,49] The potential of this effect was realized very rapidly and opened up new studies of light-scattering. Now, this phenomenon is well understood and we know that for monochromatic light shining on a molecule, the majority of scattered light remains unchanged (Rayleigh scattering) with the same incident frequency ν_0, but a small amount of scattered light's is shifted in frequency ($\nu_0 \pm \nu_C$) due to an interaction of electromagnetic waves and the electronic cloud of a molecule (Figure 2.5) The electric field of incoming light induces the electric dipole moment in a molecule, which than depends on the polarizability of the electron cloud. This may result in exciting vibrational transitions and scattered light of lower energy (Stokes radiation), whereas, for the transition to lower vibrational energy levels, scattered light may gain an energy (anti-Stokes scattering).

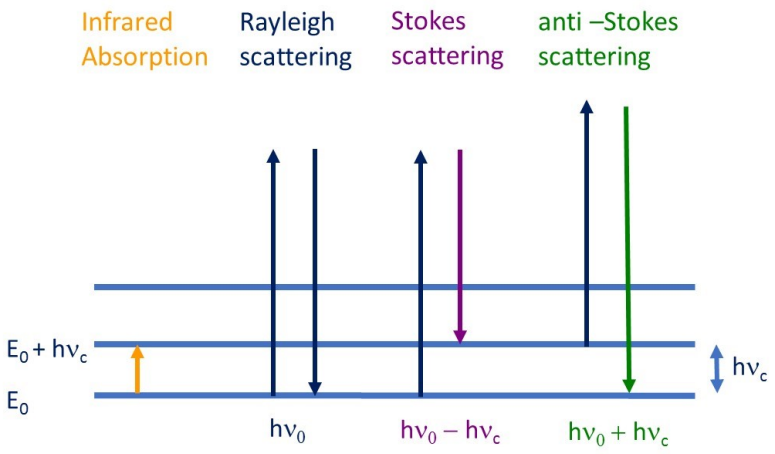

Figure 2.5 Simplified energy diagram representing vibrational energy levels (depicted by blue lines) of a molecule and its absorption of light or interaction with light, with emphasized frequencies of scattered Rayleigh and Raman radiation.

The magnitude and the direction of induced dipole moment of a molecule with an electric field $\vec{E}$ of an electromagnetic wave:

$$\vec{E} = \overrightarrow{E_0}\cos(2\pi\nu_0 t) \tag{2.16}$$

This dipole moment changes with time, as a response of nuclei oscillating with the normal mode frequency ν_C, and is given by polarizability tensor $\alpha(\nu)$. Thus, induced dipole moment P oscillates in an applied field according to (2.17).

$$\vec{P} = \overrightarrow{E_0}\left[\alpha_0\cos(2\pi\nu_0 t) + \left(\frac{\partial\alpha}{\partial Q_k}\right)_0\cos[2\pi(\nu_0+\nu_C)t) + \left(\frac{\partial\alpha}{\partial Q_k}\right)_0\cos[2\pi(\nu_0-\nu_C)t)\right] \tag{2.17}$$

In this expression, the first term describes polarizability correlated to Rayleigh scattering where the oscillating frequency ν_0 of scattered light stays unchanged. In the last two terms, induced dipole moment has changed oscillating frequency ($\nu_0 \pm \nu_C$), and they refer to anti-Stokes scattering and Stokes scattering, respectively (Figure 2.6). As mentioned before, in this way a molecule can stay either on a higher energetically vibrational level or on a lower one.

In general, just the molecules for which any component of polarizability tensor is changed upon vibration or rotation will be visible in the Raman spectrum, and are referred to as Raman active.

The intensity of Raman scattering I_R is proportional to the square of the induced dipole moment (2.18)

$$I_R \propto \alpha(\nu)^2 * \vec{E}^2 \tag{2.18}$$

This intensity is directly correlated to probability of transition from one vibrational state to another. Classical treatment of energy conservation of some of the molecular vibrations is inadequate. Therefore, quantum mechanical treatment has to be introduced in order to properly describe Raman scattering on a molecular level.[50] It begins with introducing the Raman cross section σ (2.19 and 2.20).

$$\sigma \propto (\nu_0 \pm \nu_C)^4 * \alpha(\nu)^2 \tag{2.19}$$

$$I_R \propto \sigma * I_0 \tag{2.20}$$

Finally, using quantum mechanics the scattering tensor is expressed using Kramers-Heisenberg-Dirac's theory and has the form (2.21), where Γ is a damping factor and M is the electronic transition dipole moment of a molecule in a fixed coordinate system σ,ρ.

$$\alpha_{nm} = \frac{1}{h}\sum_{R,r}\left(\frac{\langle nG|M_\rho|Rr\rangle\langle rR|M_\sigma|Gm\rangle}{\nu_{Rr} - \nu_C - \nu_0 + i\Gamma} + \frac{\langle nG|M_\sigma|Rr\rangle\langle rR|M_\rho|Gm\rangle}{\nu_{Rr} - \nu_C + \nu_0 i\Gamma}\right) \tag{2.21}$$

The formula describes a transition from an initial vibrational state n to a final vibrational state m coupled with vibronic states Rr.

2.3.4.1 Resonance Raman

When the frequency of incident light is close (preresonance) or equal (resonance) to the frequency of the electronic transition to Rr (ν_{Rr}), the first term in the scattering tensor of equation 2.22, dominates over the rest of the terms. In this way, the vibrational transitions that couple with the electronic transition dominate the Raman spectrum which is commonly known as resonance Raman effect.

Using Born-Oppenheimer approximation, where wavefunctions of nuclei and electron motion are separated, the polarizability tensor can be rewritten to (2.22).

$$\alpha_{nm} = \frac{1}{h}\sum_{r}\left(\frac{\langle nG|M_\rho|Rr\rangle\langle rR|M_\sigma|Gm\rangle}{\nu_{Rr} - \nu_C - \nu_0 + i\Gamma}\right) = \frac{1}{h}\sum_{r}\left(\frac{\langle nr\rangle\langle rm\rangle M_\rho M_\sigma}{\nu_{Rr} - \nu_C - \nu_0 + i\Gamma}\right) \tag{2.22}$$

In this expression, $M_{\rho\sigma}$ refers to the transition dipole moment components of the ground to the electronically excited state and can be further expanded using Taylor series with respect to the normal coordinate Q_k. According to the harmonic approximation, higher terms of this transformation can be neglected. Thus, we obtain 1st and 2nd terms which refer to Albrecht's A- (2.23) and B- (2.24) terms of resonance enhancement (2.25).[51]

$$[\alpha_{nm}]_{\rho\sigma} = A_{\rho\sigma} + B_{\rho\sigma} \tag{2.23}$$

$$A_{\rho\sigma} = \frac{1}{h}\sum_r \left(\frac{\langle nr\rangle\langle rm\rangle M^0_{GR,\rho}\ M^0_{GR,\sigma}}{\nu_{Rr} - \nu_C - \nu_0 + i\Gamma}\right) \tag{2.24}$$

$$B_{\rho\sigma} = \frac{1}{h}\sum_r \left(\frac{\langle n|Q_k|r\rangle\langle rm\rangle \left(\frac{\partial M_{GR,\sigma}}{\partial Q_k}\right)_0 M^0_{GR,\sigma}}{\nu_{Rr} - \nu_C - \nu_0 + i\Gamma} \right) + \left(\frac{\langle nr\rangle\langle r|Q_k|m\rangle \left(\frac{\partial M_{GR,\rho}}{\partial Q_k}\right)_0 M^0_{GR,\rho}}{\nu_{Rr} - \nu_C - \nu_0 + i\Gamma} \right) \tag{2.25}$$

Both of these terms have different scattering mechanisms and whether the molecule will scatter the incident light via A- term or B-term depends on the symmetry of the molecule and the size of the transition dipole moment.

The A-term scales with the square of the transition dipole moment M, therefore it becomes the leading term for transitions with large transition dipole moments. The A-term enhancement is most pronounced for strongly allowed electronic transitions as for example electric dipole allowed σ-σ*, π-π* or charge transfer transitions. Moreover, Franck-Condon factor products $\langle nr\rangle\langle rm\rangle$, which are integrals over the products of vibrational wavefunctions, determine if resonance enhancement will occur. Only for the transitions, where the products are non-zero, Franck-Condon resonance enhancement appears. This takes place for the normal modes which exhibit at least one internal coordinate displacement Δs (Figure 2.6) in the transition from ground to electronic excited state and can be simplified in expression (2.26).[51]

$$A \propto \frac{|M^0_{GR}|^2 * \nu_S * \Delta s}{(\nu_{Rr} - \nu_0 + i\Gamma)(\nu_{Rr} - \nu_C - \nu_0 + i\Gamma)} \tag{2.26}$$

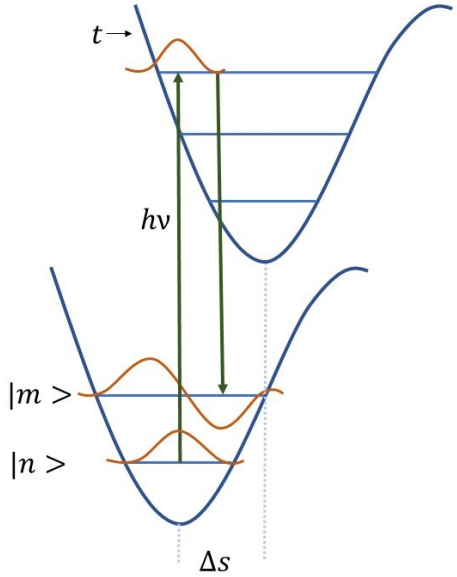

Figure 2.6 Potential energy curves of ground and electronic excited states with emphasized vibrational energy levels n and m. Orange lines in the ground state represent vibrational wavefunctions. The transition from the ground vibrational state, through intermediate to the final vibrational state, is depicted by green lines.

B-term enhancement mechanism is governed mostly by derivative of transition dipole moment with respect to a normal coordinate (2.25).[51] This becomes important for vibronic coupling of resonant excited state to another excited state, even if the resonant electronic transition is weak.

2.3.5 Surface enhanced Raman and Infrared Spectroscopy

Molecules adsorbed on certain metal surfaces may exhibit a drastic enhancement of Raman and Infrared signals by a factor of 10^7-10^8 and 10-10^3, respectively.[52,53] Such surfaces are called SERS- and SEIRA-active and consist of nanoscopic particles or nanostructured metal surfaces. The theories to explain the enhancement phenomenon can be classified into electromagnetic and chemical interaction theories. Although the mechanism of enhancement is based on similar principles, the magnitude of this effect is much bigger in SERS then in SEIRA.

An electromagnetic model was developed by Moskovic.[54] It describes that for particles with size much smaller than the wavelength of the incident light, the electromagnetic field E_0 can effectively couple to free electrons oscillations in the metal. It creates a wave of electrons in the conductor that is commonly referred to as surface plasmons. In general, surface plasmons can either be propagating on the surface of a grating, for example, or localized on the surface of a spherical particle. Here, nanoscopic surface roughness or size of the particle is required for the excitation of surface plasmons by light. It is described as localized surface plasmon resonance (LPR) effect. Upon interactions with the surface plasmons, the electric field $\overrightarrow{E_0}$ of

the incident electromagnetic radiation induces an addition field component $\overrightarrow{E_{ind}}$ resulting in a total electric field $\overrightarrow{E_{tot}}$ according to (2.27).

$$\overrightarrow{E_{tot}} = \overrightarrow{E_0}(\nu_0) + \overrightarrow{E_{ind}}(\nu_0) \tag{2.27}$$

The additional enhancement of this electric field can be rewritten as equation (2.28), where g_0 represents a frequency-dependent parameter of the metal.

$$F_E(\nu_0) = \frac{|\overrightarrow{E_0}(\nu_0) + \overrightarrow{E_{ind}}(\nu_0)|}{|\overrightarrow{E_0}(\nu_0)|} = |1 + 2g_0| \tag{2.28}$$

In the same way the Raman scattered light of an adsorbed molecule induces an additional field component of the frequency of the Raman transition ($\nu_0 \pm \nu_C$). Thus, plasmonic interactions lead to field enhancement of both the incident and the scattered radiation. Since the Raman intensity scales with the square of the electric field, the enhancement factor F_{SER} is given by (2.29).

$$F_{SER}(\nu_0 \pm \nu_C) = [(1 + 2g_o)(1 + 2g_R)]^2 \tag{2.29}$$

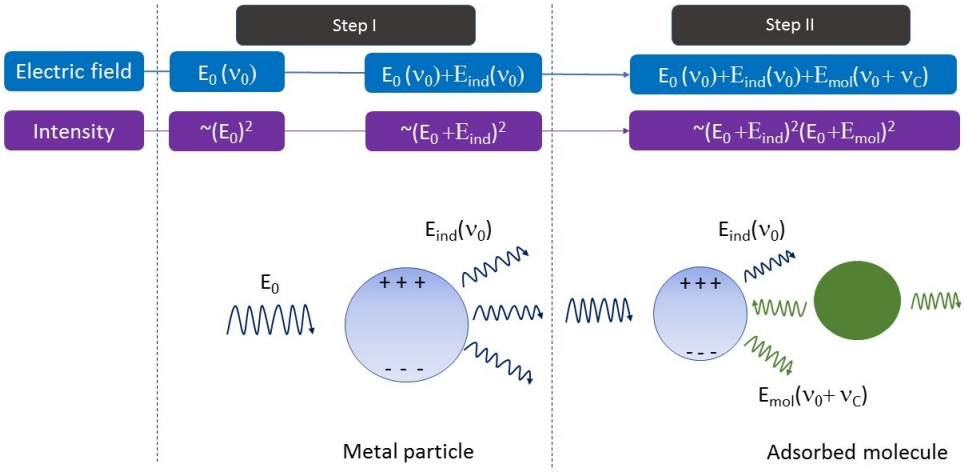

Figure 2.7 Representation of electromagnetic SER effect spherical metal particle on scattered radiation by adsorbed molecule. The mechanism is formally divided in two steps, in which first one represents induced electric field in the particle by incoming light, and the second one shows the combination of induced electric field from the first step with additional induced electric field component by scattered light by molecule.

Large enhancement occurs for surfaces which are rough on the nanoscale (10-100 nm). Roughened surfaces can be obtained by electrochemical treatment, evaporation or sputtering

of metal films in vacuum or by formation of nanoparticle arrays on material support.[55,56] The magnitude of enhancement depends on dimensions and shape of the metal nanoparticles.

The LPR effect in SEIRA spectroscopy differs from SER spectroscopy. The incident infrared light couples to metal islands and hence, leads to excitation of collective electron resonances that increase localized electric field near the metal surface. As follows, adsorbed molecule directly absorbs the incoming light. This is different in comparison to SERs effect where the molecule further scatters the incoming light which can be further amplified by induced localized electric field. Thus, the magnification of surface enhancement in SEIRA is smaller in comparison to SERS and scales with the sixth power of the distance to the centre of metal island according to (2.30), where a represents the radius of colloids.

$$F_{SEIRA}(d) = (\frac{a}{a+d})^6 \tag{2.30}$$

Another important aspect of the electromagnetic theory is the distance-dependence of the enhancement factor. It has been shown that for molecules adsorbed on the surface, the factor decays as dipole-dipole interactions decreases, as shown in equation (2.31) where a denotes the radius of colloids and d distance to the surface.

$$F_{SER}(d) = (\frac{a}{a+d})^{12} \tag{2.31}$$

A second theory describing the mechanism of surface enhancement is based on the chemical effect and is considered to be a separate mechanism which can occur in addition to the electromagnetic mechanism.[55] Molecules that are directly adsorbed on sites of roughened metal surfaces can gain selective and potential-dependent enhancement of Raman intensities. The mechanism of this process is similar to resonance Raman conditions. The electronic states of adsorbed molecule can be shifted or broadened by interaction with the surface or new electronic states of adsorbate metal complexes are generated. Such transitions are analogues to charge transfer transitions of metal complexes, gaining an enhancement via resonance Raman mechanism.

The SER effect lowers drastically the concentration demands for samples. Especially, the combination of resonance Raman and surface enhancement (SERR) can result in an up to 10^{12}-fold increase of Raman intensity compared to classical Raman spectra. This is commonly used in investigations on heme proteins attached to the roughened surfaces, in which changes of the cofactor can be selectively probed leaving protein matrix invisible.

SEIRA spectroscopy is particularly useful for investigating structural changes of immobilized proteins. The protein backbone constitutes from characteristic amide bonds which can be easily detected by IR spectroscopy (Figure 2.8).[57] Especially strong are the amide I bands which includes mainly C=O stretching and N-H bending coordinates and are detectable in a region of 1700-1600 cm^{-1}. The amide II bands include N-H bending and C-N stretching coordinates detectable in a region of 1580-1480 cm^{-1}. The position of the amide I is directly correlated to the secondary structure of the protein.[58] Amide bands are enhanced in SEIRA allowing the detection of secondary structure changes[59–62], for instance, as a consequence of a redox transition.[63,64]

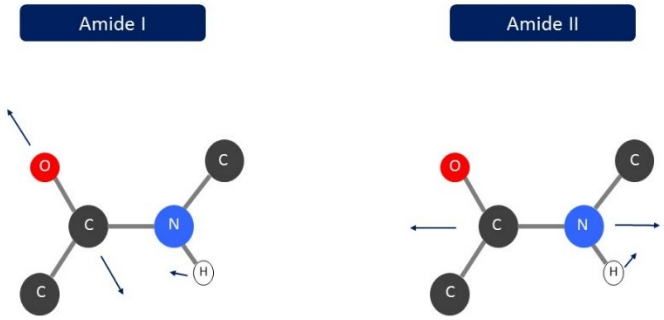

Figure 2.8 Representation of vibrations constituting protein backbone amide I and II bonds.

Another advantageous aspect of surface enhanced vibrational spectroscopy experiments is the possibility of determining the orientation of adsorbed molecule. Induced local electromagnetic field at metal surface is polarized perpendicular to the surface, thus vibrations oscillating perpendicular to the surface are exhibiting higher enhancement then randomly oriented ones.

2.3.6 Resonance Raman of heme proteins

Resonance Raman can be particularly important in exploring structure-function relationships of biological molecules. By choosing a laser line close to the electronic transition of the chromophore, Raman bands originating from the cofactor are enhanced. This method has been extensively used for monitoring the structural changes of the heme cofactor.

For an ideal, planar porphyrin molecule the D_{4h} point group represents most satisfactory symmetry description. In total, an unsubstituted metalloporphyrin has 81 normal modes S,

which in general can be divided into two: in-plane and out-of-plane normal modes according to (2.32).[65]

$$S_{in-plane} = 7A_{1g} + 6A_{2g} + 7B_{1g} + 7B_{2g} + 14E_u \quad (2.32)$$
$$S_{out-of-plane} = 2A_{1u} + 5A_{2u} + 4B_{1u} + 3B_{2u} + 6E_g$$

The resonance Raman spectrum is dominated by in-plane modes, as the dominant electronic transitions are π-π* transitions polarized in the porphyrin plane. Among these in-plane modes, the A_{2g} transitions and E_u transitions are Raman inactive. The most prominent vibrational bands in RR spectrum of a heme are in a 1300-1700 cm^{-1} spectral region and are expected to involve primarily stretching of the various C-C and C-N bonds in the porphyrin ring, as well as bending of the methine C-H groups. The RR spectrum of the heme below 600 cm^{-1}, known as fingerprint region, includes vibrations of peripheral substituents of the porphyrin and metal-ligand vibrations.

A-type scattering mechanism leads to an enhancement of totally symmetric modes (A_{1g}). The non-totally symmetric modes belong to A_{2g}, B_{1g} and B_{2g} irreducible representations. They are enhanced by B-type scattering, in which enhancement occurs based on Herzberg-Teller mechanism of vibronic coupling of electronic and vibrational transitions. As a result, they are most enhanced under Q-band excitation.

In heme containing proteins, the porphyrin plane often does not exhibit ideal planarity. Porphyrin plane deformations can be caused either by peripheral substituents of the porphyrin or perturbations of the changed core size. The latter one could be an effect of the redox reaction of the metal or coordination by axial ligand.[16,66,67] The most common deformations include saddling (B_{2u}), ruffling (B_{1u}), doming (A_{2u}) or waving (E_g). This leads to lowering of the porphyrin symmetry and thus substantially affects enhancement of vibrational bands in the RR spectrum, and modes other than A_{1g}, A_{2g}, B_{2g}, B_{1g} may become RR active.

It has been shown that resonance Raman spectra of hemes can provide particular information about the chromophore local environment, coordination of iron and character of its axial ligands, as well its redox state (Figure 2.9). Complete assignment of vibrational bands appearing in the fingerprint region (or high frequency region) between 1300 and 1700 cm^{-1} has been achieved for many cytochromes allowing correlating specific structural changes of the heme to character of a vibration. It is known that some frequencies exhibit dependency on the core size of the porphyrin.[68] Such normal modes like ν_4, ν_3, ν_2, ν_{10}, ν_{38}, ν_{37}, ν_{11}, ν_{19} are sensitive to expansion of heme pocket size which results in weakening of the force constants and thus in downshifting of the vibrational frequency. Increased core size could be a result of

oxidation or coordination state changes of the iron. For example, iron in the ferric state (Fe^{3+}) occupies smaller space than in the ferrous (Fe^{2+}) state. Also, the type of axial ligation defines the size of the heme pocket. In general, iron can be found either in 5 coordinated or 6 coordinated state, but depending on the character of axial ligand it can form 5c high spin (HS), 6cHS or 6c low spin (LS) state. The heme is typically axially coordinated by amino acids like His, Met, Arg, Cys or Tyr. Additionally, an iron can be ligated as well by small molecules which can be divided into strong and weak ligands. -CO, -CN, -O-O, and =O groups are considered strong ligands, whereas -OH and water are considered weak ligands. Usually an iron possesses one or two strong axial ligands forming 5cHS or 6cLS, respectively or one strong and one weak axial ligand forming 6cHS state. Whether a low or high spin state is formed is determined by the energy gap between d-orbitals of iron. Thus, large energy gaps result in low spin (LS) state whereas small energy gaps result in the high spin (HS) state. In 5cHS heme state, the iron is pulled towards the strong ligand and goes out of the porphyrin plane which decreases the core size and downshifts the core size sensitive porphyrin modes. In 6c state, the iron remains in the plane, however strong ligands decrease the effective core size of iron. Hence, the frequencies of the porphyrin modes increase in the order 5cHS<6cHS<6cLS.

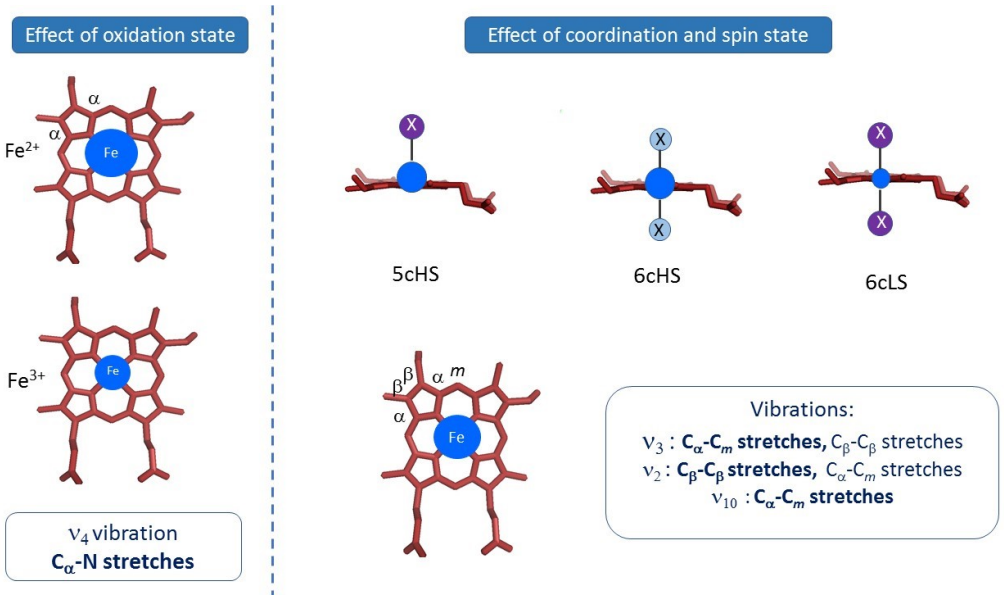

Figure 2.9 Effect of oxidation, coordination and spin state of the iron on the porphyrin core size and its vibrational modes. Sensitivity of the changes is indicated by the size and position of metal ion. X represents an axial ligand.

2.4 Electrochemical techniques

Electrochemical methods probe currents produced as a result of a redox reaction. The event of producing an electrochemical response takes place at the interface of an electronic conductor (electrode) and an ionic conductor (electrolyte) and occurs at a specific potential. The critical factor for the process is a transfer of charge (electrons) between two phases. Charge carriers in the electrode refer to electrons or holes, whereas in the electrolyte to ions. The information about electron transfer direction, its magnitude and potential at which occur is obtained in cyclic voltammetry experiment.[69]

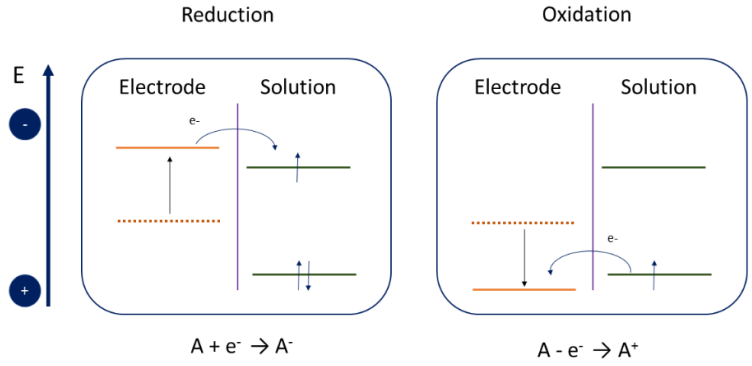

Figure 2.10 Representation of energy levels of molecular orbitals of an electrode and solute and electron transfer between them during reduction and oxidation processes.

A redox reaction in an electrochemical cell consists of two half-reactions: oxidation and reduction. The half reaction of interest occurs at the working electrode, whereas the other half reaction takes place at the counter electrode. To control the potential at the working electrode, the reference electrode of constant composition and a fixed potential is used. All together, the electrochemical cell consists of three electrodes and is known as three-electrode system (Figure 2.11). To induce charge transfer from working electrode to an interfacial solution, the negative potential is applied. It raises the energy of electrons in the electrode to such a level that they can transfer into vacant electronic states of a species present in the solution. When it happens, the flow of electrons, which is a reduction current is observed (Figure 2.10). Similar current flow but with opposite sign occurs, when the energy of electrons is lowered to move some of electrons from a molecular species into the electrode and is called oxidative current. The

potential where oxidation or reduction happen is referred to as standard potential E^0, and is a characteristic parameter for the molecule.

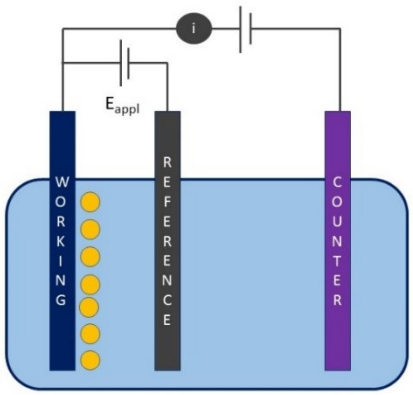

Figure 2.11 The three electrode electrochemical cell consisting of working, reference and counter electrode.

2.4.1 Thermodynamics and kinetics of an electrochemical reaction

Two half-reactions of a chemical reaction are usually denoted as a redox couple, for which we can determine redox potential. This potential refers to the situation where the concentration of oxidized and reduced species is equal. The electrode potential is directly correlated to the concentration of oxidized/reduced species according to the Nernst equation. For instance, for the reaction (2.33), it has a form (2.34), where R is the gas constant, F the Faraday constan and n the number of transferred electrons.[70]

$$O + ne \leftrightarrow R \tag{2.33}$$

$$E = E^0 + \frac{RT}{nF} ln \frac{[O]}{[R]} \tag{2.34}$$

Here, the potential is correlated to free Gibbs energy changes ΔG according to (2.35)

$$\Delta G = -nFE \tag{2.35}$$

The rate of an electrochemical reaction varies with the temperature and can with first approximation be expressed using Arrhenius equation (2.36), where $\Delta G^{\ddagger}$ represents activation energy.

$$k = Ae^{-\frac{\Delta G^{\ddagger}}{RT}} \tag{2.36}$$

2.4.2 Electric double-layer

The behavior of the electrode-solution interface can be compared to a capacitor. When a potential is applied to the electrode, charging current occures and charges accumulate on the metal side. The array of charged species at a metal/solution interface is called electric-double layer and consists of several layers (Figure 2.13). The charges of a closest layer (inner layer, inner Helmholtz plane) depends on the potential of the metal with respect to the solution and it might consist of ions and specifically adsorbed molecules. The next layer contains solvated ions which exhibit weak electrostatic interactions with the charged metal and is referred to as outer Helmholtz player. The third, last layer is called diffuse layer which extends to the bulk solution and contains ions with no electrostatic interactions with the electrode. The thickness of layers changes as the result of ionic strength conditions in a system. The structure of the double layer causes the potential to drop between the electrode and solution. This potential change might influence the rate of electrode processes.[69]

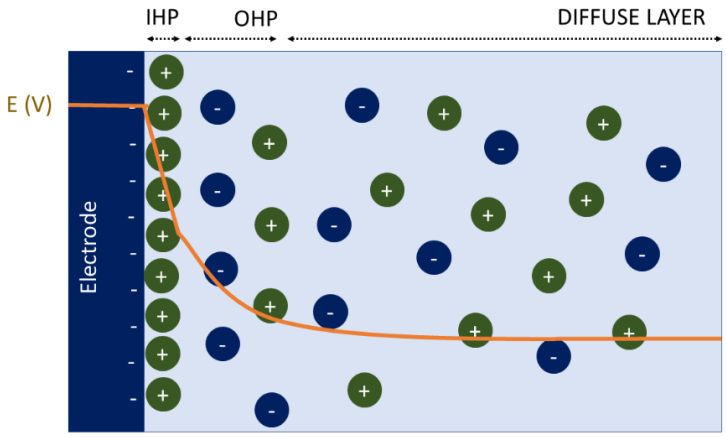

Figure 2.13 Electric double layer at metal solution interface. IHP refers to the inner Helmholtz plane, OHP to outer Helmholtz plane. Positive charges represent cations and negative anions. The orange line represents the potential drop across the layers.

2.4.3 Electron transfer in proteins

It is known that in proteins electrons can travel over large distances up to 40 Å. The charge transport between two redox sites occurs as a result of electron tunneling or electron hopping. The maximum distance for single step tunneling is believed to be not higher than 20 Å, whereas

electron hopping which is a coupled tunneling can exceed this distance limit. In general, both mechanisms can be explained on the basis of nonadiabatic electron transfers. In this reaction, donor and acceptor sites are in not in van der Waals contact to each other, and electrons can tunnel from one energy surface to another at their intersection point, whereas nuclei remains fixed (Figure 2.14). The transition state for this process lies in nuclear configuration area where configuration of reactants and products are similar, and it can be reached just by fluctuations of redox sites and their surroundings, allowing for an electron to transfer. The interactions between the sites is often very weak. Thus, the transition state must be formed many times before finally ET can occur. The probability of this electron jump is given by Landau-Zener equation (2.37), where $\Delta\varepsilon$ refers to tunneling energy gap between two potential energy surfaces, S_1 and S_2 are slopes of the non-interacting energy surface and ν is the nuclear velocity.[71]

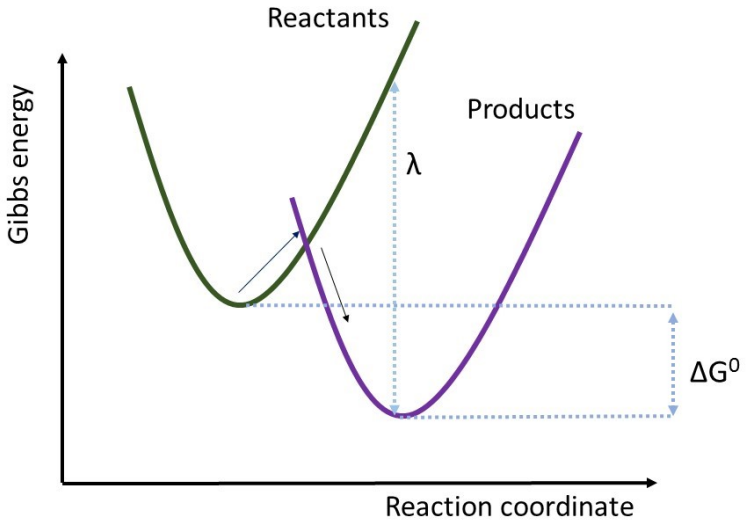

Figure 2.14 Schematic representation of potential energy surfaces of reactants and products. Arrows are indicating the path of the reaction passing through the intermediate state of a higher energy. The activation barrier ΔG^0 and the reorganization energy λ are depicted.

$$P = \frac{e^{-2\pi(\frac{\Delta\varepsilon}{2})^2}}{h\nu(S_1 - S_2)} \tag{2.37}$$

The reaction is termed adiabatic if the probability P of electron transfer at transition state to occur is equal to 1. If $P \ll 1$, the electron transfer reaction proceeds in the non-adiabatic regime.

Equation (2.37) leads to a semiclassical expression for the rate of a nonadiabatic electron transfer between donor and acceptor (2.38).[72]

$$k_{ET} = \frac{4\pi^3}{h^2 \lambda k_B T} H_{AB}^2 \exp[\frac{-(\Delta G^0 + \lambda)^2}{4\lambda k_B T}] \quad (2.38)$$

The rate of the transfer depends on the nuclear reorganization energy λ, reaction driving force ΔG^0, and electronic coupling strength between reactant and product H_{AB}. First, the electron transfer rate increases with increasing driving force, then it reaches its maximum when the nuclear factor is optimized ($-\Delta G^0 = \lambda$) and it further decreases for $-\Delta G^0 > \lambda$ (so called inverted region).

Starting from the first parameter λ, the reorganization energy is defined as the energy of the donor at the equilibrium nuclear configuration of the acceptor.[7374] For electron transfer reactions, polar solvents surrounding redox sites contribute to reorganization energy. Reorientation of solvent molecule arises as a response of the change in the charged distribution of reactants. This effect plays a great role in proteins where often redox active sites are buried deeply inside the protein. A hydrophilic environment however, leads to a larger reorganization energy than a hydrophobic site. The second contribution to this parameter arises from changes in bond lengths and angles of the donor and acceptor following ET. Thus, the reorientation of the secondary structure of protein may also contribute to the reorganization energy. However, dynamics of nuclear motion are expected to be much slower than those of solvent molecules.[74]

The second parameter H_{AB} reflects the strength of the interaction between reactants and products at the nuclear configuration of the transition state. It can be expressed using superexchange-coupling models, where electronic states of the intervening bridge mediate the couplings between donor and acceptor via superexchange. The total coupling depends upon the interaction of adjacent elements and has a form of expression (2.39), where h_{Ab} and h_{bB} represent the coupling strength between the redox sites and the bridge, h_{bb} represents coupling between adjacent elements of the bridge and Δε is the tunneling energy gap.

$$H_{AB} = \frac{h_{Ab}}{\Delta\varepsilon} (\frac{h_{bb}}{\Delta\varepsilon})^{n-1} h_{bB} \quad (2.39)$$

If the separation between donor and acceptor is a linear function of n covalent bonds, H_{AB}^2 decays exponentially with increasing n elements. The height of the effective tunneling barrier can be than expressed as (2.40), where β represents exponential decay constant.

$$\Delta E_{eff} = \left(\frac{\hbar^2}{8m_e}\right)[(\frac{2}{\delta})\ln(\frac{\Delta\varepsilon}{h_{bb}})]^2 = (\frac{\hbar^2}{8m_e})\beta^2 \quad (2.40)$$

It was shown, that β-sheets in proteins are more effective in coupling long-range interactions than α helical structures.[75]

The redox chemistry of proteins and the kinetics of electron transfer rates are often studied by adsorbing molecules on an electrode surface. This heterogeneous electron transfer is considered to act via electron tunneling and is most often treated by Marcus theory.[76] In simplified manner probability of electron tunneling can be expressed by form (2.41), where x is the distance between the electrode and the redox site of protein, and β is a factor that depends on the height of the energy barrier and the nature of the medium between two states.[69]

$$P \propto e^{-\beta x} \tag{2.41}$$

For strong electronic coupling H_{AB} between two reactants, the reaction is considered to be adiabatic. The splitting at the intersection of two energy curves is larger than kT and thus, it forces the system to stay on the lower surface (connecting reactants and products) passing from donor to acceptor. For the reactants being far away to each other, the process proceeds via the nonadiabatic mechanism described above. Immobilized proteins on electrodes are often attached to the surface by biocompatible coatings, resulting in longer distance from the electrode to an active site. As follows, electron transfer of these reactions is treated as a nonadiabatic process.[72]

III. METHODS AND INSTRUMENTATION

The detailed description of sample arrangements and instruments, as well as the methods and data analysis used in this work, will be instructed in this chapter. For detailed data about sample synthesis, sample concentrations and used chemicals, more information is given in the following chapter.

3.1 Measurements in solution

Resonance Raman and UV-Vis absorption measurements were done using a thin quartz cuvette. Most of the measurements required anaerobic environment, thus the cuvette was tightly sealed with a septum sleeve rubber, and purged with Argon, prior to inserting the sample solution.

3.1.1 Resonance Raman

All Raman measurements were done using a confocal Raman spectrometer (LabRam HR-800, Jovin Yvon) equipped with a nitrogen-cooled CCD Symphony detector. The 413 nm laser line of the Krypton ion continuous wave laser was used as excitation source. The laser beam was focused on the sample using a 20x Olympus objective and the scattered light was collected in an 180° back-scattering geometry. The laser power was adjusted for each experiment individually. Spectra were collected with 1-2 cm^{-1} spectral resolution. Raman spectra were calibrated to the Raman shift of Hg positioned at 435.834 nm. The sample component was rotated, by placing it on a rotating table, to avoid photoinduced processes like photodegradation or photoreduction. All measurements were done at room temperature (23° C).

RR and SERR spectra were analyzed using the homemade qpipsi software. The spectra were baseline-corrected by fitting a polynomial line to the raw data which was subsequently substracted from the spectrum to remove the background signal. Component spectra analysis was used to detect and assign porphyrin vibrational modes, which was done by fitting Lorentzian curves to the peaks.

3.1.2 Spectro-electrochemical UV-vis

All UV-vis measurements were done using an Agilent spectrophotometer (Cary 60 UV-vis or Cary 4000 Uv-vis) equipped with a Xenon flash lamp source and a standard 10 mm pathlength cuvette holder compartment. Collected spectra were automatically baseline corrected by subtracting a previously measured signal from the buffer.

Spectro-electrochemical measurements required a specific three-electrode electrochemical cell designed for UV-vis spectroscopy, which was purchased from PINE. The cell consists of a thin-layer quartz cuvette, a 'honeycomb' electrode and the cap holding the chip and the reference electrode in proper positions (Fig. 3.1A). The 'honeycomb' chip contains a gold working and gold counter electrode that have been screen-printed on to a rugged ceramic substrate. The working electrode is perforated with a honeycomb pattern of holes which allow light to pass through the electrode (Fig. 3.1B). The active surface of the working electrode includes a metal coating along the inner walls of the holes[77]. Prior to the experiment, the holes were coated by a mixture of a self-assembled monolayer (SAM) forming a neutral charge to avoid direct adsorption of measured protein to the metal surface. It was achieved by placing the chip into 1mM 3-mercapto-1-propionic acid and 1mM 3-amino-1-propanethiol, dissolved in ethanol. The effective path length of passing light is the length of the honeycomb card (1.7 mm).[78] For the light to pass precisely through the 'honeycomb', the height of the cell was fine-tuned by adjusting the spectrophotometer's cuvette holder compartment.

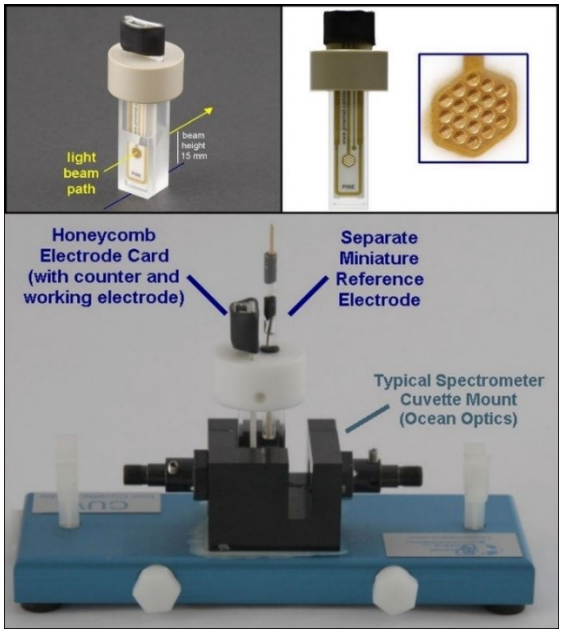

Figure 3.1 (A) Spectro-electrochemical cell for UV-vis detection with (B) 'honeycomb' electrode. (C) The spectrophotometer's cuvette holder with the mounted cell.[77]

This setup was used to detect redox transitions of protein cofactors. This was achieved as a result of electron transfer from the working electrode to the sample. The maxima of Soret band for oxidized and reduced species were detected. The ratio of oxidized/reduced species concentrations was obtained from the absorption spectrum at each potential after the redox pair has reached a Nernstian equilibrium after a certain time. This ratio was further mapped as a function of applied potential to obtain the redox potential. To accelerate the time of electrolysis, a cocktail of mediators serving as electron carriers, was used.
For performing electrochemical measurements, a potentiostat PGSTAT101 from Metrohm, was used.

3.2 Measurements at interfaces

Potential-dependent spectroscopic measurements were performed using silver for protein immobilization in SERRS, and gold for SEIRA. In both cases the electrodes were functionalized with a biocompatible coating prior to protein immobilization.

3.2.1 SERRS and Electrochemistry

All spectroscopic measurements were done using the same confocal Raman spectrometer with parameters described above. Electrochemical measurements were performed using the potentiostats: CH instrument 660 C for Ag electrode roughening, EG&G, PGSTAT101 (Metrohm) or PGSTAT128N (Metrohm) for all other measurements.

3.2.1.1 Three-electrode cell

Potential-controlled spectroscopic measurements were done using a homebuilt three-electrode cell, in which a rotating ring silver electrode served as a working electrode, a 0.5 mm Pt wire as counter electrode and an Ag|AgCl (3M KCl) as reference electrode (Figure 3.2). To avoid photoinduced processes during laser illumination and mass controlled limitations during an electrochemical experiment, the working electrode was rotated with a rotational speed of range 300 – 900 rpm.

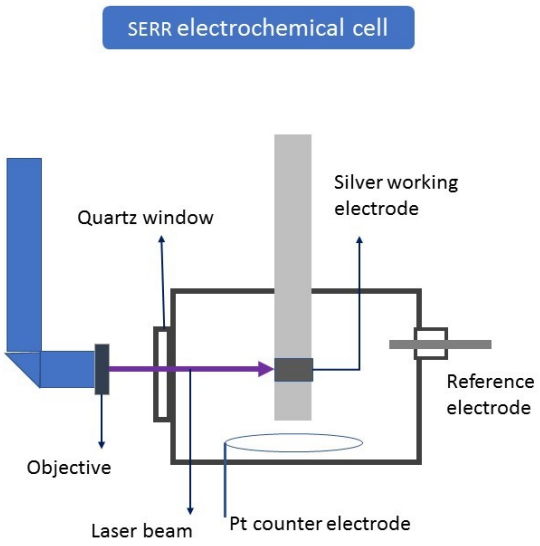

Figure 3.2 The schematic representation of homebuilt three-electrode electrochemical cell used for SERR measurements. The sample is immobilized on the roughened silver electrode which serves as working electrode in an electrochemical experiment.

To obtain SER-active silver surfaces, the electrodes were first polished with polishing paper of two different grain sizes, 100 µm and 0.3 µm, respectively. Subsequently, the surfaces were cleaned with water and ethanol. Secondly, the electrodes were mounted into a three-electrode cell used for roughening and filled with 0.1 M KCl buffer. The potential of -2 V was applied for 40 s. Subsequently, the electrodes were roughened by applying oxidative-reductive steps according to a well-established procedure.[79,80]

For protein immobilization, the so prepared electrodes were further coated with biocompatible monolayers, which were either self-assembled monolayers (SAMs) or polydiallyldimethylammoniumchloride PDADMAC polymers. SAMs provide a very good tool to bind proteins to the electrode via the terminal function of the aliphatic chains.[81] In most cases, the protein attachment was afforded by electrostatic binding between oppositely charged groups on the SAM and the protein surface.

3.2.1.2 Electrochemical procedures

For studying the redox transition of the adsorbed heme cofactor or porphyrin, cyclic voltammetry under non-turnover conditions (in absence of substrate) was used. In this method, the potential is swept with a certain scan rate v (which is change of potential as function of time $v = \frac{dE}{dt}$) to a final potential and then reversed.[82,83] During this cycle, the flowing current

is recorded which includes the Faradaic current as a result of the redox transition on the electrode and the capacitive current arising as a response of the charge density changes on the metal/solution interface. The current i is directly proportional to the concentration of oxidized/reduced species on the electrode, under conditions where no catalytic reaction takes place. The exact function of I is given in equation 3.1, where n refers to a number of electrons, F is the Faraday constant, A the electrode area, D the diffusion coefficient and x the distance between the redox couple and the electrode.[82]

$$i = nFAD(\frac{\partial C}{\partial x})_{x=0} \tag{3.1}$$

When the sweeping potential passes through the potential of the redox transition, cathodic and anodic peaks in the voltammogram are observed (Fig. 3.3A). Detecting these peaks with different scan rates plays an informative role in determining the formal potential of the redox reaction, the number of transferred electrons per transition and the electron transfer rate. For a one-electron transition, the formal redox potential E^f can be determined by the arithmetic mean between the potential of the two peaks (3.2).

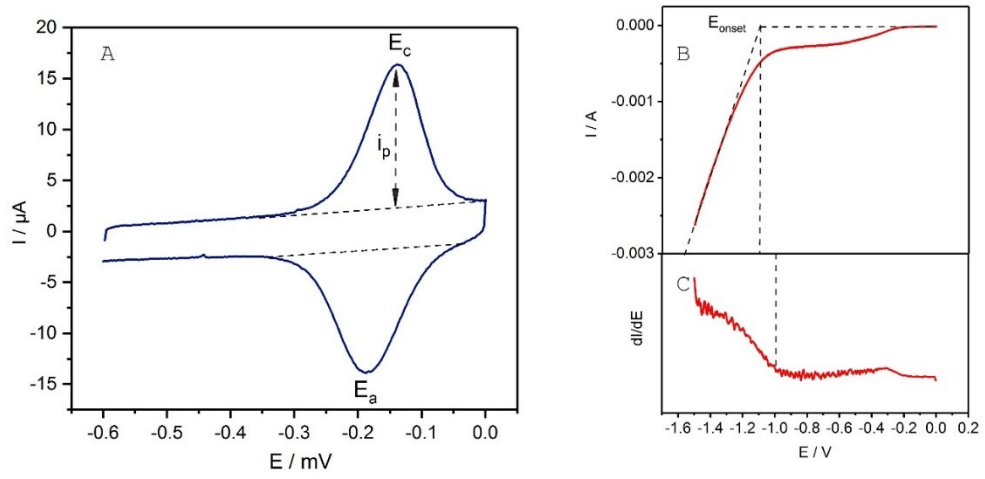

Figure 3.3 Cyclic voltammogram of HTHP protein immobilized on MUA (SAM) coated Ag electrode, in non-turnover conditions (A), recorded with 150 mV/s scan rate. Cyclic voltammogram of CoPCOOMe physisorbed on Ag electrode in turnover conditions (B), recorded with 5 mV/s scan rate, and its current first derivative in respect to potential (C).

$$E^f = \frac{E_C + E_a}{2} \tag{3.2}$$

For ideal Nernstian behavior of adsorbed species, the number of transferred electrons per reaction can be determined by relation (3.3), with $\Delta E = E_c - E_a$.[69]

$$\Delta E = \frac{90.6}{n} \tag{3.3}$$

For a reversible system, the peak current i_p is described by the Randles-Sevcik equation, which can be rewritten as (3.4), where Γ is the surface coverage and f=F/RT. [84,85]

$$i_p = \frac{F^2 v A \Gamma}{RT} \frac{e^{f(E-E^f)}}{(1+e^{f(E-E^f)})^2} \tag{3.4}$$

By analyzing peak positions as a function of scan rate, the electron transfer rate for redox couple can be determined using Laviron method.[85] This method is based on empirical Butler-Volmer equations describing an exponential dependence of the ET scan rate to the driving force (3.5 and 3.6), where k_0 is the rate at zero driving force and α refers to a transfer coefficient (often taken into calculations as ½, but precisely defined as $\alpha = \pm(\frac{RT}{F})(\frac{dln(i)}{dE})$[86]).

$$k_{ox} = k_0 e^{(1-\alpha)f(E-E^f_{O/R})} \tag{3.5}$$

$$k_{red} = k_0 e^{(-\alpha f(E-E^f_{O/R}))} \tag{3.6}$$

The potential peaks can be further directly correlated to the ET rate according to (3.7).

$$E_p = E^f_{O/R} \pm \frac{1}{f} ln \frac{fv}{2k_0} \tag{3.7}$$

Under conditions, in which substrate is present it can donate or accept electrons to or from the redox couple, which directly contributes to the current recorded at the working electrode. As a result, a catalytic current in S-shape voltammogram is recorded (Fig. 3.3). By varying the concentration of substrate, the rate of redox activity can be obtained by Michaelis-Menten kinetics. If the scan rate is sufficiently low, no redox peaks are observed in the voltammogram and the maximum current is dependent on species kinetics and substrate mass transfer. To describe the onset potential for catalysis different methods were applied: The first one requires extrapolating the catalytic response of a catalyst (Fig.3.3B), whereas the second is based on the first derivative of current in respect to potential (Fig. 3.3C).[87] As seen in Fig 3.3, , the values of onset potential can differ depending on the procedure used.

Chronoamperometic measurements were applied to specify the nature of the catalytic response. In this procedure, the response current is recorded after applying a certain potential.

3.2.1.3 Time-resolved SERR

The kinetics of the heme redox transition were followed by using time resolved SERR experiments.[45,80,88] In this method, a rapid potential jump is applied to the system as a pulse, and restoration of an equilibrium is probed by SERR measurements. Such an experiment requires generation of pulsed laser light, which can be afforded using Pockels cells, and proper synchronization of potential jumps with the probing laser pulses, afforded by a pulse-delay generator. The experiment is designed as depicted on fig. 3.3. The potential jumps are chosen in such a way that the potential for measurements is equal to the midpoint potential of the redox species. The delay time δ after which the spectrum is measured is a variable of the experiment. The measurement is repeated n times to provide a satisfactory signal/noise ratio. Therefore, after one cycle, the potential jumps back to its initial value and after the recovery time t_R, the measurement is repeated. This method allows probing ET rates in the range of microseconds.

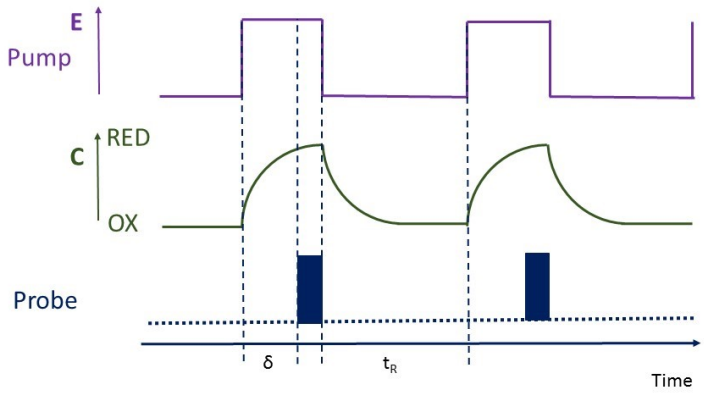

Figure. 3.3 The design of time-resolved potential-dependent SERR experiment, with a change of potential serving as the pump. The delay time between potential jump and a probe is depicted as δ and t_R refers to recovery time.

3.2.1.4 Anaerobic box

Working with heme proteins, which in their ferrous state can be very sensitive for reducing oxygen, requires an oxygen free environment. This has been achieved by use of an anaerobic glovebox. This box has been designed for performing Raman measurements by inserting the objective of the Raman microscope into the glovebox via a flexible circular hole (Fig. 3.4) A long brass tube was hereby used that was divided into two pieces such that proper attachment

with satisfactory laser beam alignment could be done. Using this setup a loss of *ca*. 20% intensity of initial Raman signal had to be taken into account.

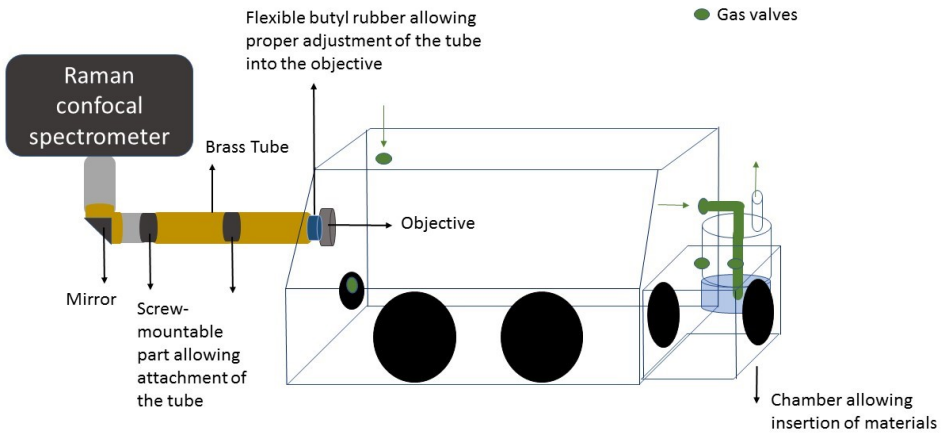

Figure 3.4 The design of anaerobic glovebox suitable to perform Raman measurements.

3.2.2 SEIRA

To obtain a SEIRA-active gold surface, nanostructured gold was deposited on a flat, polished surface of silica by electroless deposition using the mixture of Au plating solution composed of 2% HF, $NaAuCl_4 \cdot 2H_2O$, Na_2SO_3, $Na_2S_2O_3 \cdot 5H_2O$ and NH_4Cl, at 65°C.[59,89] Subsequently, the metal surface was electrochemically cleaned by electrochemical oxidative and reductive cycles, applying a potential between 0.1 V and 1.4 V in the absence of oxygen to avoid generation of reactive oxygen species. The so prepared Au-covered silica electrode served as working electrode and ATR prism in potential dependent SEIRA experiments. The prism was inserted into the spectro-electrochemical homebuilt three electrode SEIRA cell together with a Pt wire, which served as a counter electrode, and a Ag|AgCl (3 M KCl) reference electrode (Figure 3.5).[59] SEIRA measurements were performed using a Bruker IFS66v/s FTIR spectrometer equipped with an ATR setup in the Kretschmann configuration, a liquid N_2 cooled MCT detector and a globar as an IR radiation source. Spectra were recorded with a resolution of 4 cm^{-1}. Further data analysis was obtained using OPUS software.

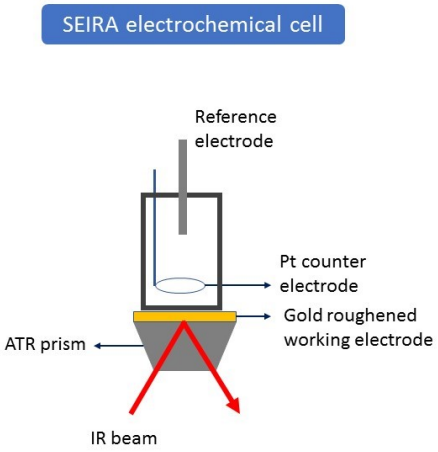

Figure 3.5 The schematic representation of homebuilt three-electrode electrochemical cell used for SEIRA measurements. The sample is immobilized on the roughened gold electrode which serves as working electrode in an electrochemical experiment.

IV. RESULTS AND DISCUSSION

4.1 Switchable Redox Chemistry of the Hexameric Tyrosine-Coordinated Heme Protein[90]

4.1.1 Abstract

Hexameric tyrosine-coordinated heme protein HTHP from Silicibacter pomeroyi has been shown to exhibit peroxidase- and catalase-like activity. In the present study, detailed spectroscopic and electrochemical investigations were performed to analyse the redox properties and active site structure of HTHP. Potentiometric titration of HTHP in solution revealed a single redox transition at –0.54 V (vs. Ag/AgCl), indicating six structurally identical tyrosine coordinates hemes. Cyclic voltammetry (CV) of immobilized HTHP afforded a distinctly more positive redox potential (–0.17 V) but failed to detect a transition at –0.54 V. Conversely, surface enhanced RR (SERR) spectroscopy provided evidence for both high- and low-potential transitions and for a partial loss of heme in the reduced state. The high-potential CV-active redox transition is attributed to the hemes of the barrel-shaped HTHP in a wheel-like orientation on the surface. Supported by coarse-grained simulations and SERR spectroscopy, the majority of HTHP is concluded to adopt a reverse-disc orientation, accounting for the low-potential transition. In view of the striking similarity of HTHP to the heme carriers HasA or HmbR regarding redox potential, Fe-Tyr ligation and heme release, we propose heme transport as an alternative or additional function.

4.1.2 Introduction

Heme proteins exert a variety of biological functions such as catalysts, electron shuttles, or substrate transporters.[4] This versatility of iron porphyrins as cofactors in proteins requires appropriate concepts to ensure specificity of the respective function which include the number and type of axial ligands and the cofactor environment including solvent accessibility, flexibility of the protein fold around the heme, and the internal electrostatics.[8–10] The interplay between these structural properties is essential for controlling the main functional parameters of hemes which are the redox potential and the accessibility of the heme center for specific substrates or molecules. The tuning range for these functional parameters is quite remarkable. The redox potential of hemes bound in proteins can be thus adjusted between ca. +0.2 and −0.6 V (vs. Ag/AgCl) to enable specific functions.[11]

For the hexameric tyrosine-coordinated heme protein (HTHP) studied in this work the physiological function is not known. The extracellular protein is encoded in the genome of the marine bacterium *Silicibacter pomeroyi*, a lithoheterotrophic organism relying on presence of inorganic compounds like carbon monoxide or sulfide to supply heterotrophy.[91,92] The protein displays an intriguing structure with each of the six subunits harboring a solvent-exposed, tyrosine-coordinated b-type heme[93] (Figure 4.1.1A). The six monomers form a barrel-shaped structure with an open hydrophobic channel. The hemes are symmetrically arranged in a ring-like orientation (Figure 4.1.1B). The heme pocket accommodates three arginines, one close to the tyrosine that serves as the only axial ligand of the heme, and two on the distal side (Figure 4.1.1C).[93] These structural properties are reminiscent to those of peroxidases carrying an arginine on the distal side of the heme pocket[94] and to catalases that are ligated by a tyrosine[95]. Thus, and in view of previous studies, it was proposed that HTHP acts as a peroxidase or catalase.[96,93] Despite the enzymatic activity that has been demonstrated for HTHP, one might also take into account a different functionality since HTHP also shows similarities to other tyrosine-coordinated heme proteins like HasA, HmbR, HmuT or ShuA that act as heme transporters.[97–100] Therefore, understanding the HTHP heme structure, the character of the Tyr ligation and finally the correlation of the heme structure with its redox properties is undoubtedly crucial for elucidating the function of HTHP.

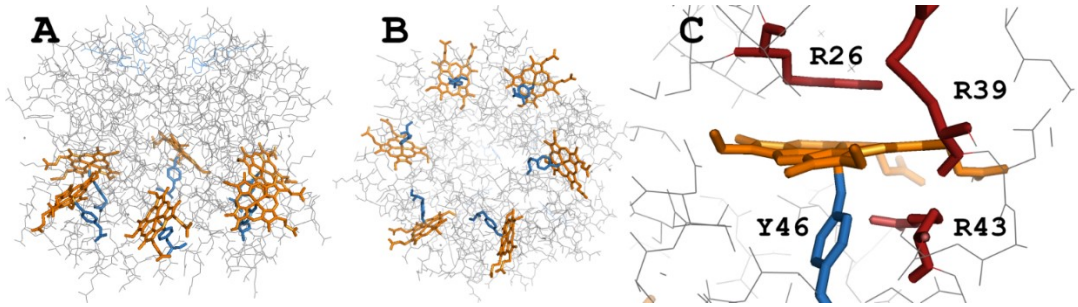

Figure 4.1.1 Structure of the hexameric HTHP [ref., pdb id 2OYY], seen from (A) the side and (B) from the top. The heme groups are highlighted by colours. (C) Structure of the heme pocket highlighting the heme, its axial Tyr ligand, and the Arg residues on the distal and proximal side.

Motivated by this comparison, the structural and redox properties of HTHP have been investigated for the first time. Complementing previous approaches,[96,101,93] the protein was studied in the immobilised state and in solution by combining electrochemical and resonance Raman (RR) spectroscopic techniques to directly relate redox properties with structural parameters of the heme ligation. The experimental approaches were supported by coarse grained simulations which helped to identify possible orientations of the immobilized protein on the surface and correlate them with heme's redox behaviour.

4.1.3 Experimental Section

Materials

Cysteamine, 3-mercaptopropionic acid, 11-mercaptoundecaoic acid, N-hydroxysuccinimide (NHS) and N-(3-Dimethylaminopropyl)-N'-ethylcarbodiimide hydrochloride (EDC), sodium dithionite were purchased from Sigma Aldrich. HTHP was heterologously expressed in *Escherichia coli* and purified as an untagged protein.[93] Further addition of iron protoporphyrin IX chloride *in vitro* increased the yield of heme-containing HTHP. The concentration values of HTHP throughout this report refer to molar values of monomer with one heme.The water used in all experiments was purified by a Milipore system. All measurements of the protein in solution and immobilised on an electrode were carried out at pH 8.0 in 20 mM and 2.5 mM TRIS buffer, respectively.

UV-vis spectro-electrochemcial redox titration

Spectro-electrochemical measurements were performed in an anaerobic tent using a PINE Honeycomb spectroelectrochemical cell which was inserted into a UV-vis spectrometer (Agilent), and connected to a potentiostat (Autolab PGSTAT101 from Metrohm). The PINE spectroelectrochemical cell consists of a quartz cuvette with a honeycomb panel working Au electrode and a Pt wire as counter electrode. An Ag|AgCl electrode (3 M KCl) was used as reference, to which all potentials cited in this work refer to, if not specified otherwise. In the experiments, a solution of *ca*. 100 µM buffered solution of HTHP was used, including a cocktail of mediators covering a wide range of redox potentials (indicated in parentheses): 1,4 naphtoquinone (60 mV), phenazinemethosulfate (40 mV), 5-hydroxy-1,4-naphtoquinone (190 mV), anthraquinone-2-sulfonate (–35 mV), phenosafranine (–62 mV), safranine T (–99 mV) , deiquat (160 mV), methyl viologen (258 mV), 4,4'-dimethyl-2,2'-dipyridyl (–496 mV) and triquat (–350 mV). Spectra were recorded after 30 min of equilibration time following each potential step. Prior to the experiments, the Au electrode was protected against protein adsorption by coating with a mixture of cysteamine and 3-mercaptopropionic acid via incubation in a solution containing 1 mM of each mercapto compound.

Resonance Raman and Surface Enhanced Resonance Raman spectroscopy

For RR measurements, 700 µM of protein solution was prepared in 20 mM TRIS buffer at pH 8. To chemically reduce the protein, 2 mM of NaDT was added to the protein solution, anaerobically. Measurements were done in tightly septum-closed quartz cuvette.

For SERR measurements, Ag cylindrical electrodes were prepared by mechanical polishing of the surface and subsequent electrochemical roughening via consecutive oxidative (300 mV) and reductive (–300 mV) steps[102] Electrodes were then incubated in an ethanolic solution of mercaptoundecanoic acid (1 mM) for *ca.* 16 h and subsequently rinsed with ethanol and water. Enzyme attachment was achieved by placing the coated electrode in 700 µL of *ca.* 3.5 µM of HTHP in 2.5 mM TRIS buffer at pH 8 for 2 h at room temperature. During incubation the electrode was rotating at 360 rpm. For measurements with covalently immobilized protein, the prepared electrode was additionally incubated in a solution of 1 mM EDC and 1 mM NHS for further three hours. Finally, the electrode was placed in a 1M KCl solution for five minutes to remove residual electrostatically bound proteins.

RR and SERR measurements were performed using the 413 nm excitation line of a Krypton ion laser (Coherent Innova 300c). The spectra were recorded at room temperature with a confocal Raman spectrometer (LabRam HR-800, Jobin Yvon). The laser power at the sample was 500 µW. RR spectra were accumulated 10 times for 30 seconds each and averaged. During the experiments, the cell was rotated to avoid photoreduction. SERR spectra were accumulated 6 times for 40 seconds each and averaged. During the measurements, the electrode was rotated through the laser beam to avoid photoreduction. The anaerobic SERR measurements were carried out within a home-built set-up (< 20 ppm O_2) described previously.[103]

Electrochemical measurements

Ag electrodes coated with HTHP as described above were used for cyclic voltammetry (CV) measurements in a range of scan rates from 5 mV/s to 150 mV/s. Measurements were done in the anoxic glove box, using the same experimental conditions as used for SERR experiments.

Coarse-grained molecular dynamics simulations[*]

The crystallographic structure 2OYY of HTHP[93] served as template for generating a coarse-grained (CG) model of the protein. For the conversion of the atomistic structure into a MARTINI CG model[104] the martinize.py script[105] was used assuming a pH of 7.0. Protein and heme cofactors were described with the MARTINI force field for proteins[106] and the parameters derived from tetrapyrroles in photosystem II[107], respectively. In order to compensate the missing hydrogen bonds, essential for protein stability in the CG model, an elastic network called rubber-bands was applied[108]. Moreover, different redox states of the heme cofactors were generated by changing the partial charges of the central beads of the heme. Consequently, the oxidized enzyme was neutrally charged, while the totally reduced variant carried a net charge of 6 e^-.

The surface was generated with home-made scripts assuming an ideal coverage of the gold with alkanethiol chains. All alkanethiol molecules consisted of three beads. The bead adjacent to the gold was fixed to maintain the ideal lattice. The characteristics of the head groups facing the solvent were varied in order to build a symmetric lattice of negative charges. In total, ca. 8 % of all SAM molecules carried a negative charge. While the SAM was treated with the

[*] Done by Dr. T. Utesch (TU Berlin)

MARTINI force field for lipids[104], the gold film was simplified as fixed and well-ordered slab. Gold particles were described as slightly charged beads carrying a positive net charge neutralizing the negative charge of the SAM head groups. This assumption was necessary for a proper conversion of the particle mesh Ewald summation[109] for long-ranged electrostatics. The reduced and oxidized CG protein structures were both placed in different orientations at distances to the SAM of more than 4.0 nm. In this way, reorientations during the adsorption process were possible. To investigate the experimentally observed influence of ionic strength on the immobilization, the systems were simulated under minimal-neutralizing and 100 mM ionic strength conditions mimicked by Na^+Cl^- beads treated with the MARTINI force field for ions.[104] The surrounding water was represented by polarizable water beads[110] to avoid water freezing at the SAM/solution interface. The phenomenon of freezing MARTINI water has been described earlier.[104]

All CG simulations were performed with GROMACS 4.6.7[111] using the MARTINI force field[104] as described above. The 2-µs production runs were preceded by short energy minimizations, heating NVT simulations, and water equilibrations. A time integration step of 20 fs was applied ensuring a stable behavior of the system. The importance of the long-range electrostatics was taken into account by using the Particle-Mesh Ewald summation[109] beyond a cut-off of 1.4 nm. Additionally, a dielectric constant of 2.5 was used which is compatible with the polarizable water model.[110] Van-der Waals interactions were shifted to zero at 1.2 nm. The semi-isotropic system allowing no cell size fluctuations in the surface plane was realized by the Rahman-Parrinello barostat[112] coupling the system to a pressure of 1 atm with a time constant of τ = 12 ps. The temperature of 300 K was simulated by the velocity-rescaling-scale scheme.[113]

4.1.4 Results

Resonance Raman spectroscopic measurements

Upon 413 nm excitation, which is in resonance with the Soret transition, primarily totally symmetric porphyrin modes are enhanced in the RR spectrum. Positions and intensities of these bands in the region between 1300 and 1700 cm^{-1} (marker band region) provide valuable information about oxidation, coordination, and spin state of the iron in the heme and its interactions with the immediate protein environment[45]. In the low frequency region spectrum detailed information about coordinating ligand can be obtained.[114] RR measurements of HTHP

in solution are presented in Figure 4.1.2. In its as-isolated form, HTHP displays the marker bands at frequencies that are characteristic of a ferric penta-coordinated high-spin state (5cHS). This state was completely reduced chemically under anoxic conditions as reflected by the downshift of the mode ν_4 from 1371 to 1359 cm^{-1}, leading to a ferrous 5cHS state. The low frequency region reveals a band characteristic of the iron-phenolate vibration band at 548 cm^{-1} in its as-isolated state, which downshifts to 542 cm^{-1} upon reduction.[98,115] The finding is consistent with the crystal structure that shows Tyr43 as the only axial ligand for each heme. In fact, a careful inspection of the spectra does not reveal any indications for heterogeneities or band splittings implying that in the fully oxidised and reduced state, all hemes adopt the same configuration and structure.[60,100,116–118] The assignment of the individual bands is given in Table 4.1.1. The most striking feature of the ferric state spectrum refers to the relatively low intensity of the ν_4 band, which normally is the strongest band upon Soret band excitation. Here the ν_2 mode is almost equally strong and the intensity of the ν_3 mode at 1489 cm^{-1} even exceeds that of the ν_4 mode. Similarly, also in the ferrous state the relative intensity of the ν_3 mode with respect to other modes is stronger than usually observed in 5cHS ferric hemes.

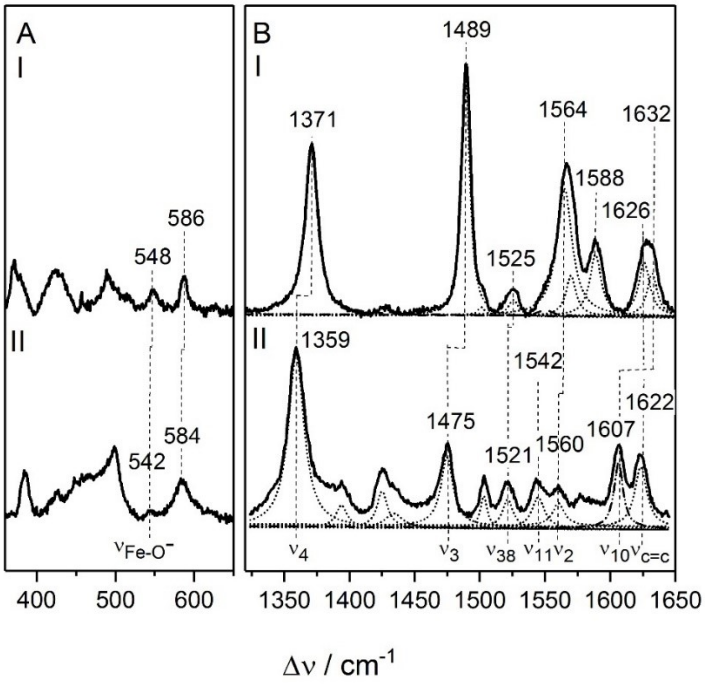

Figure 4.1.2. RR (A) low frequency region and (B) high frequency region spectra of HTHP in 25 mM TRIS buffer of the (I) (as-isolated) oxidized state and the (II) reduced state obtained upon addition of dithionite under anaerobic conditions. The dotted lines represent fitted Lorentzian band shapes.

Table 4.1.1 Spectral assignment of resonance Raman porphyrin vibrations of HTHP in oxidized and reduced state.

Band [cm^{-1}]	Ferric form (Fe^{3+})	Ferrous form (Fe^{2+})
ν_4	1371	1359
ν_3	1489	1475
ν_{38}	1525	1521
ν_2	1564	1560
ν_{19}	1573	
ν_{37}	1588	
$\nu_{c=c}$	1626	1622
ν_{10}	1632	1607
ν_{Fe-O}-	548	542

UV-vis spectro-electrochemical titration

UV-vis spectroscopy was performed to characterize the redox properties of the hemes under anoxic conditions. As-isolated HTHP showed a characteristic Soret band maximum at 400 nm, two peaks in Q-band region at 500 and 530 nm, and a charge transfer band at 620 nm (Figure 6.1.1, Appendix). The ferrous state revealed a shifted Soret band at 434 nm, and a Q band at 555 nm and 590 nm. The results are in line with previously reported data.[93] Electrochemical reduction of the protein was subsequently carried out in a spectro-electrochemical cell placed in an anoxic tent. Here similar spectra were obtained for oxidized and reduced HTHP at an applied voltage of 0.0 V and –0.7 V, respectively (Figure 4.1.3A). However, these spectra include also contributions from the mediators. To sort out these contributions, the absorption spectra were simulated by a set of Lorentzian bands. Among them, the bands at 400 and 434 nm were taken as a measure for the ferric and ferrous form of HTHP, respectively. The maxima and widths of these two bands were then kept constant for the analysis of the spectra of HTHP measured during the stepwise potentiometric reduction in the presence of mediators. The relative intensities of these bands were then converted into relative concentrations using the absorption cross sections of the absorption spectra of the pure oxidized and chemically reduced HTHP. By fitting the Nernstian equation to the potential-dependent relative concentrations a redox potential of –0.54 V (Figure 4.1.3B) is obtained with a number of transferred electrons of nearly one. This finding implies that all six hemes independently transfer electrons at the

same redox potential. Note that this redox potential is more negative by 0.31 V than the one that was obtained previously electrochemically for HTHP attached to electrodes.[96]

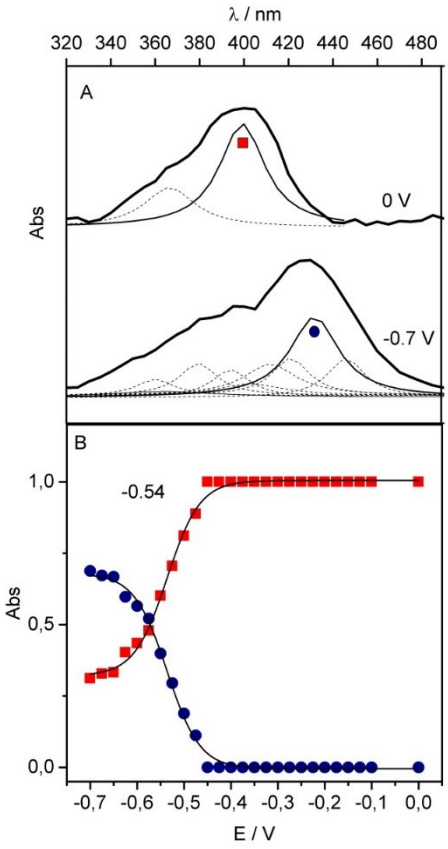

Figure 4.1.3. A: Soret band of absorption spectra of HTHP in solution at pH 8 (20 mM Tris buffer at pH 8.0), measured in the presence of mediators corresponding to a potential of 0 V (top) and –0.7 V (bottom). Dotted lines represent the spectral contributions of the mediators. The violet square and blue circle indicate the main spectral contribution of the oxidized and reduced HTHP, respectively. B: Potential-dependent distribution between the oxidized (red squares) and reduced HTHP (blue circles) under anoxic conditions. The solid black lines represent the fits of the Nernstian equation to the data. The dotted line indicates the redox potential.

Surface-Enhanced Resonance Raman spectroscopic measurements

In the next step the electrochemical properties of immobilized HTHP were investigated. HTHP was attached to a functionalized electrode using two different approaches. First, the electrode was coated with a self-assembled monolayer (SAM) of mercaptoundecanoic acid (MUA). Subsequently, the electrode was incubated in concentrated protein solution to adsorb the protein electrostatically via interactions with the positively charged surface of the protein as described previously[96]. In the second approach, the electrode carrying the electrostatically bound protein was incubated in a solution including EDC and NHS, to covalently crosslink the carboxylic functions of the SAM and surface Lys residues of HTHP.[119]

The SERR spectra of both the electrostatically and the covalently bound HTHP, measured at 0.0 V (Figure 6.1.2, Appendix), agree well with the RR spectrum of the ferric HTHP in solution. Upon lowering the potential, the SERR spectra reflect the reduction of the immobilized HTHP albeit not in the same manner for the covalently and electrostatically bound HTHP as illustrated for the ν_4 band region (Figure 4.1.4A, B). In the latter case, the gradual intensity increase at ca. 1360 cm^{-1} due to the growing-in of the ν_4 mode of the ferrous species might be noted, which, however, does not reach the intensity level of the 1371 cm^{-1} band of the ferric form even at –0.8 V (Fig. 4.1.4B), leaving ca. 40% of the hemes in the ferric state. The relatively weak and poorly resolved intensity distribution feature around 1360 cm^{-1} impairs a reliable band fitting analysis. Thus, to illustrate the potential-dependent reduction of the electrostatically bound HTHP, the integral intensity in this spectral region is demonstrated, after subtracting the contribution of the 1371 cm^{-1} band (Figure 4.1.4D). Plotting these data against the electrode potential indicates that the (incomplete) reduction occurs within two steps at potentials at ca. –0.1 and –0.4 V. For the covalently bound HTHP, reduction is more efficient albeit also not complete, with 25% remaining in the ferric state at –0.8 V. In this case the quality of the spectra allows a component analysis[120] using the SERR spectrum measured at 0.0 V and the RR spectrum of the chemically reduced HTHP as initial component spectra. A detailed description of the component analysis is given in the appendix. However, it turned out that at negative potentials, the ν_4 band envelope broadens, such that the global fit required an additional band component at 1357 cm^{-1}, which is also characteristic of a ferrous 5cHS heme. Thus, it can be concluded that there are two redox couples (states) with ν_4 modes of the ferrous forms at 1359 (I) and 1357 cm^{-1} (II) and the corresponding mode of the ferric form at the same position, i.e. 1371 cm^{-1} (I + II). The redox potentials of these two transitions are estimated to be at ca. –0.49 and –0.43 V for state I and II, respectively (Figure 6.1.3, Appendix).

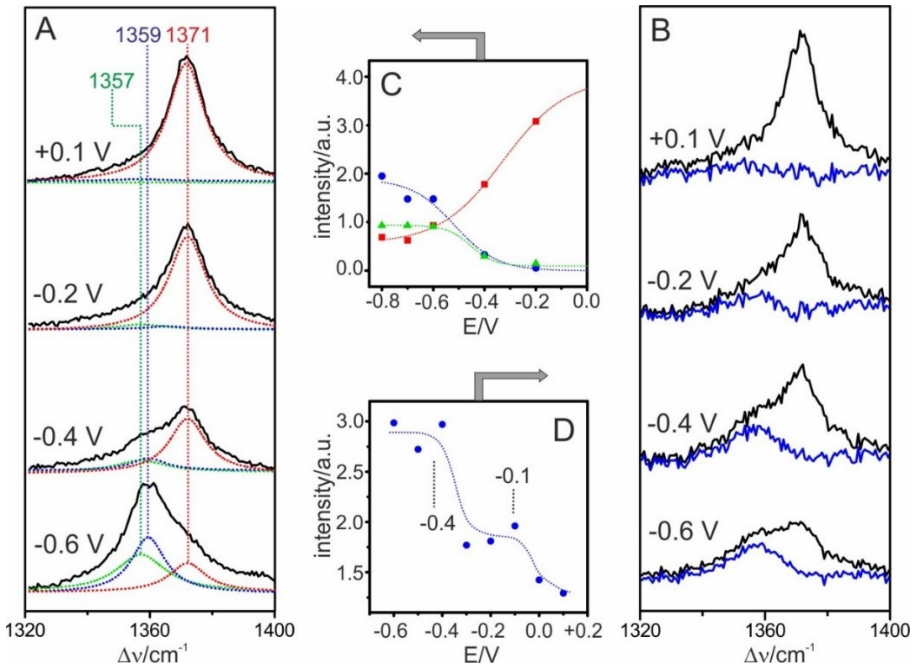

Figure 4.1.4 Potential-dependent SERR spectra in the ν_4 band region of the (A) covalently bound and (B) electrostatically bound HTHP. The spectra were measured with 413 nm excitation under anoxic conditions (pH 8.0, 2.5 mM Tris buffer). The spectra in A were analysed on the basis of the component spectra of the reduced (blue) and oxidized HTHP (red) as derived from the RR spectroscopic measurements. A good global fit requires inclusion of an additional component with a ν_4 band at 1357 cm^{-1} (green). The resultant spectral contributions of the three species are plotted in C vs. the electrode potential. The spectra in C were analysed by first subtracting the ν_4 band component at 1371 cm^{-1} from the experimental spectra and integrating the residual intensity on the low frequency side of this band. In D the intensity values of the component spectra in B were plotted versus the electrode potential. The dotted blue curve, obtained by a polynomial fit, serves to guide the eyes and has no specific physical meaning.

For both the electrostatically and the covalently bound HTHP, an irreversible intensity loss is noted upon shifting the electrode potential to negative values. Re-setting the electrode potential back to 0.0 V indicates a lowering of the SERR intensities by 25% compared to the initial values. As in the case of the covalently bound HTHP, desorption can be excluded. These findings imply either an irreversible destruction of the SAM, or more likely a partial release of heme cofactors from the immobilized HTHP (*vide infra*).

At applied positive potential (0.1 V) the low frequency SERR spectra of covalently attached HTHP also featured the characteristic Fe-Tyr vibration at 548 cm^{-1} (Figure 6.1.4, Appendix). Decrease of potential resulted in loss of intensity of this band with a concomitant loss of intensity of the ν_4 vibration. At an applied negative potential (-0.6 V), a significant fraction of the peak at 548 cm^{-1} is still detectable. Contribution of the 542 cm^{-1} vibration, as seen for reduced HTHP in solution, is not clearly seen in the SERR spectra but cannot be ruled out completely due to the very low overall signal intensity.

Cyclic voltammetry

Cyclic voltammograms (CVs) of the immobilized protein on the Ag electrode reveal just one redox peak of HTHP (Figure 5). When HTHP is immobilized covalently, the capacitive current is noticeable higher. However, the current densities of the transitions (obtained from integrating baseline corrected redox waves) are equal for both immobilization procedures. The redox transitions were found to be –0.17 V and –0.16 V and thus nearly the same for covalently and electrostatically bound HTHP, respectively. These redox potentials are somewhat higher (ca. 70 mV) than those determined by CV for MUA-coated Au electrodes[96] and significantly more positive by at least 0.38 V than the redox potential of HTHP in solution as determined by UV-vis spectroscopy in the present work.

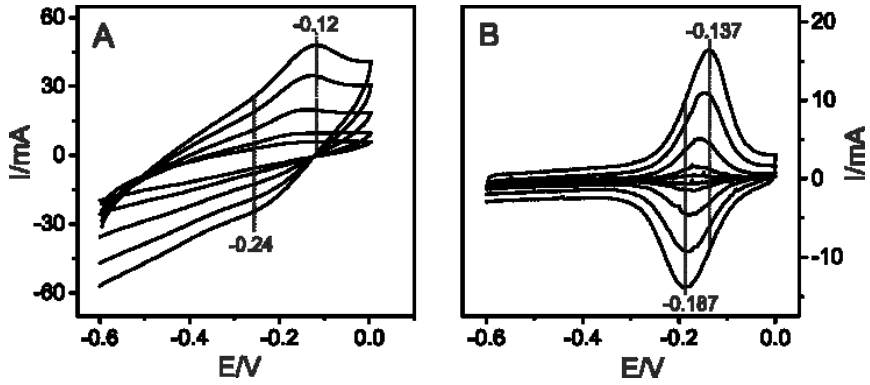

Figure 4.1.5 Cyclic voltammograms in nonturnover conditions of (A) covalently bound HTHP to the electrode, (B) electrostatically bound HTHP to the electrode, in range of different scan rates from 150 mV/s to 10 mV/s. Dotted lines indicate the formal redox potential calculated from the redox peaks. Measurements were carried out in 2.5 mM TRIS buffer at pH 8.

The Laviron method was used to calculate electron transfer rates of the redox transitions in the CVs, assuming that heterogeneous electron transfer is the rate-limiting step, characterized by only one rate constant.[84] For both the covalently and the electrostatically bound HTHP nearly the same rate constants were obtained with k_{ET} values of ca. 9 s^{-1} for the reduction and ca. 2 s^{-1} for the oxidation.

Simulations[†]

CG MD simulations were carried out with HTHP in different oxidation states and at different ionic strengths conditions. Calculations using 100 mM ionic strength (Na^+Cl^-) did not lead to an adsorption for neither oxidized nor reduced HTHP during the 2 µs CG simulation time. Instead, an effective shielding of the negatively charged carboxyl-terminated SAMs by Na^+ beads was observed. These findings are consistent with the experimental observation that HTHP did not bind to carboxyl-terminated SAMs under high ionic strength.

At minimal-neutralizing conditions, where ions are used just to compensate the charge, fully oxidized HTHP established surface contact via its N-terminus and adsorbed initially in the "wheel-like" conformation with all heme cofactors in different distances to the surface (Figure 4.1.6A,B). Subsequently, HTHP changed its orientation on the SAM to adopt the "reverse disc" configuration (Figure 4.1.6C). The reorientation from "wheel-like" to the "reverse disc" was mainly triggered by the C-terminal Lys-75 of the different monomers, which tightly adsorbed on the SAM. Notably, the dipole moment of immobilized HTHP pointed toward the solution, which is in disagreement with recent predictions based on simple electrostatic calculations.[96] This unexpected observation was qualitatively reproduced in independent simulations. Reorientation from the "reverse disc" back to the "wheel-like" conformation was not observed, but might be at least transiently possible since the distances of the individual hemes towards the gold show non-negligible fluctuations indicating a high degree of flexibility of the immobilized protein (Fig. 6.1.5, Appendix). In the fully reduced state, however, the protein does not adsorb to the SAM at all.

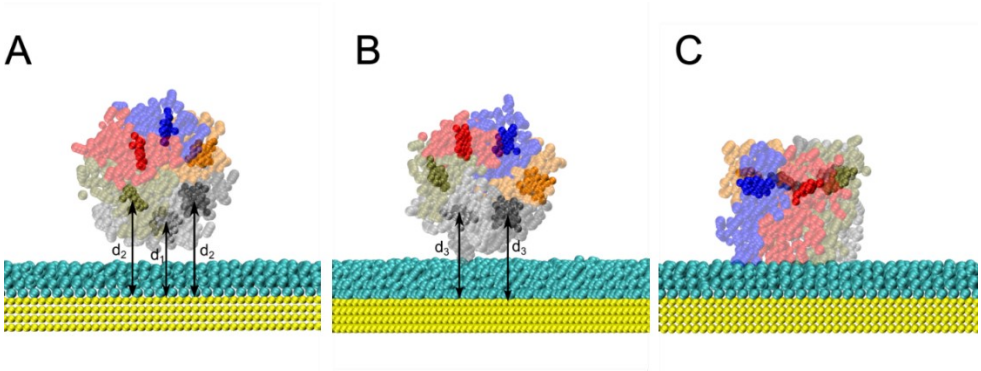

Figure 4.1.6 Two-step adsorption process of fully oxidized HTHP on the SAM. First, HTHP adsorbed in a "wheel-like" orientation (A,B), which subsequently converts to the "reverse disc" orientation (C). Subpanel A shows the case that one heme (heme 1) is in direct electron transfer distance to the gold (d_1 = ca. 22 Å) while two other hemes (heme 2 and heme 6) show larger

[†] Prepared by Dr. T. Utesch (TU Berlin)

distances (d_2 = ca. 32 - 34 Å). In the second case (B), two hemes (heme 1 and heme 6) are in distances (d_3 = ca. 28 Å) allowing slow direct electron transfer. All distances are measured between the central bead of the heme and the gold surface. Gold surface and SAM are colored in yellow and cyan, respectively. HTHP is colored according to its monomers. The protein matrix is indicated as transparent, while the heme cofactors are opaque.

4.1.5 Discussion

The crystal structure of HTHP has been determined to a resolution of 2.5 Å (2OYY).[93] It served as a starting point for the interpretation of the spectroelectrochemical data and the coarse-grained MD simulations carried out in this work.

Heme pocket structure

The RR spectra indicate identical structures and protein-porphyrin interactions for all six hemes, in line with the crystallographic data. Frequencies in the marker band region prove a 5cHS configuration. The vibrational pattern of the spectra is similar to those of other tyrosine-coordinated hemes.[97–99,115,118,121] In particular, a charge transfer band at 620 nm in the electronic spectrum and the presence of the Fe-O^- vibration at the position characteristic of a partially negative charge at the oxygen atom imply Tyr46 as the only axial ligand (Figure 4.1.1).[97] The crystal structure of HTHP shows Arg43 in hydrogen bond distance, which may stabilize the tyrosinate coordination to the heme iron. In this respect, the situation is not only similar to catalases but also to the H32A variant of the HasA heme,[100,122] where the central iron exhibits also an axial Tyr coordination with a His as hydrogen bond partner, or to the HmuT heme transporter, where a hydrogen bond interaction with heme ligated Y235 was recently found.[98] In fact, RR spectra of the H32A variant of the heme transporter proteins HasA and HmbR also reveal a very intense ν_3 band as observed in HTHP, although its intensity does not exceed that of the ν_4 band.[97] The situation changes in the ferrous state. Here, the electronic spectrum does not show a clear charge transfer band as in the ferric state, which indicates a weakening of the Fe-O bonding strength. In line with this interpretation is the observed 6 cm^{-1} downshift of the Fe-Tyr vibration in the RR low frequency spectrum upon reduction of the protein. Such a weakening of the bond after heme reduction can be rationalized as the negative charge of the oxygen atom does not further stabilize the reduced iron, which could result in slight repulsion of Tyr as an axial ligand either by elongating the bond or changing the coordination angle.[97,123] Indications for a Tyr ligation can also be derived from the electronic spectra since the 555 nm 590 nm absorption bands are similar in position as observed for catalase-related allene oxide synthase cAOS and peroxidase MAP which both include Tyr-O(H)-Fe(II) ligation.

Redox potentials

The potentiometric titration of HTHP in solution afforded a redox potential of –0.54 V. This value holds for all six hemes, consistent with the crystal structure that displays the same heme-protein interactions in each monomer. The heme is solvent-exposed with the propionate side chains pointing into the solution phase. This structural feature may in part account for the negative redox potential, which is still lower by ca. 0.1 V than the redox potentials of high-spin iron porphyrins in aqueous solution.[124] Most likely, it is the unique tyrosinate ligation that provides substantial electron density to the heme and, therefore, stabilizes the ferric state. Thus, major structural changes at the redox site including an alteration of the ligation pattern or changes in the protonation states of the heme propionates have to be taken into account to rationalize the significant redox potential upshift by ca. 0.38 V determined for the immobilized HTHP by CV.

The two redox potentials determined in the SERR experiments of covalently bound HTHP are closer to the redox potential of the protein in solution. The value for the redox couple I is only more positive by 50 mV (i.e. –0.49 V) which may partly be due to the relatively large error margin of the SERR spectroscopic analysis and partly reflect the potential drop across the SAM/solution interface. The even more positive redox potential of state II (–0.43 V) points to a structural difference compared to the hemes of the native HTHP in solution, which is in fact supported by the different ν_4 frequency (1357 vs 1359 cm^{-1}). Such a shift might be attributed to a change of Tyr coordination, which could be initiated by the observed weakened Fe-O interaction and it might precede the release of the heme to the bulk solution. The ca. 25% irreversible loss of SERR intensity at very negative potentials, which was observed for both the electrostatically bound and the covalently attached HTHP, supports the hypothesis of heme release upon electrochemical reduction in immobilized state. The potential-dependent SERR spectra of electrostatically bound HTHP allows identifying two redox transition around –0.1 and –0.4 V but due to the low signal-to-noise ratio these values mark only the approximate ranges of the respective redox potentials.

High-potential redox transition in the wheel configuration

The unprecedented variety of redox potentials determined for HTHP in the immobilized state by CV and SERR spectroscopy and their substantial differences to the redox potential in solution can be related to different modes of protein adsorption. Let it first consider the well-defined single redox transition at −0.17 V in the CV experiments. These results are similar albeit not identical to those of the previous study on HTHP on SAM-coated Au electrodes[96]. In that work, HTHP was electrostatically immobilized at high ionic strength and the redox potential was slightly more negative (ca. -0.23 V vs. −0.17 V) than observed in the present study. Moreover, the authors reported a distinctly higher current density, which was interpreted in terms of a complete reduction of all six hemes of HTHP adsorbed in a disc orientation. For SAM-coated Ag electrodes, electrostatic binding was impaired at high electrolyte concentrations and found to occur only at very low ionic strength (2.5 mM), which together with the much lower current density, points to a different adsorption behavior of HTHP for SAM-coated Ag and Au electrodes. This might be related to the quite different potentials of zero charge that are more negative for Ag than for Au.[125,126] As a result different electrostatic interactions between the protein and the electrode surface are expected that lead to a different surface affinity of the protein and shifts of the redox potential.

The electron transfer rates derived from the CV experiments imply that this transition solely originates from hemes in close distance to the surface, corresponding to the wheel orientation whereas the reverse-disc orientation can be ruled out. In the wheel orientation, only one out of the six hemes can be in an electron transfer distance (ca. 22 Å distance between the heme center and the electrode surface; Figure 4.1.6A) that may account for the observed kinetics. However, prior to the heterogeneous electron transfer, this redox site must undergo a structural change that causes the upshift of the redox potential from −0.54 to −0.17 V. This structural change is likely to be related to the specific surrounding of the heme that faces the electrode in the wheel orientation. Specifically, the heme propionates which are solvent exposed and thus deprotonated for HTHP in solution,[127] may be protonated upon contacting the SAM, thereby accounting for the increase of the redox potential. In fact, electrostatic calculations for the four-heme Cyt c subunit in photosynthetic reaction centers revealed redox shifts between 0.16 and 0.41 V, depending on the protonation state of the heme propionates,[14] which are in the range of the changes observed in the present work. Alternatively or additionally, weakened Fe-Tyr interaction could precede an axial ligand exchange, possibly by the adjacent Arg which may cause comparably large redox potential shifts, such as the replacement of Met by a Lys or

a His in cytochrome c, or water by a His in cytochrome P450.[128–130] Regardless of the nature of the underlying structural changes, it is tempting to assume that this structural change is brought about the local electric field at the SAM/protein interface, as it was also observed for other heme proteins such as cytochrome c, cytochrome P-450, or cytochrome c_3 with or without ligand exchange.[129–131] Electric-field induced ligand exchange occurs within milliseconds, as shown for cytochrome c,[132] and changes of the propionate protonation state may even be faster. Since the time constants for the rotational diffusion of electrostatically bound proteins is expected to be in the microsecond to short millisecond range,[133] it may well be that all hemes of the HTHP in the wheel orientation contribute to the CV signal.

Due to the short separation from the electrode and the more perpendicular orientation of at least one of the hemes, SERR spectroscopy should preferentially probe HTHP in the wheel configuration. However, the SERR spectra of the electrostatically bound protein include only a rather small spectral contribution of hemes with a redox transition at around −0.1 V that, within the large error margin, may correspond to that observed in the CV. Thus, it can be concluded that either only a relatively small fraction of the immobilized HTHP is present in the wheel orientation or that the wheel orientation is only transiently adopted for a comparably short time. The failure to detect spectral differences between differently coordinated hemes is certainly due to the poor signal-to-noise ratio and the very low contribution of the structurally perturbed heme, i.e. one out of six hemes of the wheel orientation which, in addition, is much less populated than the reverse disc population.

The covalently bound HTHP seems to display a similar orientational distribution, although the high-potential transition can only be detected in the CV but not in the SERR experiments. It might be that cross-linking slightly favors the reverse disc orientation. Note that single covalent attachments sites are expected to retard but not fully impair rotational diffusion[119] which may account for the broadened CV signal.

The conclusions derived from the CV and SERR experiments are not in full agreement with the CG MD simulations, which revealed the “reverse disc” as the only stable configuration, whereas the “wheel” orientation is only adopted in the initial phase of adsorption. However, transition from the reverse disc to an at least transient wheel orientation that is probed in the experiments may occur on time scales which are not accessible even when using coarse graining models. Further, other shortcomings of these models may be considered. For example, the MARTINI force field is overestimating hydrophobic interactions[134] which may result in

increased stability of the “reverse disc” conformation and may prevent a tilting toward the “wheel”. Other points that are inevitably neglected in our model are changes in the protonation pattern upon adsorption, changes upon the applied potential, and defects in the SAM or gold film which could act as hotspots for protein immobilization. Most important, however, is the fact that adopting the reverse disc orientation is accompanied by structural changes at the adsorption site, which are likely to affect the adsorption properties. Specifically changes of the protein structure involving the rupture and formation of (coordinative) bonds cannot *per se* be described by the present simulation techniques.

Low-potential redox transitions in the reverse disc configuration

Despite the failure of the CG MD simulations to account for a minor fraction of HTHP in the wheel configuration, the theoretical predictions of the reverse disc orientation as the main fraction of the adsorbed HTHP is in line with the experimental findings. In the reverse disc orientation, the redox sites do not experience any electrostatic interactions with the SAM surface and should therefore display a redox potential similar to that in solution. Consequently, the hemes with a redox transition at –0.49 V observed in the SERR spectra are attributed to structurally unperturbed hemes of the reverse disc orientation. The discrepancy with respect to the value in solution (–0.54 V) may partly be due to the error associated with the SERR spectra analysis and partly to the potential-drop across the electrode/SAM/solution interface.[135] Taking into account that distance-dependent attenuation of the surface enhancement, the yet appreciable contribution of these hemes to the SERR spectra confirms the prediction of the reverse disc as the prevailing orientation.

In this orientation, electron exchange with the electrode is, on the first sight difficult to understand since the average distance of the hemes to the electrode is ca. 40 Å, thus much too large for electron tunneling. However, careful inspection of the structure reveals several aromatic amino acids in between the heme and contact region to the SAM. Six of them, W5, H63, F18, F64, W74, and Y73 may be involved in an electron hopping mechanism to allow, at least, for a slow electron transfer between the heme and the electrode (Fig. 6.1.6, Appendix).[74] The overall electron transfer in this configuration is evidently too slow for detection in the CV (< 1 min) but sufficiently fast to be observed in the SERR spectroscopic measurements (> 5 min). Furthermore, the proposed hopping mechanism is not very efficient since there is a considerable fraction of non-reducible hemes that are detected in the SERR experiments even at very negative potentials.

Implications for the function of HTHP

The physiological function of HTHP is not known. In the first investigation of HTHP in solution, peroxidase and catalase activity was demonstrated.[93] A previous electrochemical study revealed also peroxidase activity for the immobilized HTHP although the catalytic process seems to refer to the structural perturbed high-potential heme (ca. −0.23 V) and was suggested to run via the intermediate formation of a ferrous heme.[96] This mechanism is in contrast to the reaction cycle in solution, which does not include the structurally perturbed heme and its transient reduction[93]. Such variability in terms of mechanism and active site structures would be quite surprising for an enzymatic process. As an alternative interpretation one may attribute the catalytic activity of the immobilized HTHP to the hemes (partially) released from the protein. Then the CVs in the presence of H_2O_2 as shown by Peng et al.[96] would represent the superposition of the redox transition of the high-potential hemes and catalytic response of the loosely bound or free iron porphyrin. In fact, the present results suggest that HTHP tends to release hemes when binding to the SAM-coated electrode. This conclusion can be drawn from the ca. 25% loss of intensity during the SERR spectroscopic experiments which cannot be attributed to desorption of the protein since it is observed for both the covalently and electrostatically bound HTHP. This interpretation does not argue against HTHP´s natural function as is a (bifunctional) catalase-peroxidase enzyme. In this context we like to refer to other heme transporters like the hemophore HasA from *Pseudomonas aeruginosa*[122], the heme transporter HmuT from *Corynebacterium diphtheriae*[98], the hemoglobin receptor HmbR from *Neisseria meningitides*[97] and the heme-binding protein ShuA from *Shigella dysenteriae*[99]. In all these proteins, the heme exhibits a very similar structure with a tyrosine serving as an axial ligand. Here the oxygen atoms carry a partially negative charge, often enhanced by hydrogen bond interaction with a neighboring amino acid. Indeed, it was proposed the tyrosine ligation is responsible for heme uptake in HmuT which can provide high heme binding stability.[98] As shown by presented results, reduction of the iron could weaken the coordination with the Tyr and could be a starting point for heme release in the heme transport pathway. A similar situation could be present in HmbR and HasA, where the former is involved in hemin progression and the latter as well is responsible for heme uptake in extracellular space and releases the heme after binding to a specific receptor on the bacteria cell surface.[136] Summarizing the observations, it is tempting to assume that HTHP serves as a heme carrier. Following this hypothesis, any conclusion concerning a redox-linked heme release in HTHP would be premature, however. Other trigger mechanisms for heme release like protein-receptor or protein-membrane interactions are possible and should be further investigated in the context of the heme transporting hypothesis.

4.2 Spectroscopic observation of calcium-induced reorientation of cellobiose dehydrogenase immobilized on electrodes and its effect on electrocatalytic activity[60]

4.2.1 Abstract

Cellobiose dehydrogenase catalyzes the oxidation of various carbohydrates and is considered as a possible anode catalyst in biofuel cells. It has been shown that the catalytic performance of this enzyme immobilized on electrodes can be increased by presence of calcium ions. To get insight into the Ca^{2+} induced changes of the immobilized enzyme surface enhanced vibrational (SERR and SEIRA) spectroscopy together with electrochemistry were emplozed. Upon addition of Ca^{2+} ions electrochemical measurements show a shift of the catalytic turnover signal to more negative potentials while SERR measurements reveal an offset between the potential of heme reduction and catalytic current. Comparing SERR and SEIRA data it is proposed that binding of Ca^{2+} to the heme induces protein reorientation in a way that the electron transfer pathway of the catalytic FAD center to the electrode can bypass the heme cofactor resulting in catalytic activity at more negative potential.

4.2.2 Introduction

Cellobiose dehydrogenase (CDH) is a flavocytochrome which was found to be involved in wood degradation. It was first discovered in 1974 by Westermak and Eriksson who reported a cellulose degradadation and reduction of some reactans by extracellular redox active enzyme obtained from funghi and named it cellobiose oxidase.[137] However, later it was shown that iron containing compounds and quinones have higher affinity to the enzyme than molecular oxygen, renaming it to cellobiose dehydrogenase (EC 1.1.99.18).[138] To this end, CDHs were found to be secreted by white-rot, brown-rot, plant-pathogenic and composting funghi from the dikaryotic phyla, under cellulolytic conditions, when cellulose is the major carbon source in parallel with cellulases and hemicellulases. In general, they can be divided into two classes, Basidiomycete (class I) and Ascomycete (class II). Apart of their origin, CDHs from these different classes differ in catalytic activity. Due to the fact that ascomycetes are less capable of rapid wood degradation, being more suitable for degrading the wood in more harsh conditions like higher temperatures, wider range of pH and humid environment, enzymes from this class found to be able to oxidize bigger variety of carbohydrates. [139]

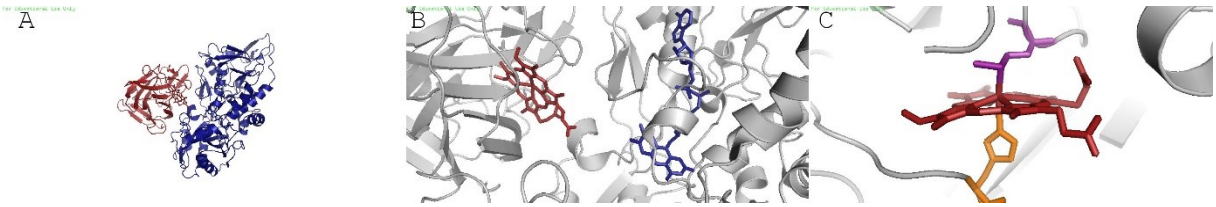

Figure 4.2.1 The crystal structure of *Mt*CDH (PDB ID: 4qi6) representing (A) cytochrome domain coloured in red and flavin domain coloured in blue, (B) heme cofactor colored in red and FAD cofactor coloured in blue, (C) heme axially coordinated by His residue coloured in orange and Met residue coloured in purple.

The structure of monomeric cellobiose dehydrogenase comprises two domains, a larger FAD containing domain, and smaller cytochrome containing domain (Fig. 4.2.1) The heme belongs to heme b class of cytochromes, with proximal His and distal Met axial coordination, forming a 6cLS state that is conserved in all classes of CDH (Fig. 4.2C). [140] Their catalytic function involves oxidation of many carbohydrates, like cellobiose, cellodextrins, maltose, lactose, glucose, lactose, diphenolic compounds and catecholamines, such as dopamine, adrenaline and noradrenaline in a presence of electron acceptors.[141] The enzyme exhibits highest substrate specificity for cellobiose, with K_M values ranging from 0.01 (*Mt*CDH at pH 6.0[142]) to 0.29

(*Cu*CDH at 4.5[143]) and turnover rates (k_{cat}) of 13 and 19, respectively. During this process, substrate binding to the flavin domain reduces the FAD cofactor with two electrons, which can be further transferred to two-electron or one-electron acceptors or via internal electron transfer (IET) to the heme cofactor, which serves as an electron sink (Fig. 4.2.2). Alternatively, electrons are transported to the heme cofactor via internal electron transfer (IET). From here, electrons can reduce external acceptors like cytochrome c. It was shown that the rate of FAD reduction reaches 70 s^{-1}, whereas the reduction rate of the heme cofactor via IET process is slower (48 s^{-1}).[144] Although there are different pathways for electrons to pass through the protein, the presence of the cytochrome domain enhances the reduction of one-electron oxidants.[145] CDHs belonging to class II, as studied in this work (*Mt*CDH) are characterized by best performance in pH range of 4.5 – 6.0 and temperature range of 45° C – 75° C.[142] Due to their substrate specificity and broad range of environmental conditions they are recognized as good biocatalysts for development of new classes of biodevices.

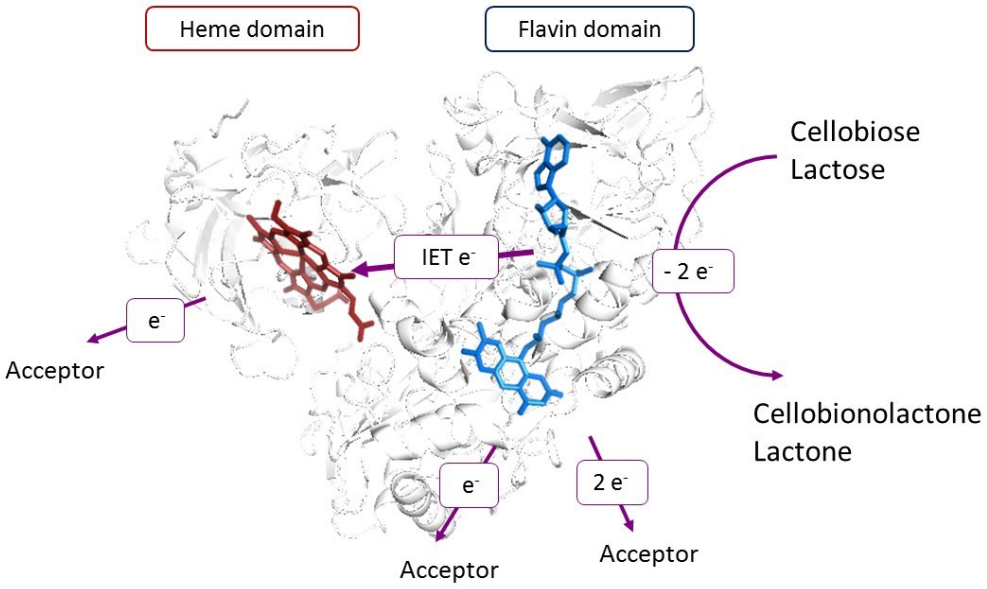

Figure 4.2.2 Simplified catalytic reaction of cellobiose dehydrogenase oxidizing cellobiose to cellobionic acid with marked possible pathways for electron/s donation.

In order to better appreciate the advantage of this enzyme for third class glucose biosensors, a short summary of biosensor development will be described briefly. First time entrapping an enzyme on an electrode to serve as a biological recognition element in a technological device, defined now as biosensor, was achieved by Clark and Lyons in 1962.[146] They used glucose oxidase (GO_x), an enzyme catalysing oxidation of glucose to gluconic acid, in presence of oxygen. What was monitored that time, was the oxygen consumed during the reaction in

amperometric device in which applying a reductive potential to the platinum cathode led to the subsequent conversion of oxygen to water (see Fig. 4.2.3). This device was quickly transferred to industry which resulted in the first launched glucose analyser. It has to be noted that electrochemical glucose biosensors are a leading concept for this most commonly tested analyte, accounting for *ca*. 85 % of the entire biosensor market.[147] However, since this class of device relies on the constant use of oxygen as physiological electron acceptor, fluctuations of oxygen tension can cause a significant errors.[148] Additionally, detection of hydrogen peroxide requires applying potentials at which other oxidizable constituents present in human blood are active and can affect selectivity of the measurement. Overcoming these drawbacks was addressed in second class of biosensors, in which different methods of establishing electronic contact between a redox active site of an enzyme and the surface of the electrode were developed and tested. The best or most common one include mediators, which indirectly facilitate electronic communication by shuttling electrons from the protein to the electrode (see Fig. 4.2.3). In spite of providing a reasonable solution, mediators are often toxic, hardly soluble or chemically unstable. This led to the development of third class of device which can operate without additional mediators and at low potentials close to the redox transition of the redox protein (see Fig. 4.2.3). In search of a suitable enzyme, CDH together with horseradish peroxidase HRP, superoxide dismutase SOD, alcohol dehydrogenase ADH and fructose dehydrogenase FDH were promising candidates fulfilling the requirements for efficient DET in multifaced electronic applications.[29,141] CDH exhibits a cytochrome domain as built-in mediator and anchor of the enzyme to the electrode and thus is especially attractive for technical biodevices. Furthermore, due to its high adaption to environmental conditions, the ET process can be pH (optimum range pH 4 – pH 8) and temperature modulated. Similarly, the same reasons make the enzyme attractive for development of enzymatic biofuel cells, in which glucose could be used as a fuel.[149] Hence, the enzyme gained a particularly high scientific interest in the field of bioelectrochemistry over the last 20 years, in which fundamentals of internal electron transfer of CDH were addressed, as well genetic modifications with a purpose of improving oxidizing properties of the biocatalyst and finally finding suitable type of electrodes for high loading and proper orientation of the enzyme.[141,150]

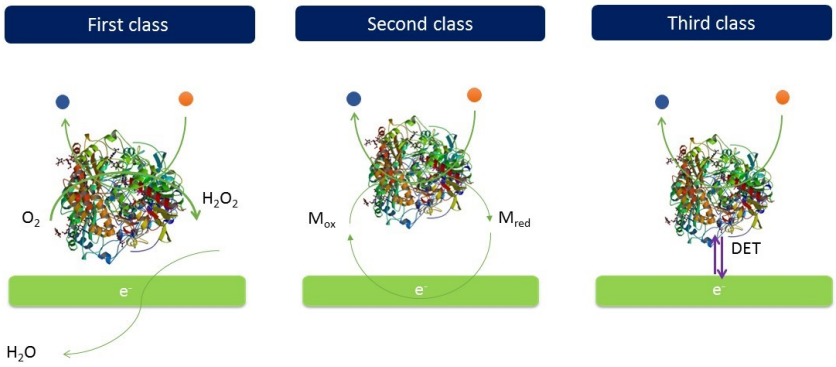

Figure 4.2.3 Summary of classes of biosensors utilizing an enzyme as a biological recognition element for glucose detection. First class is based on use of oxygen, second class on mediators providing ET contact with an electrode and third class utilizes established direct ET between the redox site and the electrode.

When CDH is attached to the electrode, different electronic pathways from the redox center to the electrode can be imagined. Upon gaining two electrons from the substrate, electrons could be already donated from the flavin, or alternatively could be first transported to the cytochrome domain via IET and then reach the electrode (see Fig. 4.2.2). Whereas DET between the partially solvent exposed heme and the electrode can be facilitated, the flavin center, which is buried inside the protein matrix, requires mediators to shuttle electrons to the electrode surface.[141] For instance, osmium complexes (Os^{3+}) or benzoquinone can be used as one-electron or two-electron mediators, respectively.[141] Depending on their redox potential they can compete with DET by accepting electrons from the heme cofactor. First investigations of HET of *Ps*CDH immobilized on a graphite electrode revealed low surface coverage of *ca*. 5-50mM/cm^{-1} hindering the detection of the DET response in the electrochemical experiment in absence of substrate.[141] Hence, further studies focused on enhancing the effective electrode area for CDH binding or providing suitable orientation of the immobilized enzyme. This has been achieved by using different types of enzymes which could be bound to different kinds of electrodes like *Nc*CDH on graphite[151], *Ps*CDH on single-[152] and *Tv*CDH on multi-walled carbon nanotubes[153], *Ps*CDH on glassy carbon[154], *Tv*CDH, *Ps*CDH and *Mt*CDH on gold[155] and *Pc*CDH on gold nanoparticles[156]or, as presented here, *Mt*CDH on silver[60]. Naturally, experiments additionally differ in the surface modification for CDH binding in order to provide a surface charge suitable to interact and stabilize a proper orientation of the enzyme

for DET. Overall, the current density reached values in a range of 0.5 μA/cm^{-1} to 500 μA/cm^{-1}, being the highest for -NH_2 functionalized surface[150].

Another method to improve electrochemical efficiency of electrostatically bound biocatalysts on electrodes is modulation of ionic strength conditions. Increasing ionic strength conditions can result in faster heterogeneous ET rates, which is often interpreted as an effect of increased mobility of the protein as a result of modified protein surface electrostatics, increasing the probability of adapting suitable orientation for faster ET kinetics.[157,158] Moreover, the presence of metal ions itself can have different effects on protein stability and activity. As shown by Hofmeister, the metal ions are able to differently organize water molecules around them which can have a further impact on protein stability.[159,160] Alternatively, ions can interact with charged groups of amino acids from protein backbone. In this respect, it is often crucial if mono- or divalent metal ions are used. This binding or interaction can directly induce a conformational change of the protein. For instance, divalent cations such as Ca^{2+}, Mn^{2+} or Mg^{2+} were shown to lead to a conformational relaxation of integrin α5β1.[161] Such a conformational change could as well directly enhance the reactant-product transition probability in the electron transfer mechanism.[74,162]

One representative of CDH is produced by the ascomycete fungus *Myriococcum thermophilum*; (*Mt*CDH) a thermotolerant saprophyte[163] It is known from previous reported investigations that *Mt*CDH can be successfully immobilized on different kind of electrodes (graphite[164,165], or gold[166]) while retaining good catalytic activity. In the absence of natural redox partners electrons are believed to be transferred almost exclusively via a heme redox transition to the electrode.[167] It was shown that at pH5.5 after addition of 5mM sugar (lactose, cellobiose) CDH reaches its maximum catalytic rate. Moreover, increasing the ionic strength of the buffer increased the catalytic activity of immobilized *Mt*CDH.[164,168] Surprisingly, the effect was much more pronounced for the di-valent cation salt $CaCl_2$ than for monovalent cation salts such as KCl.[165,168] It has been proposed that specific binding of Ca^{2+} ions either influence the intramolecular- or the heterogeneous electron transfer properties,[168] however, no final conclusions could be drawn up to now.

Vibrational spectroscopy gives detailed information about molecular structure. In Raman spectroscopy, inelastic scattering of monochromatic light by the molecule is analyzed. Under Resonance Raman (RR) conditions, where the frequency of the source light is close to the frequency of an electronic transition, structural changes of a chromophore are selectively

probed. This approach has been widely used to study the heme cofactor in heme-proteins using violet light excitation. On the contrary infrared (IR) spectroscopy is mainly used to determine the secondary structure of proteins, which is given by the geometry of the peptide backbone.

In surface enhanced vibrational spectroscopy locally enhanced electric fields at the surface of noble metal nanostructures are used to selectively monitor the vibrations of surface bound molecules. In combination with electrochemistry surface enhanced resonance Raman (SERR) and surface enhanced infrared absorption (SEIRA) spectroscopy are powerful techniques to study structure-function relationships of enzymes on surfaces.[169] SERR and SEIRA measurements have been individually applied in the past to study the redox and catalytic properties of various enzyme/electrode systems.[116,170–174] In this work, both vibrational spectro-electrochemical techniques have been employed on the same enzyme to investigate the influence of monovalent Na^+ and divalent Ca^{2+} ions on the electron transfer pathway of surface-bound *Mt*CDH. SERR spectroscopy (SERRs) provides detailed insight into the structure and redox behavior of the heme located inside the cytochrome domain and its communication with the electrode, while the SEIRA signal is dominated by the vibrations of the protein backbone. Complementary SEIRA and SERR spectroscopic measurements therefore provide unique information about possible changes in the orientation of the immobilized enzyme. Finally, electrochemical measurements reveal valuable information about the overall catalytic activity of immobilized *Mt*CDH.

4.2.3 Experimental Section

Materials

Poly(diallyldimethylammonium chloride) solution (PDADMAC) was purchased from Sigma Aldrich(Steinheim, Germany). Lactose was provided by Sigma Aldrich and used as a substrate for catalysis. CDH from *Myriococcum thermophilum* was expressed and purified as described previously.[142] As measuring buffers 50 mM and 200 mM acetate at pH5.5 were used. Since acetate exhibits a pK_a of 4.76, the pH was further adjusted with NaOH to reach the final pH of 5.5. In the further analysis we discuss this condition as the one in presence of monovalent Na^+ ions. Optionally, $CaCl_2$ salt in a concentration between 5 – 50 mM was added to 50 mM acetate buffer. $CaCl_2$ was provided by Sigma Aldrich. The water used in all experiments was purified by a Millipore system (Bedford, MA, USA).

Electrochemistry and Surface Enhanced Resonance Raman Spectroscopy

SERR and electrochemical measurements were performed with the CDH modified silver electrode mounted in a three-electrode electrochemical cell in different buffers. During the measurement the sample was flashed with Argon and rotated constantly. Cyclic voltammograms were recorded using a CH 600E potentiostat in a potential range of -300 – 100 mV vs. Ag|AgCl (3 M KCl). All experiments were done at room temperature.

Chronoamperometric measurements were recorded using a CH 600E potentiostat. The electrode was rotated applying 360-1140 rpm. 250µl of lactose and 250µl of $CaCl_2$ solution was added to the cell to reach final concentrations of 10mM each.

SERR measurements were performed using the 413 nm laser line of a Krypton Ion Laser (Coherent Innova 300 c). The spectra were recorded at room temperature with a confocal Raman Spectrometer (LabRam HR-800, Jobin Yvon) using 250 µW laser power for continuous wave (CW) measurements and 500 µW laser power for measurements using pulsed laser illumination (PW). CW SERR spectra were accumulated three times 10 s each and averaged, PW SERR spectra were accumulated two times 1 min each and averaged. During the measurement the electrode was rotated to avoid photo-reduction.

Surface Enhanced Infrared Absorption Spectroscopy

SEIRAs measurements were performed with a Kretschmann-ATR configuration using a Silicon-crystal under an angle of incidence of 60°. The SEIRA spectra were recorded between 1000 - 4000 cm^{-1} with a spectral resolution of 4 cm^{-1} on a Bruker Tensor 27 spectrometer, equipped with a liquid nitrogen cooled photoconductive MCT detector. 400 scans were co-added for each spectrum. Electrode potentials were applied by a Metrohm PGSTAT 101 Autolab potentiostat under control of NOVA 1.9 software. All potentials in the paper are refered to the Ag|AgCl (3M KCl) electrode (+0.21 V vs SHE).

4.2.4 Results

Electrochemistry

Cylindrical electrodes (3 mm height and 5 mm in diameter) suitable for SERRs and electrochemistry were made of silver and prepared by polishing the solvent exposed surface with sandpaper and subsequent electrochemical roughening via repetitive oxidative and reductive steps.[102] The electrodes were incubated in a Poly(diallyldimethylammonium chloride (PDADMAC) solution for 10 min, which served as a functional coating for protein immobilization.[175] Subsequently, the electrode was rinsed with water and dried.

Enzyme attachment was achieved by incubating the coated electrode in 700 µl of a 0.33 µM *Mt*CDH in 50 mM acetate solution at pH 5.5 for 1h at room temperature. During incubation the electrode was rotating at 360 rpm. Binding of *Mt*CDH under these conditions is expected to occur due to the electrostatic attraction of the negatively charged CYT domain and the positively charged PDADMAC.

For spectro-electrochemical measurements the silver electrode was incorporated into a three-electrode electrochemical cell as working electrode. A Pt wire functioned as counter and an Ag|AgCl (3 M KCl) electrode as reference electrode.

Cyclic voltammograms of immobilized *Mt*CDH under non-turnover and turnover conditions (10mM lactose) were recorded at a scan rate of 2 mV/s and 100mV/s, respectively, while the electrode was slowly rotated at 360 rpm to keep the same conditions as in the SERR experiments. Measurements were performed in different acetate buffer concentrations (50 – 200 mM) and in presence of $CaCl_2$ (5 – 50 mM). No redox peaks were recorded under non-turnover conditions although SERRs and SEIRAs measurements confirmed the presence of CDH on the electrode. However, in the presence of lactose as substrate a clear catalytic current was observed (Figure 4.2.4A). The turnover signal was fitted by a sigmoidal function taking the average of the forward and reverse scan. This yielded an inflection point (IP) at -72 mV (See also Table 4.2.1), which will be in the following used as a value to characterize the potential dependence of the catalytic current. Furthermore, the open circuit potential decreased from 100 mV to 17 mV upon addition of lactose.

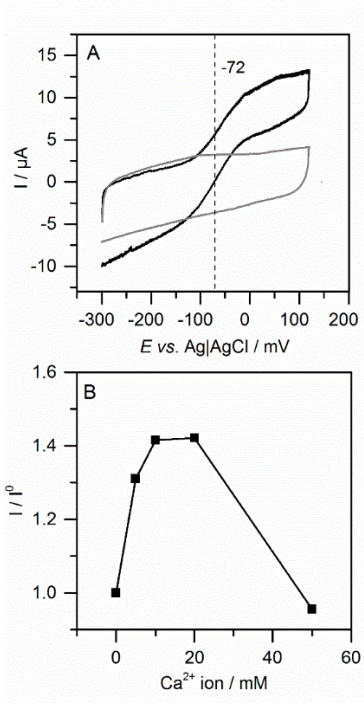

Figure 4.2.4. A: Cyclic voltammograms of *Mt*CDH recorded under non-turnover (grey) and turnover (10mM lactose, black) conditions in 50 mM pH 5.5 acetate buffer. The inflection point potential is indicated by a dashed line. The scan rate was 2 mV/s. B: Increase in electrocatalytic current at 0 mV (*vs. 3 M* Ag|AgCl) of immobilized *Mt*CDH in presence of lactose as a function of Ca^{2+}- ion concentration. The current (I^0) in the absence of Ca^{2+} ions was used as reference.

The size and shape of the electrochemical turnover signal showed a strong dependence on the ion concentration in solution (Figure 4.2.5 A-C). In general, upon increasing the concentration of mono- (Na^+) and di-valent (Ca^{2+}) ions in solution, the catalytic current curves were shifted to more negative potentials. Mostly due to this shift higher catalytic currents were measured for higher ion concentrations at an applied voltage of 0V. In the case of monovalent Na^+ ions the electrocatalytic current increased by 45 % upon changing the ion concentration from 50 to 200 mM. Interestingly, the same increase in catalytic activity could be reached for much lower ion concentrations if divalent Ca^{2+} ions were added to the buffer solution instead (Figure 4.2.4B). Already for Ca^{2+} concentrations below 10 mM a significant increase in catalytic current was observed which reached a maximum at 20 mM Ca^{2+}. Higher concentrations of Ca^{2+} did not improve the catalytic performance. For 50 mM Ca^{2+} the catalytic current even fell below the value that was observed in the absence of Ca^{2+}.

Addition of either 150 mM Na^+ or 20 mM Ca^{2+} resulted in a comparable shift in the turnover signal to more negative potentials (Figure 4.2.5B, C and Table 4.2.1) yielding inflection points of -92 mV and -100 mV, respectively (dashed vertical lines in Figure 4.2.5 B and C). This behavior was also reflected by a shift in the open circuit potential to -10 mV and -55 mV, respectively.

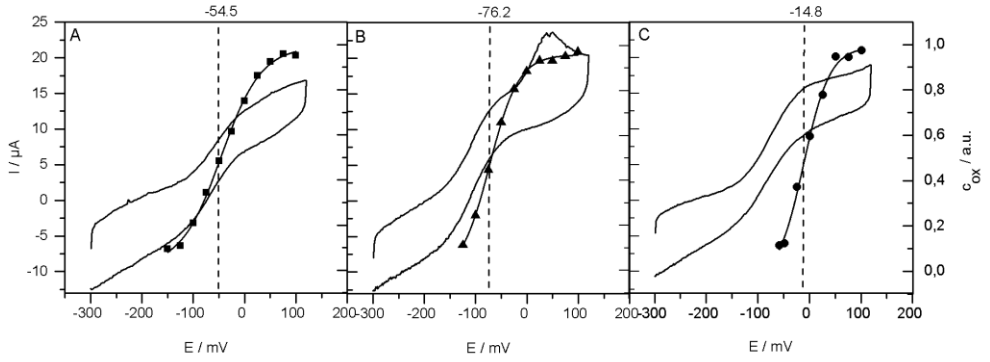

Figure 4.2.5 Cyclic voltammograms of *Mt*CDH under turnover conditions (10 mM of lactose, scan rate 100mVs^{-1}) Measurements were taken in A: 50 mM acetate buffer; B: 200 mM acetate buffer; C: 50 mM acetate buffer + 10 mM $CaCl_2$ buffer. Lines with symbols represent redox titration curves obtained from SERR measurements of immobilized *Mt*CDH in the absence of lactose, fitted by Nernst equation.nst fit of the data. Dashed lines (- - -) refer to the redox potential of the heme obtained from SERRs.

SERR measurements

To investigate the function of the heme cofactor in the catalytic cycle of *Mt*CDH/electrode systems, SERR measurements of *Mt*CDH illuminated with a 413 nm laser were recorded (Figure 4.2.6). The SERR spectra revealed the characteristic vibrational modes (ν_4, ν_3, ν_2, ν_{10}) of a 6-coordinated low spin *b*-type heme cofactor[176] supporting the proposed immobilization of *Mt*CDH on PDADMAC coated electrodes via the heme domain. At positive potentials (100 mV), the oxidation sensitive marker band (ν_4) was found at 1370 cm^{-1}, corresponding to a ferric form of the heme (Figure 4.2.6A). At an applied potential of -200 mV, the ν_4 band down-shifted to 1362 cm^{-1} revealing complete reduction of the heme (Figure 4.2.6B). The redox transitions were found to be completely reversible (data not shown). When the substrate lactose was added at open circuit conditions the heme became fully reduced indicating that the protein remains catalytically active and the intra-domain electron transfer is preserved upon immobilization (Figure 4.2.6C). All spectra are in good agreement with the one presented by Cohen et al.[176]

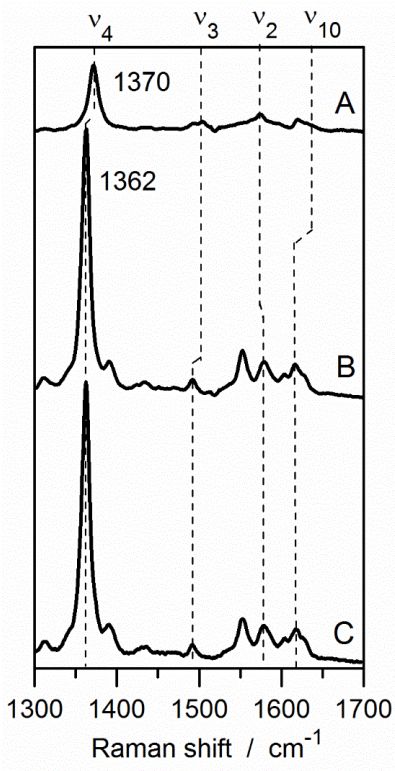

Figure 4.2.6 High frequency SERR spectra of *Mt*CDH immobilized on silver electrodes at: A: 200 mV; B: -200 mV; C: at open circuit potential after addition of 10 mM lactose. The characteristic vibrational modes of heme are indicated by dashed lines.

Potential dependent SERR measurements made it possible to determine the relative intensities of the oxidized and the reduced heme species at a given applied potential. Here complete component spectra of the ferric and ferrous form of the heme were fitted to the spectra. To transform the SERR intensities into relative concentrations the Raman cross sections for ferrous and ferric heme *b* were calculated via component analysis, as described previously.[158] This procedure yielded the molar fraction of oxidized heme (x_{ox}) as a function of potential shown in Figure 4.2.5 D-F. From the so spectroscopically derived redox titration curves -fitted by the Nernst equation- the formal potential of the heme ($E^{\circ\prime}$) and the apparent number of transferred electrons could be determined. At a 50 mM buffer concentration in the absence of Ca^{2+}, the $E^{\circ\prime}$ of the heme was determined to be -54.5 mV (*vs.* 3 M Ag|AgCl) (Figure 4.2.5D and Table 4.2.1). With respect to this value, we observed a negative shift of *ca*. 22 mV in higher ionic strength (200 mM) (Figure 4.2.5E and Table 4.2.1). The presence of $CaCl_2$ caused a positive shift in the $E^{\circ\prime}$ of *ca*. 40 mV (Figure 4.2.5F and Table 4.2.1). Furthermore, if Ca^{2+} ions were present, the SERR signal decreased significantly at potentials more negative than the $E^{\circ\prime}$ (Figure 4.2.7).

Using time resolved SERR spectroscopy,[102] the relative contributions of the oxidized and reduced species could be monitored as a function of delay time, after a change in electrode potential. Fitting the data with a mono-exponential decay formula, the heterogeneous electron transfer rate k_{HET} between the heme and the electrode was determined for potential jumps from 100 mV to the respective $E^{\circ\prime}$ (Figure 6.2.1, Appendix). Under low ionic strength (50mM) conditions, the rate constant was determined to be 4.6 s^{-1}. Increasing the ionic strength to 200 mM resulted in an almost 3 times faster heterogeneous electron transfer rate whereas the presence of $CaCl_2$ only slightly increased the rate constant (Table 4.2.1).

Table 4.2.1 Redox parameters of *Mt*CDH immobilized on Ag electrodes coated with PDADMAC solution.

Ion concentration	$E^{0'}$ / mV[a]	n[b]	K_{HET} / s^{-1}[c]	*OCP* / mV[d]	*IP* / mV[e]
50 mM ac.*	-54.5 ± 3	0.70 ± 0.01	4.6 ± 0.7	17	-72 ± 8
200 mM ac.	-72.6 ± 6	0.86 ± 0.01	13.54	-10	-92 ± 12
50 mM ac. + 10 mM Ca^{2+}	-14.8 ± 3	0.97 ± 0.03	7.17	-55	-100 ± 14

*ac. stands for acetate buffer. [a] Formal heme potential ($E^{0'}$) [b] number of apparent electrons (n). [a] and [b] were determined by fitting the Nernst equation to the relative intensities of oxidized and reduced species. [c] Heterogeneous electron transfer rate (k_{HET}) between heme and electrode. [d] Open circuit potential (*OCP*) in presence of lactose. [e] inflection point (*IP*) of the CV turnover signal of *Mt*CDH

SEIRAs measurements

Electrodes for SEIRAS were prepared by casting a nanostructured gold island film on the flat, hydrophobic surface of an Silicon-ATR prism via chemical deposition.[157,177]

PDADMAC-coated Au working electrodes were incubated with a *Mt*CDH solution for 1 h with a total concentration of 2 µM in 1 ml. The enzyme functionalized Au-film on the silicon crystal was incorporated into a electrochemical cell as working electrode together with a Pt and a Ag|AgCl (3 M KCl) electrode as counter and reference electrode.

The so derived SEIRA spectrum of immobilized *Mt*CDH revealed the characteristic amide I and amide II bands of a protein (Figure 4.2.7A and 6.2.2 Appendix[174]). The second derivative analysis of spectra allowed us to assign the observed bands in the region between 1630 and 1695 cm^{-1} to the secondary structure elements of the enzyme, mainly exhibiting contributions of α-helices, β-sheets and turns (Figure 6.2.2 Appendix[177]). Moreover, close to the spectral region of amides I and II vibrations we observe also a negative peak, which we assign to the aliphatic C-H bending modes of PDADMAC (Figure 4.2.7A,B and 6.2.3 Appendix[178]). It has to be noted that the overlap of the amide I band with the OH bending mode deriving from water molecules fluctuating within the polymer matrix or bound to the Au surface prevents an absolute quantitative analysis of immobilized *Mt*CDH.

Upon the addition of $CaCl_2$ via buffer exchange the overall intensity of the amide I and II bands of *Mt*CDH spectra increased about 10% (Figure 4.2.7C). However, the ratio between the two amides bands remains nearly unchanged.

Characteristic bands assigned to the aliphatic C-H bending and stretching modes of PDADMAC in the SEIRA spectra decreased only slightly (<5%) upon $CaCl_2$ addition. (Figure 6.2.3, Appendix). Similar changes in forms of decreasing C-H bending intensity upon Ca^{2+} addition is observed in the (difference) spectra with immobilized *Mt*CDH (Figure 4.2.7C).

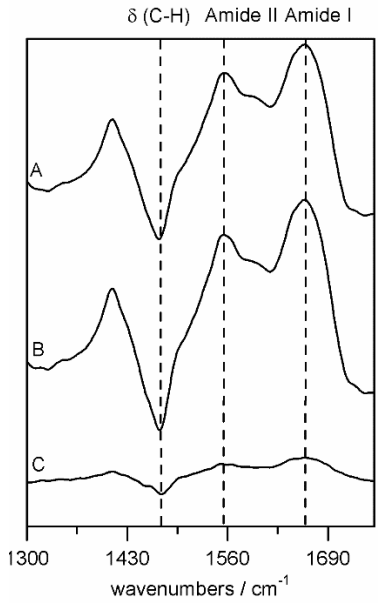

Figure 4.2.7. SEIRA spectra of immobilized *Mt*CDH on gold electrode in: A: 50 mM acetate buffer; B: 50mM acetate buffer + 10 mM $CaCl_2$. C: SEIRA difference spectrum of B-A. The dashed lines indicate the characteristic band positions of the aliphatic C-H bending modes of PDADMAC and the amide I and II vibrations of the protein backbone.

In successive potential-dependent measurements in presence of $CaCl_2$ the intensity of the overall spectrum remains almost unchanged (variations ≤ 5 %). This observation is clearly different to the one derived from SERR experiments, where the spectral intensity drastically decreased at negative potentials by up to 60% (Figure 4.2.8).

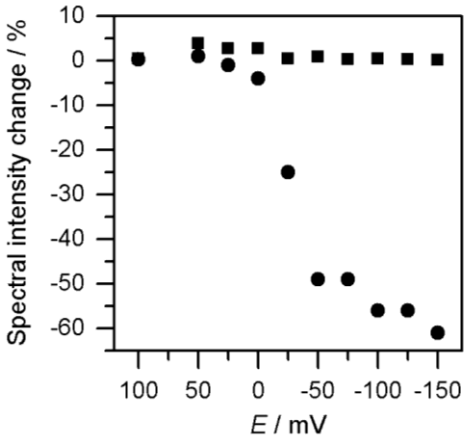

Figure 4.2.8. Potential-dependent spectral intensity changes of the heme of *Mt*CDH immobilized on silver electrode measured with SERRs (●) and the amide I band of *Mt*CDH immobilized on a gold electrode measured with SEIRAS (■). All measurements were done in 50 mM acetate buffer + 10 mM $CaCl_2$.

Finally, the amperometric response of immobilized *Mt*CDH to the addition of lactose and calcium was tested for two different applied potentials. When the potential was set to -54.5 mV (Figure 4.2.9A) addition of lactose lead to an increase in current but subsequent addition of 10mM $CaCl_2$ did not alter this current. Also at an applied potential of -100 mV (Figure 4.2.9B) the current increased when lactose was added. However, in this case upon subsequent calcium addition a further current increase was observed.

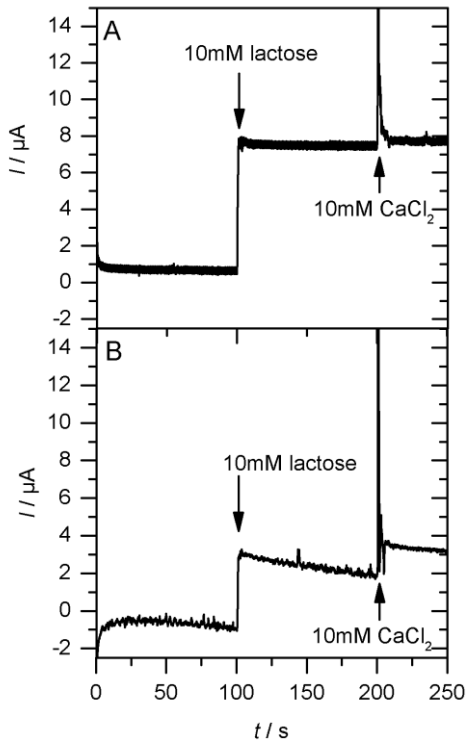

Figure 4.2.9. Current of immobilized *Mt*CDH as a response to addition of substrate and Ca^{2+} ions. During the measurement a potential of -54 mV (A) and -100 mV (B) was applied. The electrode was rotating during the measurement.

4.2.5 Discussion

No noticeable spectral changes were observed between the RR spectra taken in solution and the SERR spectra obtained after protein immobilization. It is therefore concluded that immobilization of *Mt*CDH on a PDADMAC coated silver electrode did not change the native structure of the heme environment. Furthermore, the catalytic activity of the enzyme remains intact also in the immobilized state.

For immobilized *Mt*CDH at high ionic strength conditions the $E^{\circ\prime}$ of the heme was located at *ca.* -76 mV, which is very close to the values that have been determined previously: -81 mV for CDH from *Phanerochaete sordida* at pH5.6, or -75 mV for CDH from *Myriococcum thermophilum* at pH7.0 measured in a thin-capillary type spectroelectrochemical cell.[166,167] For immobilized *MtCDH* measured under low ionic strength conditions, a slightly more positive value of E° at *ca.* -54 mV was determined. This shift can be explained on the basis of strengthened electrostatic interactions between the positively charged polymer and the surface

of the cytochrome domain. At low ionic strength, the positively charged polymer preferentially stabilizes the ferrous form of the heme, which results in upshifting of the $E^{\circ\prime}$.[179] At higher ionic strength (200 mM) the electrostatic interactions of the protein with the polymer are weakened and thus the $E^{\circ\prime}$ coincides with its value in solution.

This interpretation is in line with the observed increase in the heterogeneous electron transfer rate under high ionic strength conditions. The weakened electrostatic interactions between the bound protein and electrode surface may ensure a higher mobility of the cytochrome domain such that the enzyme can adopt orientations that are not favored by electrostatic interactions, but which establish a faster electron transfer pathway.[180]

It has to be noted that these observations are similar to the ones reported in our previous experiments on human sulfite oxidase[158] an enzyme with a cytochrome b_5 (Cyt b_5) domain similar to CDH. In this work increasing the ionic strength of a buffer solution leads to a higher flexibility of the Cyt b_5 domain on the surface resulting in an increase of the $E^{\circ\prime}$, the catalytic current and the heterogeneous electron transfer rate.

The direct comparison of the cyclic voltammograms under turnover conditions and the SERR redox titration under high and low ionic strength conditions shows that in both cases the onset and rise of the catalytic current correlates with the heme redox transition. Although the inflection point of the CV turnover signal was ca. 20 mV more negative than the inflection point of the SERR redox titration –corresponding to the $E^{\circ\prime}$ of the heme- it is reasonable to assume that the electron pathway from the catalytic FAD center to the electrode goes via a heme redox transition.

The presence of Ca^{2+} ions, however, had a different influence on CDH activity. Already at a concentration of 10 mM of Ca^{2+} the catalytic turnover signal of the enzyme was shifted to a more negative potential, therefore a simple increase in the enzyme's flexibility, as in the case of Na^{+}, can be ruled out as a possible explanation. Moreover, Ca^{2+} did not induce significant structural changes of the PDADMAC layer, as the overall intensity of the corresponding SEIRA spectra just slightly (<5%) decreased after addition of Ca^{2+} (Figure 6.2.2, Appendix). A possible explanation of this small effect is an increased permeability of the PDADMAC layer that allows the adsorbed CDH molecules to move slightly closer to the surface without major re-orientation.

Noticeable is the decrease in SERR intensity of the heme bands at potentials below $E^{\circ\prime}$ in presence of Ca^{2+}. Such a decrease can be a result of enzyme desorption. However, SERR and

SEIRA intensity shows a very strong distance dependence that scales roughly with the 12th or 6th power respectively of the molecule's distance to the electrode.[45] Therefore the observed signal decrease can also be attributed to protein re-orientation. Protein desorption or large scale reorientation can be excluded from the SEIRA data as in this case either a Ca^{2+} induced overall signal decrease or a change in relative intensity of the amides I and II bands should be observed. In contrary, a slight signal increase (*ca.* 10%) after Ca^{2+} addition is observed with no significant changes in relative band intensities. Therefore, a rather small re-orientation of the CYT domain within *Mt*CDH takes place, which is triggered by binding of Ca^{2+} to the enzyme. This hypothesis is supported by the fact, that the SERR intensity of the heme can already drastically decrease if the orientation of the heme plane becomes more parallel to the surface.[133] Such a small reorientation would be hardly visible in the SEIRA spectrum. Hence, it can be concluded that the overall orientation of the entire enzyme remains mostly unchanged and only the relative alignment of the heme plane to the surface is significantly altered.

In a previous study by Schulz et al.[168] a strong effect of Ca^{2+} ions on catalytic activity has been reported for *Mt*CDH modified graphite electrodes. In that work a five times higher catalytic current has been observed. It was proposed that the presence of Ca^{2+} either influences the heterogeneous electron transfer rate or that binding of Ca^{2+} to the enzyme decreases the distance between the FAD and the heme cofactor resulting in a higher intramolecular electron transfer.[168] In presented experiments the heterogeneous electron transfer rate remains almost unchanged suggesting that the increased catalytic current of the enzyme does not originate from enhanced electron transfer between the cytochrome domain and the electrode. A change in the distance between the heme and the FAD, however, seems likely, taking into account the proposed CYT domain re-orientation.

The most striking differences between addition of monovalent Na^{+} or divalent Ca^{2+} ions can be found when the potential dependence of the catalytic current, recorded by CV, is compared to the heme redox titration, measured with SERRs (Figure 4.2.5C). In the electrochemical turnover signal a negative potential shift of the catalytic current is observed upon addition of Ca^{2+} similar to the one measured for high ionic strength conditions. The $E^{\circ\prime}$ of the heme, however, shifts by *ca.* 30 mV to more positive values. Based on the direction of the shift and the fact that the change in the $E^{\circ\prime}$ occurs already at a very low Ca^{2+} ion concentration, it is likely that $E^{\circ\prime}$ of the heme itself has changed and not the electrostatic interaction between the protein and the electrode. This redox shift could be very likely induced by binding of Ca^{2+} to

the heme propionates that would stabilize the reduced form of the heme similar to what has been reported previously for myoglobin and Mn^{2+} ions.[181]

In the presence of Ca^{2+} the inflection point of the catalytic current is 85 mV more negative than $E^{\circ\prime}$ of the heme; thus a closed catalytic cycle is already achieved at potentials where the heme domain stays reduced, limiting its ability to accept catalytically created electrons from FAD center. Therefore, under these conditions an electron pathway from the FAD to the electrode is created that bypasses the heme redox center. This alternative electron transfer pathway is responsible for the more negative open circuit potential measured in the presence of Ca^{2+}.

This hypothesis is supported by the chronoamperometric measurements under turnover conditions (Figure 4.2.10): When the applied potential is set equal to the heme redox potential (-54.5 mV) addition of Ca^{2+} ions has no effect on the recorded current as an efficient electron transfer pathway via the heme has been already established at this potential. At an applied potential of -100 mV the catalytic current is generally lower as heme reduction by the electrode competes with catalysis. However, at this potential presence of Ca^{2+} ions improves the catalytic performance as it opens up a new pathway for the electrons from the FAD to the electrode. In principle, this increased current could also be a result of a faster intramolecular electron transfer. In this case, however, one should have observed increased currents for both potentials upon addition of calcium.

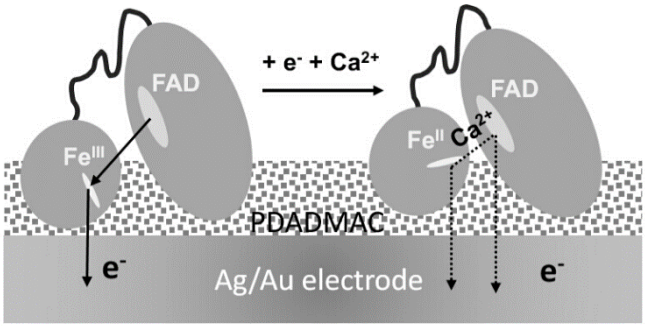

Figure 4.2.10 Schematic representation of the proposed changes in orientation and electron transfer mechanism of CDH on PDADMAC coated electrodes upon addition of Ca^{2+} ions.

Based on these observations a reaction model depicted in Figure 4.2.10. can be proposed. In the oxidized state of the heme, Coulomb-interactions stabilize the positively charged iron with negatively charged propionate groups. In the reduced state, this interaction is weakened and

the heme propionates are thought to bind the Ca^{2+} ion. The Flavin domain exhibits several negatively charged amino acids at the surface that faces the CYT domain.[182] One of these amino acids could bind to the Ca^{2+} ion, which would compensate for the positive excess charge. Note that this binding would not occur if only monovalent Na^{+} ions are present. The newly formed electrostatic bond between the two domains could alter the electron pathway from the FAD to the electrode. This might in general lead to faster internal electron transfer rate as proposed before.[168] However, the catalytic currents below -50 mV, observed in in this work, do not involve a redox transition of the heme cofactor as they occur at much more negative potentials than its $E^{\circ\prime}$ value. The negatively shifted catalytic activity in the presence of Ca^{2+} would then be attributed to the promotion of an alternative electron transfer pathway between the Flavin and the PDADMAC coated electrode triggered by the Ca^{2+} induced reorientation. In this scenario, the cytochrome domain would function as an anchor for *Mt*CDH to the electrode. Albeit the electron pathway bypasses the heme at more negative potentials the presence of the cytochrome domain nevertheless stabilizes the enzyme on the surface in a desirable orientation. Such an stabilizing effect has been observed before for the membrane bound Hydrogenase (MBH) trimer on electrodes[171] where five times higher catalytic activity was observed in the presence of the cytochrome domain that was not involved in the electron transfer pathway.

Concluding remarks

Cellobiose dehydrogenase from *Myriococcum thermophilum* was successfully immobilized on PDADMAC coated metal electrodes and showed to be catalytically active in presence of lactose as substrate. Comparison of the catalytic currents with SER spectroscopic monitoring of the heme oxidation state confirmed that the electrocatalytic electron transfer pathway from the catalytic FAD center to the electrode involves the heme as an intermediate electron acceptor. Addition of monovalent Na^+ and divalent Ca^{2+} ions lead both to a negative shift of the catalytic turnover signal. However, the mechanistic origin of this shift was found to be much different for both types of ions. Higher concentrations of monovalent Na^+ affected the electrostatic interaction between the enzyme and the coated electrode resulting in a negative shift of the heme redox potential which was still involved in the ET pathway. In contrary, complementary SERS and SEIRA measurements strongly indicate that divalent Ca^{2+} ions bind directly to the reduced heme propionate groups leading to a positive shift of the heme redox potential and a re-orientation of the heme plane in respect to the surface. To explain the observed negative shift in the catalytic turnover a scenario where a negatively charged amino acid chain of the flavin domain also binds from the other side to Ca^{2+} to compensate for the excess charge is proposed. This local reorientation establishes a new electron transfer pathway to the electrode that does not need the heme iron as intermediate electron acceptor. Electron transfer is thus not limited by the heme redox potential anymore and more negative open circuit potentials could be achieved this way. Undoubtedly, these findings are of high interest for better understanding the parameters that control the catalytic activity of CDH on electrodes and thus can give valuable suggestions for rational design of enzymatic biofuel cells.

4.3 Hydrogen evolution by cobalt hangman porphyrins under operating conditions studied by combined vibrational spectroelectrochemistry

4.3.1 Abstract

Cobalt Hangman complexes are promising catalysts for hydrogen production yet their catalytic mechanism is still a topic of dispute. In this project, the structure of hangman complexes attached to electrodes during catalytic turnover was investigated via electrochemistry and Surface enhanced resonance Raman spectroscopy. To understand the role of the hanging group for proton supply, complexes with either a carboxylic acid or ester hanging group were compared. Dip-coating immobilization procedures resulted in forming not uniformly active species on the electrode. RR and SERR spectra in great majority probed formation of Co^{I} species. For immobilized CoPCOOH measured at pH 4 and pH 10 conditions, possibly electrochemical formation of Co^{III}-H species occur, followed by photochemical dissociation of proton induced by laser illumination in SERR experiment. For immobilized CoPCOOMe measured at pH 4 conditions, photochemical homolytic cleavage of Co^{III}-H yielded evolution of dihydrogen. Obtained results suggest formation of Co^{I} and Co^{III}-H intermediates in HER cycle under operating conditions.

4.3.2 Introduction

Hydrogen-based fuel cells are one of the most promising renewable-energy devices today. However, they rely on the constant supply of molecular hydrogen, which has to be created and stored in an efficient way. Thus, as of yet, the costly production of dihydrogen is a crucial limitation for their competitiveness in industrial applications.[183] As a consequence, extensive efforts have been made to find active and long-lasting catalysts for electrochemical hydrogen evolution. Molecular, synthetic catalysts have the strong advantage that their chemical properties can be tuned in a very precise manner, thereby opening up the possibility to understand the mechanism of a desired reaction in more detail. On the downside, many of these molecular catalysts, especially when adsorbed on electrodes, require high overpotentials for effective catalysis and are unstable under turn-over conditions.[184,185] A promising class of catalysts is based on Hangman porphyrins (see Figure 4.3.1). In these compounds, the porphyrin macrocycle provides a cleft for a metal center responsible for electron transfer, while a hanging functional group plays the role of a proton relay. Together, the so designed structure is suitable to perform proton/electron transfer reactions.[30,32,186] The selectivity to a certain reaction can be tuned by the choice of the metal, and, indeed, it could be shown that cobalt and nickel Hangman porphyrins as well as corroles are good catalysts for the hydrogen evolution reaction (HER),[37,187–190] whereas iron and cobalt analogues are suitable for the oxygen reduction reaction (ORR).[34,191–193] Similarly, the effect of the functional group, which can accelerate proton supply (or removal) as a key limiting factor, was investigated for many target reactions, e.g. water oxidation.[36,194] Several reaction mechanisms have been proposed for this class of Hangman porphyrins based on electrochemical and spectroscopic data. However, little is known about their structure during catalytic turnover. Earlier reports include quantum mechanical calculations of relevant intermediates for HER[189,195] or vibrational spectroscopy studies of some complexes for ORR[35,191]. However, these studies are still incomplete and the conclusions drawn require further detailed analysis and experimental proof.

In the current study, cobalt hangman porphyrins and the HER reaction were chosen as models for the detection and assignment of reaction intermediates by using a combination of electrochemical, spectroscopic, and theoretical techniques. The knowledge obtained from these investigations provides first steps in understanding the mechanism of these class of complexes under operating conditions.

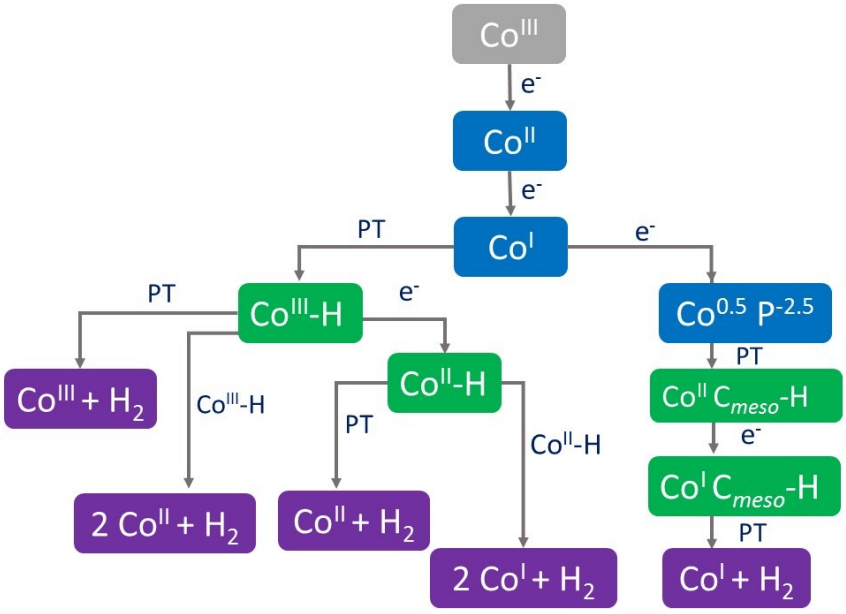

Scheme 4.3.1 Proposed mechanisms of the hydrogen evolution reaction catalyzed by cobalt hangman porphyrin.[37,189] Blue boxes represent oxidation states of cobalt changed upon reduction, green boxes represent cobalt-hydride intermediates and violet boxes represent the final states after hydrogen evolution.

The current mechanism of hydrogen evolution catalyzed by cobalt porphyrin complexes was proposed to occur via several pathways (Scheme 4.3.1).[37,189] They all begin with the reduction of Co^{II} to Co^{I} (or the two electron reduction of Co^{III} to Co^{I}, depending on the starting oxidation state). Then, as depicted by the left side of the scheme, addition of one proton can lead to the formation of a Co^{III}-H intermediate, which has also been characterized by NMR spectroscopy[196]. From this intermediate hydrogen evolves either by direct protonation of this state or by bimolecular combination with another Co^{III} hydride species. In the former case the compound converts into a Co^{III} state whereas in the latter the compound is converted back into a Co^{II} state.[32,37] Another pathway for hydrogen evolution is achieved by supply of one more electron to the Co^{III}-H intermediate leads to formation of a Co^{II}-H species from which hydrogen evolves (either by homolytic or heterolytic cleavage). In this case, the complex converts back to a Co^{II} or Co^{I} state that can re-enter the catalytic cycle. Based on theoretical calculations, it was recently proposed that under weak acidic conditions (pKa ~20 in acetonitrile) the catalytic mechanism might be different.[189] In this case the Co^{I} state is not nucleophilic enough to attack a proton and needs to be further reduced to form the so called $Co^{0.5}$ reduced state, which exhibits substantial metal-ligand orbital mixing with partial reduction of the porphyrin ligand ($P^{-2.5}$). The protonation of the reduced ($Co^{0.5}$) compound occurs via a phlorin intermediate, in which one *meso* carbon atom of the porphyrin macrocycle gets protonated. Under this condition

the aromaticity of the porphyrin is disrupted. From here, upon further reduction, followed by protonation, hydrogen evolves leaving cobalt at its Co^{I} state.[189]
Resonance Raman (RR) and surface enhanced resonance Raman (SERR) spectroscopy are chosen to gain more insight into vibrational fingerprints of cobalt hangman porphyrins under turnover conditions. Resonance Raman spectroscopy provides an excellent way to determine the oxidation, coordination and spin state changes of the porphyrin macrocycle as well as local environmental changes of neighbouring molecules.[170,197] RR investigations have been widely used in the past, especially to determine the structure of heme containing proteins or other iron porphyrin compounds, with their vibrational fingerprints now thoroughly reported.[35,60,103,171,191,198] In comparison cobalt porphyrins have been poorly investigated by vibrational spectroscopic methods so far.[198,199] Therefore, there is no clear vibrational assignment of their different oxidation states or different ligand coordination, which makes identification of reaction intermediates highly challenging. DFT calculations can help to understand the complex Raman spectra obtained in experiments. Apart from providing information about the structure of the compound, DFT methods offer a theoretical approach in which the character of uncertain bands can be precisely visualized and identified. We have thus used this approach to better interpret the obtained experimental spectra.

The catalytic efficiency of Co hangman complexes for HER has been studied mostly in organic solution.[37,186,189] In order to use them as electrocatalysts they have to be adsorbed on electrodes and should work in aqueous solution. Reaction mechanisms that have been postulated for these complexes in organic solution might be altered under these conditions. Firstly, for physisorbed complexes electron supply might become much slower. Secondly, deprotonation of the hanging group in aqueous solution, as has observed for iron hangman complexes[35] can have a strong influence on their electrocatalytic properties.

In order to study Co hangman complexes attached to electrodes in aqueous environment, applied SERR spectroscopy and electrochemistry were employed. The combination of both methods allows studying structural changes of target molecules at a defined electrode potential[60] and thus makes it possible to correlate a certain catalytic activity with an in-situ structure of the catalyst. To extract the influence of the hanging group on the structure and activity of the catalyst, two compounds having either a carboxylic acid or a methyl ester functional group were chosen. To the best of my knowledge, these are the first catalytic

correlated structural changes of immobilized cobalt porphyrins probed by vibrational spectroscopy.

4.3.3 Experimental Section

Synthesis[3]

Cobalt hangman porphyrins have been synthesized according to the described procedures.[30,34,35,200] Firstly, metal free Hangman porphyrins are formed by a statistical condensation method using 4-Formyl-5-methoxycarbonyl-2,7-di-tert-butyl-9,9-dimethylxanthene, mesitaldehyde and pyrrole followed by ester hydrolysis if necessary. Further metalation was performed by reaction of the ligands with cobalt(II) acetate in dimethylformamide. Two compounds, a cobalt Hangman porphyrin with xanthene backbone holding either a carboxylic acid or a methyl ester functionality, were afforded.

Absorbance and Resonance Raman spectroscopy

For spectroscopic measurements in solution, complexes were dissolved in acetonitrile to reach a final concentration of around 2 mM. For reduction experiments, KEt3BH was dissolved in tetrahydrofuran to reach a concentration of ca. 100 mM.[201] Subsequently, 50µl of the reducing agent was added to the complexes containing solution in a concentration ratio of 1:10, anaerobically in an oxygen free tent.

For spectroscopic measurements 2 mm thick quartz cuvettes were filled with samples and closed with air-tight septum rubbers. Absorbance spectra were collected using an Agilent spectrometer. For resonance Raman measurements, the 413 nm excitation line of a Kr^+ ion laser was used. Spectra were recorded with a confocal Raman spectrometer (LabRam-HR 800, Jobin Yvon) equipped with a Symphony detector. The laser was focused on the sample with 20x Olympus objective, laser power reached 500 µW and light was collected in 180° back scattered geometry. Spectra were accumulated 10 times for 20s and averaged, using binning factor 1 and gratings of 1200 1/mm. The cuvette with sample was rotated during the measurement to avoid photo-induced processes and/or decomposition. All measurements were performed at room temperature.

[3] Done by P. Wrzolek (HU Berlin)

Electrochemistry and Surface Enhanced Resonance Raman Spectroscopy

Silver ring electrodes were polished and electrochemically roughened by a well-established method of successive oxidative and reductive steps.[102] After electrode preparation, the compounds were physisorbed by dip-coating on an electrode by placing the electrodes in a highly concentrated (1 mM) sample solution in acetonitrile and waiting for solvent to evaporate. Alternatively, the electrodes were dip-coated in 10 times diluted CoPCOOH solution, one time, five time and ten times with speed of electrode removal of 10 mm/min. Subsequently, the electrode was mounted in a homemade three-electrode spectro-electrochemical cell with a Pt electrode serving as counter electrode and an Ag|AgCl (3M) electrode as reference electrode. All potentials mentioned in the paper refer to Ag|AgCl (3M). Measurements were performed in NaBorat buffer at pH10 and in acetate buffer at pH4.
Electrochemical measurements were performed using a Autolab potentiostat from Metrohm. During chronoamperometic measurements, the electrode was rotated with 20 Hz rotational speed to avoid mass transport limitations.
In the SERR experiments, spectra were accumulated 10 times for 20s each and averaged. The electrode was rotated with 15Hz rotational speed to avoid photo-induced processes. Spectra were further baseline corrected and their intensity was normalized to the most intense ν4 mode.

DFT calculations[4]

The Raman spectra of CoTPP molecules were computed by density functional theory (DFT). The initial structure was created manually using Gaussview and further optimized. Both geometry optimization and calculation of the spectra was done using Gaussian 09 at the BP86 level of theory.[202–205] The def2tzvp basis set was utilized for the cobalt atom, while the 6-31g* basis set was used for carbon, hydrogen, nitrogen and oxygen atoms.[206] A polarizable continuum model (PCM) was applied to include the influence of the solvent (acetonitrile).[207]
Raman activities, obtained from DFT calculations, have been further transformed into Raman intensities according to a well-known procedure.[208]

[4] Done by R. Goetz (TU Berlin)

4.3.4 Results

Resonance Raman and UV-VIS spectra

Two cobalt hangman compounds have been synthesized and investigated experimentally. The first one, abbreviated as CoPCOOH, contains a carboxylic acid function as hanging group, while the second, abbreviated as CoPCOOMe, has a methyl ester function at the same position (Figure 4.3.1).

Both cobalt hangman porphyrins show a strong Soret transition in their UV-Vis absorption spectrum that is typical for metallo-porphyrins (Figure 4.3.2 AI, BI).[34] Maximum Soret peak at 432 nm and 430 nm is similar as obtained for Co^{II}TMpyP in PBS.[199]

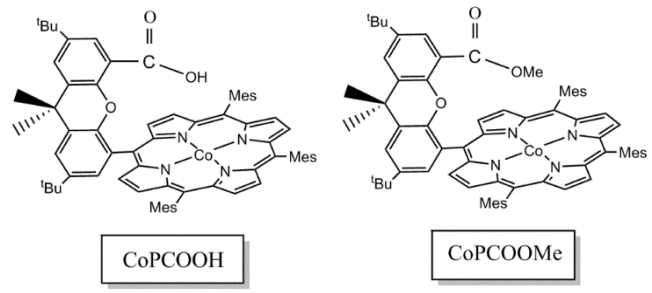

Figure 4.3.1. Chemical structures of studied hangman porphyrins with carboxylic acid or methyl ester hanging groups.

When exciting the porphyrin with a laser line close to the maximum of the Soret band transition, primarily totally symmetric porphyrin vibrations in the high frequency region of a spectrum are probed via A-term resonance enhancement. They carry the structural information about the chromophore, particularly ν_4 being the most sensitive band for oxidation state changes (composed mostly of C_α-$N_{pyrollic}$ stretches), whereas ν_3 and ν_2 are the most sensitive band to coordination and spin state changes (composed mostly of C_β–C_β and C_α-C_{meso} stretches).[45]

RR spectra obtained with 413 nm excitation of CoPCOOH and CoPCOOMe in their resting state in solution show four strong bands (Figure 4.3.2CI and 2DII) in the 1300-1700 cm^{-1} region. Based on literature reports on similar systems, all of them were assigned to porphyrin

ring vibrations.[35,198,199] Both complexes have the oxidation state sensitive mode ν_4 at 1369 cm^{-1}, which is typical for a Co^{II} state.[198,199] The coordination and spin state sensitive modes ν_3 and ν_2 were found at 1500 cm^{-1} and 1568 cm^{-1}, respectively which for hemes would imply formation of 6c low spin (6cLS) state.[68]

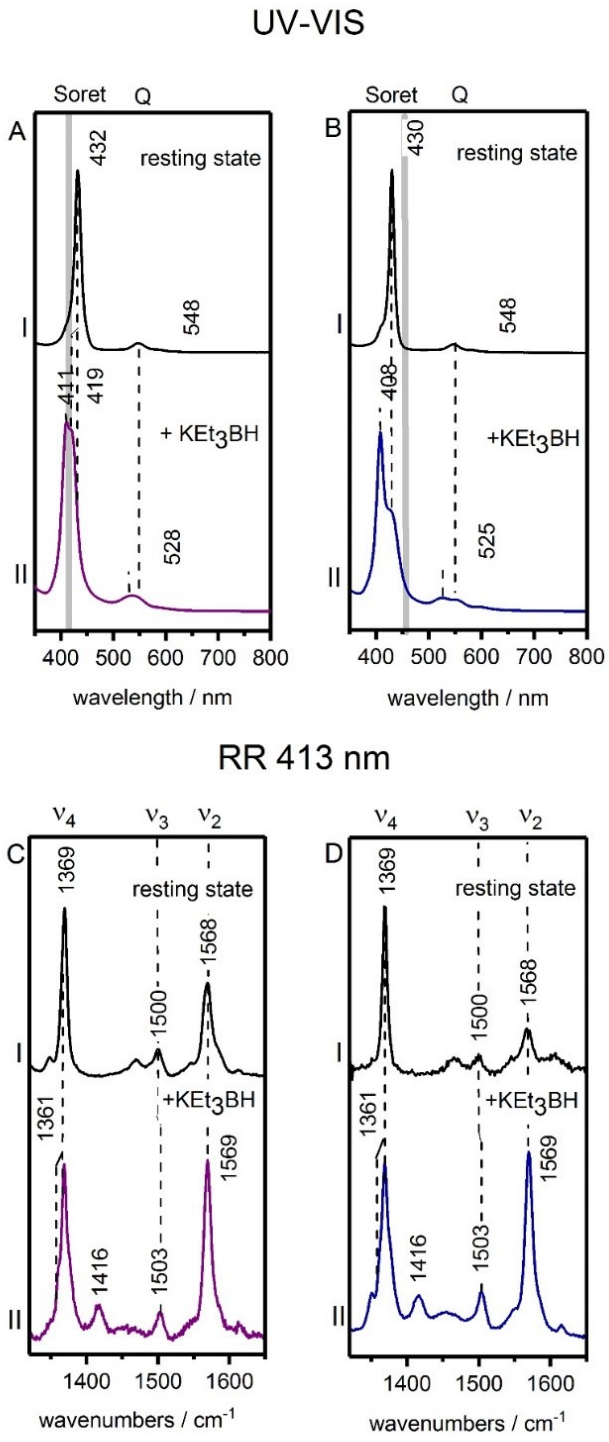

Figure 4.3.2. UV-Vis (top) and resonance Raman (bottom) spectra obtained in acetonitrile for CoPCOOH (A,C) and CoPCOOMe (B,D), using 413 nm excitation, in their resting state (I) and after addition of reductant KEt_3BH (II). Dotted lines indicate maxima in the UV-Vis spectra and the positions of porphyrin vibrations in the RR spectra, respectively. The grey line (A,B) represents the position of the 413 nm excitation laser line.

To determine the structure of Co hangman complexes in their reduced state, which is the first step during HER catalysis, KEt_3BH as a reductant was added to the resting state of both compounds. As a result, the Soret electronic transition of CoPCOOH downshifted to two maxima at 411 nm and 419 nm with slight contribution of 432 nm band, whereas the Soret electronic transition of CoPCOOMe represents rest of 430 nm band and additional maximum at 408 nm. Recorded RR spectra under so-derived conditions for both complexes show the same spectral changes in comparison to their respective resting state spectra (Figure 4.3.2CII and 4.3.2DII). The position of ν_3 and ν_2 bands upshifts by 3 cm^{-1} and 1 cm^{-1}, respectively. The ν_4 band becomes broader with a shoulder arising from a new band at 1361 cm^{-1}. Such a downshift of this band is expected for lower oxidation states.[68,170] Presence of the 1369 cm^{-1} peak indicates that significant amount of Co^{II} state is probed under so-reducing conditions. Interestingly, the final spectra revealed the appearance of a new band at 1416 cm^{-1}, which cannot be undoubtedly assigned as one of totally symmetric A_{1g} porphyrin modes for ideal D_{4h} planarity of porphyrin. Moreover, the intensity of the ν_2 band became higher than the corresponding ν_4 band, which is not common for resonance Raman spectra of porphyrins and could be a result of lowered symmetry of porphyrin macrocycle.[209]

Surface enhanced resonance Raman spectra under catalytic conditions

In order to investigate catalytic mechanism of the porphyrin compounds in aqueous environment under operating hydrogen evolving conditions, CoPCOOMe and CoPCOOH were physisorbed on roughened silver electrodes via physisorption. The method leads to formation not uniformly distributed thick layers of compounds. (for further details about composition of complexes on the electrode surface see Appendix). To correlate catalytic activity of the complexes with the available proton concentration cyclic voltammetry measurements with 2 mV/s scan rate at pH 4 in acetate buffer and pH 10 in sodium borate buffer were performed (Figure 4.3.3). Noble metals like silver have a high intrinsic catalytic activity. Thus, the turnover current of the Co hangmans superimposes with the activity of the silver electrode itself, which makes it difficult to quantify the contribution of the complexes to the HER. As seen in the CV's the catalytic activity of compounds is lower than of the electrode itself which suggests that compounds are passivating the electrode surface. In order to clarify the activity of compounds, the dip-coating method was used to control the amount of complexes on the electrode surface. Three electrodes were dip-coated in CoPCOOH diluted solution: one, five and ten times, respectively. The catalytic activity of this compound at pH 10 conditions was

highest for electrode dip-coated five times- (I ~ 3.5 mA at -1.5 V), then lower for one time- (I ~ 2.4 mA) and the lowest for ten times-dip-coated electrode (I ~ 0.9 mA) (Fig. 6.3.1, Appendix). These results show that activity of complexes is increasing with number of layers or amount of compound on the electrode until the thickness that does not further increase catalytic rate but passivates activity of former layers. Thus, the catalytic activity of physisorbed CoPCOOH and CoPCOOMe, which are expected to form thick layers (see SI), at pH 4 was found to be comparable to each other (I ~ 5 mA for CoPCOOMe and I ~ 6 mA at 1.5 V) and lower than of bare electrode (I ~ 11 mA at -1.5 V). Similarly, at pH 10, the CoPCOOMe reached the catalytic current of I ~ 0.6 mA and CoPCOOH the catalytic current of I ~ 0.8 mA, which is lower than for bare electrode (I ~ 5 mA).

For spectroscopic investigations of structural changes of the catalysts, the same electrochemical setup was used subsequently in SERR experiments. Firstly, after attaching compounds to the electrode, the structure remains unchanged with preserved frequency of the redox sensitive ν_4 mode and spin state sensitive ν_3 mode as observed in RR spectra for Co^{II} oxidation state with slight changes of their intensity ratio (Fig. 4.3.3 C, F open circuit). Secondly, the potential was applied in stepwise manner to allow collecting the potential-trapped SERR spectra. With the purpose of observing catalytically relevant intermediates of the porphyrin compounds, spectra were recorded in the potential range of 0 to -1.5 V.

In Figure 4.3.3C and 4.3.3F selected spectra are shown that correspond to the following significant changes in the CV. At -1.0 V where the catalytic turnover at pH 4 conditions is already observed, and at -1.5 V where high catalytic turnover and low catalytic turnover, at pH 4 and pH 10, respectively is demonstrated. At -1.0 V for both compounds, regardless of pH conditions, the intensity of ν_4 porphyrin mode is decreased in comparison to other porphyrin modes present in SERR spectra (Fig. 4.3.3B, 4.3.3E). Changed ratio of ν_4/ν_2 modes is potential-induced and starts at already relatively positive potential of -0.6 V and remains not further influenced by applying more negative potentials. At -1.5 V the appearance of a new peak at 1414 cm^{-1} for CoPCOOMe at pH 10 and at 1418 cm^{-1} for CoPCOOH at pH 4 and pH 10 is observed, which cannot be assigned to a totally symmetric porphyrin vibration from A_{1g} irreducible representation of D_{4h} point group. Clear potential dependent intensity of this band is presented in Figure 3B and 3E. Interestingly, the new band is not observed for CoPCOOMe at pH 4. Concomitant to the emergence of the new porphyrin band, a shoulder appeared at 1361 cm^{-1} in the ν_4 peak region of CoPCOOH. The same shoulder at 1361 cm^{-1} appears in the RR

spectra upon addition of KEt_3BH reductant in acetonitrile solution. Applying negative potentials (E<-0.8 V at pH 4 and E<-1.1 V at pH 10) results in irreversible decrease of intensity of spectrum for both compounds suggesting desorption of compounds from the electrode surface (Figure 6.3.2 and 6.3.3, Appendix).

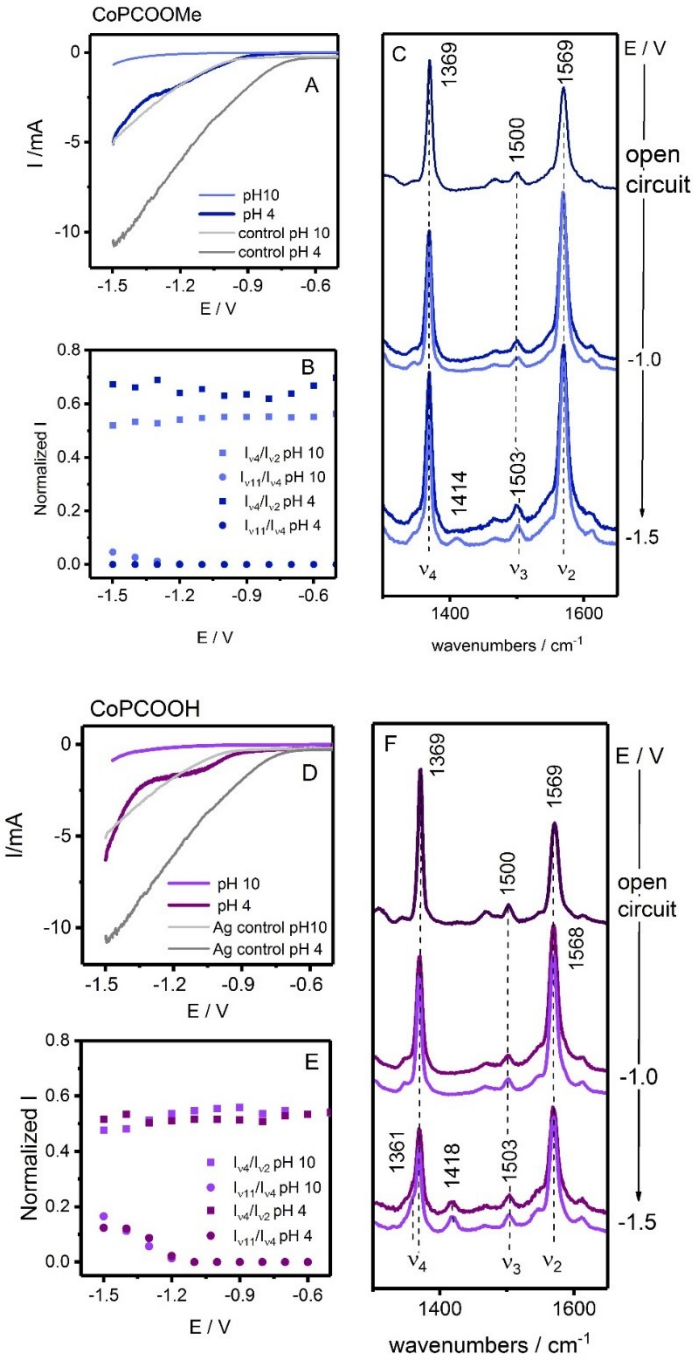

Figure 4.3.3. Catalytic responses and SERR spectra of CoPCOOMe (top) and CoPCOOH (bottom) immobilized on a roughened silver electrode at pH 4 and pH 10. (A, D) Cyclic voltammograms of compounds and control silver electrode, measured with 2 mV/s scan rate. Blue and violet lines correspond to the signal when CoPCOOMe, and CoPCOOH are attached, gray lines correspond to the response of the bare roughened silver electrode. (B, E) Potential dependent normalized intensity ratio

of ν_4/ν_2 and ν_{11}/ν_4 porphyrin vibrations detected in SERR spectra. (C, F) SERR spectra of compounds measured at open circuit, -1.2 V and -1.5 V, at corresponding pH conditions (navy blue and navy violet pH 4, light blue and light violet pH 10). Assigned porphyrin vibrations are indicated by dotted lines. SERR spectra at pH 10 -1.0 V were multiplied by 0.44. SERR spectra at pH 4 -1.5 V were multiplied by 2.68.

4.3.5 Discussion

Structures of CoPCOOH and CoPCOOMe in the resting state

The resonance Raman spectra of the carboxylic acid as well as the methyl ester complex in their resting states (Figure 4.3.2) revealed three major bands (ν_4, ν_3, ν_2), which were assigned, based on previous reports, to totally symmetric marker porphyrin vibrations of a Co^{II} low spin state with two axially coordinating strong ligands, very likely acetonitrile molecules. These spectra are in good agreement with reported resonance Raman measurements on CoTMPyP complexes (TMPyP = Tetrakis(4-methylpyridyl)porphyrin).[198,199] If the investigated compounds are physisorbed on a silver electrode and no potential is applied (open circuit), the measured spectra possess the same features as compared to the solution spectra showing that immobilization did not interfere with their structure. Moreover, comparison of UV-Vis absorption spectra with reported data in the literature confirm that the oxidized Co^{II} state is present in the measurements.[34,198,199]

Structures of CoPCOOH and CoPCOOMe under reducing and HER operating conditions

The addition of KEt_3BH reductant to compounds dissolved in acetonitrile results in formation of different species for CoPCOOH and CoPCOOMe, which is indicated by UV-Vis spectra. It can be assumed that the bands at 411 nm (CoPCOOH) and at 408 nm (CoPCOOMe) correspond to one species, and the band with maximum at 419 nm (CoPCOOH) correspond to another species not formed in CoPCOOMe compound. Interestingly, the RR spectra of both compounds in reducing conditions are merely identical with characteristic new changes: decreased in intensity and broadened ν_4 porphyrin mode with shoulder at 1361 cm^{-1}, upshift of ν_3 and ν_2 modes and appearance of new mode of 1416 cm^{-1} frequency and significant rest contribution of features belonging to Co^{II} state. Based on catalytic mechanism of compounds presented in Scheme 4.3.1, in the absence of proton donor, the reduction of Co^{II} state leads to the formation of either Co^{I} or $Co^{0.5}P^{-2.5}$ species. The occurence of the latter, which in literature is described as phlorin intermediate[188] or porphyrin anion radical[210] would require highly

reducing agent, and its presence would be reflected in UV-Vis spectrum by broad band below 700 nm[188]. Since none of these aspects are fulfilled in the measurements, the RR species cab be assigned to Co^{I} state. It is interesting to note distinct RR spectral features of this species, out of which some are found to be typical for RR of metalloporphyrins, such as downshift of ν_4 band with concomitant upshift of ν_3 and ν_2 mode, and other unusual components such as decrease of ν_4 intensity and appearance of new mode which might be assigned to ν_{11} porphyrin mode[210,211] (see discussion in Appendix). The former aspects could be understood as a result of reduced core size of cobalt porphyrin upon reduction to Co^{I} state observed for totally symmetric A-term enhanced modes.[68] The latter ones require consideration of either lowering of porphyrin symmetry upon which other than described in former case porphyrin modes are becoming totally symmetric and thus enhanced (A-term enhancement), or of other mechanisms involving mixing of vibrational basis set (B-term or C-term vibronic coupling enhancement), which might give rise to complete Raman excitation profile (REP) of porphyrin modes.[16,67,209,212,213] The indications of both: ruffling of the porphyrin plane and composition and assignment of mode at *ca*. 1414 cm^{-1} to non-totally symmetric mode derived from the B_{1g} representation are further discussed in Appendix, supported by quantum mechanical calculations of Co^{I}TPP (cobalt tetraphenylporphyrin).

The same spectral features are observed in SERR spectra of COPCOOH at both pH 4 and pH 10 conditions and for CoPCOOMe at pH 10 conditions, at applied -1.5 V potential. Similarity of the vibrational signature of all these spectra allows to conclude that in all cases the same Co^{I} intermediate is probed.

Implications of probed species on HER catalytic mechanism

Although RR spectra reveal probing of the same Co^{I} intermediate, different mechanisms drive its formation. The simplest case is found for CoPCOOMe compound dissolved in acetonitrile solution, in which addition of reductant results in reducing Co^{II} to Co^{I} state, supported by shift of Soret electronic transition from 430 nm to 408 nm. The reduction, however, is not complete which is reflected by remaining presence of shoulder in Soret region of UV-Vis spectra and corresponding modes in RR spectrum. The similar situation is created for CoPCOOMe attached to the electrode at pH 10 conditions, in which thick layers of compound can be treated as proton donor absent conditions.

In the proton donor present conditions, as for CoPCOOH dissolved in acetonitrile, the reduction to Co^{I} species (411 nm peak in UV-Vis spectrum) is further followed by proton transfer from hanging group and most likely formation of Co^{III}-H intermediate species, which is visible in UV-Vis spectrum as band with maximum at 419 nm. This species, however is failed to be probed by RR spectroscopy due to perturbation of laser illumination. It is known that metal hydrides can undergo photochemical dissociation of proton or hydride.[214] One example of such photolysis probed by RR spectroscopy is photoconvertion of bridging hydride in [NiFe] hydrogenase followed by proton transfer to neighbouring cysteine.[215] In Co^{III}-H state, photoillumination most likely results in dissociation of proton which subsequently is transferred back to carboxylic hanging group leaving compound at Co^{I} state (Scheme 2). Thus, although this state is present in solution, RR spectrum reflects the composition of Co^{I} state with some amount of Co^{II} state. Definite amount of substates present in spectra is difficult to quantify since resonance Raman cross sections for certain states cannot be simply taken from UV-Vis spectra as different mechanisms have to be taken into account to construct REP profiles of the species. Similar case, in which proton from Co^{III}-H intermediate is photoconverted back into carboxylic hanging group yielding photo-formation of Co^{I} state is expected to occur for CoPCOOH immobilized on the electrode at both pH 4 and pH 10 conditions (Scheme 4.3.2). Note that compounds form thick layers on the electrode in which catalytic activity is passivated. Most likely, the species closest to the electrode are trapped by amount of sample on the electrode, and thus after formation of Co^{III}-H species, proton transfer is too slow for further hydrogen evolution. Alternatively, the electron transfer could take place to yield formation of Co^{II}-H species from which hydrogen could be evolved, however photoreaction of this intermediate would not result in formation of Co^{I} state. In any case, the photodissociation occurs to be faster than any possible catalytic electron or proton transfer, thus further probing of mechanistic cycle is interrupted. Situation is different in thinner layers of compounds (dip-coating), which RR spectra at applied negative potential did not result in observing Co^{I} species (Fig 6.3.2, Appendix). As follows, constant turnover of catalytic species makes them not detectable in RR spectra.

Second case of photolytic cleavage of hydride species is present for CoPCOOMe physisorbed on the electrode at pH 10 conditions. Here, the proton transfer yields formation of Co^{III}-H species. Subsequent laser illumination most probably homolytically cleaves hydrogen from

two neighbouring species (compounds lack proton accepting hanging group). As a result, Co^{II} state iformed and hence give enhancement in RR spectrum (Fig. 4.3.3C and Scheme 4.3.2).

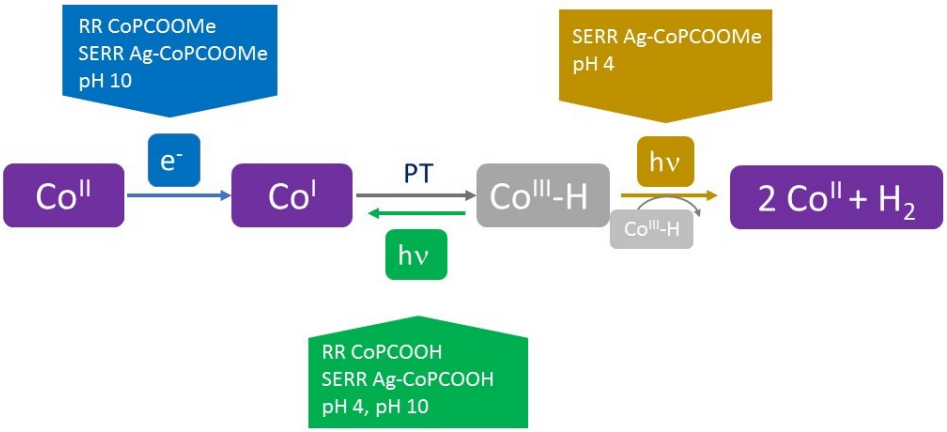

Scheme 4.3.2. Proposed mechanistic cycle of CoPCOOH and CoPCOOMe physisorbed on an electrode under operating HER conditions perturbated by laser-illumination. Intermediates marked in violet represent visible states in RR and SERR spectra under conditions described in boxes.

Obtained results confirm that catalytic mechanism of hydrogen evolution occurs via formation of Co^{III}-H species for CoPCOOH and alternatively can follow homolytic cleavage of hydrogen atoms for CoPCOOMe. However, complete assignment of species under HER operating conditions is failed due to perturbation of photochemical reactions and difficulty of forming uniformly active compound on the electrode surface.

Concluding remarks

The structures of Co hangman complexes with a carboxylic acid or methyl ester hanging motif were investigated during HER catalysis by potential dependent SERR experiments. Upon reducing the compounds dissolved in solution and at applied negative potentials (-1.5 V) formation of Co^{I} species in RR and SERR spectra was observed. The rate of the catalytic activity of compounds attached to the electrodes was not possible to obtain due to high current background originating from silver activity and not uniform formation of active species upon immobilization. Formation of Co^{III}-H intermediate was detected in UV-Vis spectrum of CoPCOOH in solution and further comparisons allowed to conclude formation of this species at immobilized state at pH 4 and pH 10 conditions. However, due to photochemical dissociation of proton from this state of CoPCOOH, SERR spectroscopy failed to probe further HER intermediates. In contrast, CoPCOOMe yielded photo-induced formation of dihydrogen by homolytic cleavage of hydrogen atoms.

V. CONCLUSIONS AND OUTLOOK

RR, electrochemistry and SERR vibrational spectroscopy was employed to elucidate structure-function relationship of the heme proteins HTHP and *Mt*CDH and synthetic hangman cobalt porphyrin compounds. In all cases, investigations focused on detecting the redox transitions of the heme or porhyrin active sites and identifiying correlations with the structural parameters. In some cases, the electrocatalytic activity of immobilized species and their structural behaviour on the electrode was monitored. RR/SERR spectroscopic analysis of the porphyrin groups was achieved by excitation in the Soret transition which led to the resonance enhancement. For immobilization, roughened silver electrode served as a supporting material, which functioned as the working electrode in the electrochemical experiment and provided satisfactory Raman signal enhancement at the respective excitation wavelength in the SERR experiment.

In the first part of work, spectroscopic and electrochemical investigations of immobilized HTHP identified different heme redox species in the protein. The structure of all hemes in solution was found to be five coordinated with tyrosine as an axial ligand. All hemes possessed the same redox potential of -0.54 V (vs. Ag|AgCl), as shown in Uv-vis spectroelectrochemical experiment. Electrostatic and covalent binding of the protein to the MUA-coated silver electrode resulted in different redox species. CVs revealed redox transitions at *ca*. -0.17 V which partially were as well observed by SERRs. Additionally, SERRs studies revealed low potential transitions at *ca*. -0.49 V and -0.43 V, accounting for the native redox transition as in solution and slightly modified one. The reason for observing not uniform heme redox properties is the different orientation and thus different interaction of hemes the surface. As shown by coarse grained molecular dynamics simulation, the protein can possibly adsorb in a disc-like conformation (in which all hemes possess the same distance to the electrode) or a wheel-like conformation (in which hemes have different distances to the electrode). Possibly, the hemes being farthest away from the electrode surface retain their native properties and thus exhibit high potential transition in SERR, but fail to be detected in CV. The hemes from the wheel-like conformation, which exhibit shortest distance to the electrode and are the most probable to be influenced by the local electric field at MUA/electrode interface, display highest redox transition accounting for a perturbated heme structure, however just poorly detectable in SERR of electrostatically bound HTHP. Finally, the slightly modified redox transition at *ca.* -0.43 V of the heme was found to account for structurally changed heme, in which possibly

tyrosine weakened coordination could be a reasonable cause. Presented findings could have further implications on function of HTHP. It was previously proposed and electrochemically proven that the protein can exhibit peroxidase and catalase activity. However, this activity refers to high redox transition hemes which are likely perturbated. The structural similarity and distinct tyrosine coordination can be found in heme proteins involved in heme trafficking systems. In these proteins, similarly like in HTHP, tyrosine carries a negative charge which can be enhanced by hydrogen bonding interaction with neighbouring amino acid. Moreover, in these proteins it is believed that tyrosine ligation is responsible for heme uptake. As observed in our experiments weakened tyrosine ligation and partial release of the heme from the protein point to a similar role for HTHP. The possibility of the protein to serve as a heme carrier opens new considerations about mechanism of this process whether it is potential-, membrane-interaction or protein-interaction controlled. In this context, further studies to investigate the release and the uptake of heme in HTHP are required.

In the second part of the work, spectro-electrochemical studies on *Mt*CDH contributed to the understanding of the influence of ionic strength conditions and divalent cations on the heterogenous electron transfer rate and the catalytic efficiency of an enzyme immobilized on the polymer PDADMAC-coated silver electrode. Electrochemical and spectroscopic methods have proven that increased ionic strength conditions can lead to an increased DET rate from the cytochrome domain to the electrode, and a downshift of the onset potential for lactose oxidation. Divalent cations caused reorientation of the electrostatically bound cytochrome domain, shift of the onset potential for the catalytic activity of the enzyme and opened new electron transfer pathway directly from the FAD center to the electrode, which overall increased the ET efficiency. It is highly probable that, calcium-induced conformational reorganization leads to increased ET rate between FAD and the electrode as a result of enhanced probability of transient donor-acceptor state formation. These findings inspired further investigations of DET from the flavin to the electrode by Schulz et al., who showed as well DET from FAD to the electrode of *Tv*CDH and *Ps*CDh from I class of CDH entrapped under a dialysis membrane fixed onto a SAM-coated gold electrode at low pH, in the absence of cations.[216] Due to rare the poor HET between the flavin domain and the electrode these findings are of high interest of further understanding this ET process. Moreover, since the new electronic pathway occurs at more negative potential, the CDH gains an additional argument for the use in biodevices in which oxidation of other compounds could be potential-discriminated.

In the third part of work, spectro-electrochemical investigations were chosen to analyze structure of catalytic intermediates of cobalt hangman porphyrins during hydrogen evolution reaction. These were first vibrational spectroscopic studies of this cobalt compounds. RR spectra revealed characteristic modes for porphyrin vibrations with spectrum very similar to widely known hemes or iron porphyrins. When the compounds were immobilized on an electrode, they exhibit electrocatalytic hydrogen evolution at potentials of *ca*. -1.2 V (vs. Ag|AgCl in aqueous solution at pH 4 and pH 10). Compounds with an acid hanging group were active at both pH 4 and pH 10 conditions, whereas ester functions were found to be inactive at pH 10 conditions. At operating catalytic potentials when compounds were physisorbed on the electrode, SERR spectra revealed a distinct additional ν_{11} porphyrin mode of B_{1g}-derived symmetry group. The appearance of this mode was the result of distortion of the porphyrin ring which resulted in lowered macrocycle symmetry, and thus became visible in resonance Raman experiment under Soret excitation. The deformations were further proven in theoretical DFT calculations. The appearance of new peak correlated well with onset potential of HER catalysis. It was assumed that a catalytic intermediate Co^{III}-H was formed under operating conditions when compounds are physisorbed on the electrode. However, due to perturbations originating from laser illumination and subsequent photochemical reactions, further probing of catalytic cycle was not feasible. Photodissociation of proton and hydrogen atom in CoPCOOH and CoPCOOMe, respectively were found to be the most satisfactory explanation for result of this photoinduced reaction. Moreover, these findings showed the interesting aspect of distorted porphyrin compound in catalysis. Such effects of hangman ligands were not addressed before in the context of catalysis, therefore it might be interesting for further investigations.

The present work demonstrated the importance of in-situ structural investigations of porphyrin containing compounds and proteins for the understanding their catalytic performance and function, both in biology and synthetic chemistry. Combination of electrochemistry and vibrational spectroscopy provided a thorough way in elucidating the redox-related structural response in electrocatalysis.

REFERENCES

1. Beale, S. I. Biosynthesis of Hemes. *Knowl. Creat. Diffus. Util.* **3,** 2406–8 (2005).

2. *Porphyrins and Metalloporphyrins*. (Elsevier Scientific, 1975).

3. Barkigia, K. M., Chantranupong, L., Smith, K. M. & Fajer, J. Structural and theoretical models of photosynthetic chromophores. Implications for redox, light-absorption properties and vectorial electron flow. *J. Am. Chem. Soc.* **110,** 7566–7567 (1988).

4. Poulos, T. L. Heme enzyme structure and function. *Chem. Rev.* **114,** 3919–3962 (2014).

5. Mense, S. M. & Zhang, L. Heme: a versatile signaling molecule controlling the activities of diverse regulators ranging from transcription factors to MAP kinases. *Cell Res.* **16,** 681–92 (2006).

6. Auwärter, W., Écija, D., Klappenberger, F. & Barth, J. V. Porphyrins at interfaces. *Nat. Chem.* **7,** 105–20 (2014).

7. Biesaga, M., Pyrzy??ska, K. & Trojanowicz, M. Porphyrins in analytical chemistry. A review. *Talanta* **51,** 209–224 (2000).

8. Smulevich, G., Feis, A. & Howes, B. D. Fifteen years of Raman spectroscopy of engineered heme containing peroxidases: what have we learned? *Acc. Chem. Res.* **38,** 433–40 (2005).

9. Rydberg, P., Sigfridsson, E. & Ryde, U. On the role of the axial ligand in heme proteins: A theoretical study. *J. Biol. Inorg. Chem.* **9,** 203–223 (2004).

10. Tezcan, F. A., Winkler, J. R. & Gray, H. B. Effects of ligation and folding on reduction potentials of heme proteins. *J. Am. Chem. Soc.* **120,** 13383–13388 (1998).

11. Liu, J. *et al.* Metalloproteins containing cytochrome, iron-sulfur, or copper redox centers. *Chem. Rev.* **114,** 4366–4369 (2014).

12. Cameron, M. D. & Aust, S. D. Cellobiose dehydrogenase–an extracellular fungal flavocytochrome. *Enzyme Microb. Technol.* **28,** 129–138 (2001).

13. Hildebrandt, P. & Stockburger, M. Cytochrome c at charged interfaces. 1. Conformational and redox equilibria at the electrode/electrolyte interface probed by surface-enhanced resonance Raman spectroscopy. *Biochemistry* **28,** 6710–6721 (1989).

14. Voigt, P. & Knapp, E. W. Tuning Heme Redox Potentials in the Cytochrome c Subunit of Photosynthetic Reaction Centers. *J. Biol. Chem.* **278,** 51993–52001 (2003).

15. Hu, X., Brunschwig, B. S. & Peters, J. C. Electrocatalytic hydrogen evolution at low overpotentials by cobalt macrocyclic glyoxime and tetraimine complexes. *J. Am. Chem. Soc.* **129,** 8988–8998 (2007).

16. L. D. Sparks, C. J. Medforth, M. S. Park, J. R. Chamberlain, M. R. Ondrias, M. O. Senge, K. M. Smith, J. A. S. Metal Dependence of the Nonplanar Distortion of Octaalkyltetraphenylporphyrins. *J. Am. Chem. Soc.* **115,** 581–592 (1993).

17. Varadarajan, R., Zewert, T. E., Gray, H. B. & Boxer, S. G. Effects of buried ionizable amino acids on the reduction potential of recombinant myoglobin. *Science* **243,** 69–72 (1989).

18. Olea, C., Kuriyan, J. & Marletta, M. A. Modulating heme redox potential through protein-induced porphyrin distortion. *J. Am. Chem. Soc.* **132,** 12794–12795 (2010).

19. Coon, M. J. CYTOCHROME P450: Nature's Most Versatile Biological Catalyst. *Annu. Rev. Pharmacol. Toxicol.* **45,** 1–25 (2005).

20. McDonnell, A. M. & Dang, C. H. Basic review of the Cytochrome P450 System. *J. Adv. Pract. Oncol.* 263–268 (2013).

21. Zámocký, M. *et al.* Independent evolution of four heme peroxidase superfamilies. *Arch. Biochem. Biophys.* **574,** 108–119 (2015).

22. Yoshikawa, S., Muramoto, K. & Shinzawa-Itoh, K. Proton-pumping mechanism of cytochrome C oxidase. *Annu. Rev. Biophys.* **40,** 205–23 (2011).

23. Michel, H., Behr, J., Harrenga, a & Kannt, a. Cytochrome c oxidase: structure and spectroscopy. *Annu. Rev. Biophys. Biomol. Struct.* **27,** 329–56 (1998).

24. Brzezinski, P., Ojemyr, L. N. & Adelroth, P. Intermediates generated during the reaction of reduced Rhodobacter sphaeroides cytochrome c oxidase with dioxygen. *Biochim. Biophys. Acta* **1827,** 843–7 (2013).

25. Zhang, W. & Li, G. Third-generation biosensors based on the direct electron transfer of proteins. *Anal. Sci.* **20,** 603–609 (2004).

26. Meredith, M. T. & Minteer, S. D. Biofuel cells: enhanced enzymatic bioelectrocatalysis. *Annu. Rev. Anal. Chem. (Palo Alto. Calif).* **5,** 157–179 (2012).

27. Leech, D., Kavanagh, P. & Schuhmann, W. Enzymatic fuel cells: Recent progress. *Electrochim. Acta* **84,** 223–234 (2012).

28. Bullen, R. A., Arnot, T. C., Lakeman, J. B. & Walsh, F. C. Biofuel cells and their development. *Biosens. Bioelectron.* **21,** 2015–2045 (2006).

29. Stoica, L., Ludwig, R., Haltrich, D. & Gorton, L. Third-generation biosensor for lactose based on newly discovered cellobiose dehydrogenase. *Anal. Chem.* **78,** 393–398 (2006).

30. Dogutan, D. K., Kwabena Bediako, D., Teets, T. S., Schwalbe, M. & Nocera, D. G. Efficient synthesis of hangman porphyrins. *Org. Lett.* **12,** 1036–1039 (2010).

31. Lee, C. H., Villágran, D., Cook, T. R., Peters, J. C. & Nocera, D. G. Pacman and hangman metal tetraazamacrocycles. *ChemSusChem* **6,** 1541–4 (2013).

32. Roubelakis, M. M., Bediako, D. K., Dogutan, D. K. & Nocera, D. G. Proton-coupled electron transfer kinetics for the hydrogen evolution reaction of hangman porphyrins. *Energy Environ. Sci.* **5,** 7737–7740 (2012).

33. Bediako, D. K. *et al.* Role of pendant proton relays and proton-coupled electron transfer on the hydrogen evolution reaction by nickel hangman porphyrins. *Proc. Natl. Acad. Sci. U. S. A.* **111,** 15001–15006 (2014).

34. McGuire Jr., R. *et al.* Oxygen reduction reactivity of cobalt(ii) hangman porphyrins. *Chem. Sci.* **1,** 411 (2010).

35. Ly, H. K. *et al.* 2 Nd Coordination Sphere Controlled Electron Transfer of Iron Hangman Complexes on Electrodes Probed By Surface Enhanced Vibrational Spectroscopy. *Chem. Sci.* **6,** 6999–7007 (2015).

36. Dogutan, D. K., McGuire, R. & Nocera, D. G. Electocatalytic water oxidation by cobalt(III) hangman β-octafluoro corroles. *J. Am. Chem. Soc.* **133,** 9178–80 (2011).

37. McKone, J. R., Marinescu, S. C., Brunschwig, B. S., Winkler, J. R. & Gray, H. B. Earth-abundant hydrogen evolution electrocatalysts. *Chem. Sci.* **5,** 865–878 (2014).

38. Dyads, P. *et al.* Electrochemistry and Spectroelectrochemistry of Bismanganese. 3479–3489 (2011).

39. Peljo, P. *et al.* Biomimetic oxygen reduction by cofacial porphyrins at a liquid-liquid interface. *J. Am. Chem. Soc.* **134,** 5974–84 (2012).

40. Costas, M. Selective C–H oxidation catalyzed by metalloporphyrins. *Coord. Chem. Rev.* **255,** 2912–2932 (2011).

41. Peg, W. J. Electronic Spectra. *Society* 1894–1900 (1985).

42. Hof, M. Section II Methods 1 : Optical Spectroscopy Basics of Optical Spectroscopy. **1,** 1–3 (2003).

43. David Dolphin. *The Porphyrins*. (1978).

44. Gouterman, M. Spectra of Porphyrins. *J. Mol. Spectrosc.* **6,** 138–163 (1961).

45. Siebert, F. & Hildebrandt, P. *Vibrational spectroscopy in life science*. **286,** (WILEY-VCH Verlag, 2008).

46. Herzberg, G. *Molecular spectra and molecular structure II. Infrared and Raman spectra of polyatomic molecules*. (1945).

47. Wilson, P. C. *et al.* MOLECULAR VIBRATIONS: The Theory of Infrared and Raman Vibrational Spectra. *J. Electrochem. Soc.* **102,** 1–394 (1955).

48. Long, D. a. *Early history of the Raman effect*. *International Reviews in Physical Chemistry* **7,** (1988).

49. Raman, C. V. & Krishnan, K. S. A New Type of Secondary Radiation. *Nature* (1928).

50. Placzek, G. *The Rayleigh and Raman scattering*. (Lawrence Radiation Laboratory, 1959).

51. Albrecht, A. C. On the theory of Raman intensities. *J. Chem. Phys.* **34,** 1476–1484 (1961).

52. Etchegoin, P. G. & Le Ru, E. C. A perspective on single molecule SERS: current status and future challenges. *Phys.*

Chem. Chem. Phys. **40,** (2008).

53. Aroca, R. in *Surface-Enhanced Vibrational Spectroscopy* 185–222 (2006).

54. Moskovits, M. Surface-enhanced spectroscopy. *Rev. Mod. Phys.* **57,** 783–826 (1985).

55. Campion, A. & Kambhampati, P. Surface-enhanced raman scattering. *Chem. Soc. Rev.* **27,** 241–250 (1998).

56. Master, V. & Dimitra, M. S. Anisotropic plasmonic nanoparticle arrays for surface-enhanced biosensors. (2017).

57. Miyazawa, T. & Blout, E. R. The Infrared Spectra of Polypeptides in Various Conformations: Amide I and II Bands. *J. Am. Chem. Soc.* **83,** 712–719 (1961).

58. Byler, D. M. & Susi, H. Examination of the secondary structure of proteins by deconvolved FTIR spectra. *Biopolymers* **25,** 469–87 (1986).

59. Kozuch, J. A. Structure-Function Relationships of Membrane Proteins - Spectroelectrochemical Investigation of Artificial Membranes vorgelegt von Diplom-Chemiker Jacek Artur Kozuch. 127 (2012). doi:http://dx.doi.org/10.14279/depositonce-3486

60. Kielb, P. *et al.* Spectroscopic Observation of Calcium-Induced Reorientation of Cellobiose Dehydrogenase Immobilized on Electrodes and its Effect on Electrocatalytic Activity. *ChemPhysChem* **16,** 1960–1968 (2015).

61. Heidary, N. *et al.* Orientation-controlled electrocatalytic efficiency of an adsorbed oxygen-tolerant hydrogenase. *PLoS One* **10,** 1–9 (2015).

62. Kozuch, J., Steinem, C., Hildebrandt, P. & Millo, D. Combined electrochemistry and surface-enhanced infrared absorption spectroscopy of gramicidin A incorporated into tethered bilayer lipid membranes. *Angew. Chemie - Int. Ed.* **51,** 8114–8117 (2012).

63. Ataka, K. & Heberle, J. Use of surface enhanced infrared absorption spectroscopy (SEIRA) to probe the functionality of a protein monolayer. *Biopolymers* **82,** 415–9 (2006).

64. Ataka, K. & Heberle, J. Biochemical applications of surface-enhanced infrared absorption spectroscopy. *Anal. Bioanal. Chem.* **388,** 47–54 (2007).

65. Spiro, T. G. & Strekas, T. C. Resonance Raman spectra of heme proteins. Effects of oxidation and spin state. *J. Am. Chem. Soc.* **96,** 338–345 (1974).

66. Huang, Q., Medforth, C. J. & Schweitzer-Stenner, R. Nonplanar heme deformations and excited state displacements in nickel porphyrins detected by Raman spectroscopy at soret excitation. *J. Phys. Chem. A* **109,** 10493–10502 (2005).

67. A. Shelnutt, J. *et al.* Nonplanar porphyrins and their significance in proteins. *Chem. Soc. Rev.* **27,** 31 (1998).

68. Parthasarathi, N., Hansen, C., Yamaguchi, S. & Spiro, T. G. Metalloporphyrin core size resonance Raman marker bands revisited: implications for the interpretation of hemoglobin photoproduct Raman frequencies. *J. Am. Chem. Soc.* **109,** 3865–3871 (1987).

69. Bard, A. J. & Faulkner, L. R. *Electrochemical methods*. (John Wiley & Sons, 2001).

70. Keyes, T. E. & Forster, R. J. *Spectroelectrochemistry*. *Handbook of Electrochemistry* (2007). doi:10.1016/B978-044451958-0.50027-6

71. Larsson, S. Electron Transfer in Proteins. *faraday Trans.* 1375–1388 (1983).

72. Marcus, R. a. Electron Transfer Reactions in Chemistry: Theory and Experiment (Nobel Lecture). *Angew. Chem. Int. Ed.* **32,** 1111–1121 (1993).

73. Gray, H. B. & Winkler, J. R. Electron Transfer in Proteins. *Annu. Rev. Biochem.* **65,** 537–561 (1996).

74. Gray, H. B. & Winkler, J. R. Long-range electron transfer. *Proc. Natl. Acad. Sci. U. S. A.* **102,** 3534–3539 (2005).

75. Beratan, D. N., Betts, J. N. & Onuchic, J. N. Protein Electron Transfer Rates Set by the Bridging Secondary and Tertiary Structure. *Science (80-.).* (1991).

76. Marcus, R. a. Chemical and Electrochemical Electron-Transfer Theory. *Annu. Rev. Phys. Chem.* **15,** 155–196 (1964).

77. www.pineresearch.com.

78. Pine Instrument Company. Honeycomb Spectroelectrochemical Cell User Guide. **10004,** (2013).

79. Sezer, M. *et al.* Multi-layer electron transfer across nanostructured Ag-SAM-Au-SAM junctions probed by surface enhanced Raman spectroscopy. *Phys. Chem. Chem. Phys.* **12,** 9822–9829 (2010).

80. Sezer, M. Spectro-Electrochemical Investigations on Immobilised Heme Proteins. (2011).

81. Ulman, a. Formation and Structure of Self-Assembled Monolayers. *Chem. Rev.* **96,** 1533–1554 (1996).

82. Kissinger, P. T. & Heineman, W. R. Cyclic voltammetry. *J. Chem. Educ.* **60,** 9242–5 (1983).

83. Rahman, H., Hussain, I. & Manirul Haque, S. K. Review on cyclic voltammetric and spectrophotometric approaches for the analysis of drugs (antihypertensive) using different electrodes and wavelength. *Der Pharma Chem.* **7,** 44–55 (2015).

84. Laviron, E. The use of linear potential sweep voltammetry and of a.c. voltammetry for the study of the surface electrochemical reaction of strongly adsorbed systems and of redox modified electrodes. *J. Electroanal. Chem. Interfacial Electrochem.* **100,** 263–270 (1979).

85. Léger, C. & Bertrand, P. Direct electrochemistry of redox enzymes as a tool for mechanistic studies. *Chem. Rev.* **108,** 2379–438 (2008).

86. Batchelor-Mcauley, C. *et al.* Recent Advances in Voltammetry. *ChemistryOpen* **4,** 224–260 (2015).

87. Harnisch, F. & Freguia, S. A basic tutorial on cyclic voltammetry for the investigation of electroactive microbial biofilms. *Chem. - An Asian J.* **7,** 466–475 (2012).

88. Murgida, D. H. & Hildebrandt, P. Redox and redox-coupled processes of heme proteins and enzymes at electrochemical interfaces. *Phys. Chem. Chem. Phys.* **7,** 3773–3784 (2005).

89. Miyake, H., Ye, S. & Osawa, M. Electroless deposition of gold thin films on silicon for surface-enhanced infrared spectroelectrochemistry. *Electrochem. commun.* **4,** 973–977 (2002).

90. Kielb, P. *et al.* Switchable Redox Chemistry of the Hexameric Tyrosine-Coordinated Heme Protein. *J. Phys. Chem. B* **121,** 3955–3964 (2017).

91. Bürgmann, H. *et al.* Transcriptional response of Silicibacter pomeroyi DSS-3 to dimethylsulfoniopropionate (DMSP). *Environ. Microbiol.* **9,** 2742–2755 (2007).

92. Moran, M. A. *et al.* Genome sequence of Silicibacter pomeroyi reveals adaptations to the marine environment. *Nature* **432,** 910–3 (2004).

93. Jeoung, J.-H., Pippig, D. a, Martins, B. M., Wagener, N. & Dobbek, H. HTHP: a novel class of hexameric, tyrosine-coordinated heme proteins. *J. Mol. Biol.* **368,** 1122–31 (2007).

94. Berglund, G. I. *et al.* The catalytic pathway of horseradish peroxidase at high resolution. *Nature* **417,** 463–8 (2002).

95. Murshudov, G. N. *et al.* The structures of Micrococcus lysodeikticus catalase, its ferryl intermediate (compound II) and NADPH complex. *Acta Crystallogr. Sect. D Biol. Crystallogr.* **58,** 1972–1982 (2002).

96. Peng, L. *et al.* Surface-tuned electron transfer and electrocatalysis of hexameric tyrosine-coordinated heme protein. *Chem. - A Eur. J.* **21,** 7596–7602 (2015).

97. Mokry, D. Z. *et al.* HHS Public Access. *Biochim Biophys Acta* **33,** 395–401 (2014).

98. Bennett, E. H. *et al.* HHS Public Access. *Biochemistry* **150,** 137–143 (2015).

99. Eakanunkul, S. *et al.* Characterization of the periplasmic heme-binding protein ShuT from the heme uptake system of Shigella dysenteriae. *Biochemistry* **44,** 13179–13191 (2005).

100. Kumar, R. *et al.* Replacing the axial ligand tyrosine 75 or its hydrogen bond partner histidine 83 minimally affects hemin acquisition by the hemophore HasAp from pseudomonas aeruginosa. *Biochemistry* **53,** 2112–2125 (2014).

101. Peng, L. *et al.* Molecularly imprinted electropolymer for a hexameric heme protein with direct electron transfer and peroxide electrocatalysis. *Sensors (Switzerland)* **16,** 1–11 (2016).

102. Wackerbarth, H., Klar, U., Gunther, W. & Hildebrandt, P. Novel Time-Resolved Surface-Enhanced (Resonance) Raman Spectroscopic Technique for Studying the Dynamics of Interfacial Processes: Application to the Electron Transfer Reaction of Cytochrome c at a Silver Electrode. *Appl. Spectrosc.* **53,** 283–291 (1999).

103. Sezer, M. *et al.* Surface Enhanced Resonance Raman Spectroscopy Reveals Potential Induced Redox and Conformational Changes of Cytochrome c Oxidase on Electrodes. *J. Phys. Chem. B* **119,** 9586–91 (2015).

104. Marrink, S. J., Risselada, H. J., Yefimov, S., Tieleman, D. P. & de Vries, A. H. The MARTINI Force Field: Coarse Grained Model for Biomolecular Simulations. *J. Phys. Chem. B* **111,** 7812–7824 (2007).

105. de Jong, D. H. *et al.* Improved Parameters for the Martini Coarse-Grained Protein Force Field. *J. Chem. Theory Comput.* **9,** 687–697 (2013).

106. Monticelli, L. *et al.* The MARTINI Coarse-Grained Force Field: Extension to Proteins. *J. Chem. Theory Comput.* **4,** 819–834 (2008).

107. de Jong, D. H. *et al.* Atomistic and Coarse Grain Topologies for the Cofactors Associated with the Photosystem II Core Complex. *J. Phys. Chem. B* **119,** 7791–7803 (2015).

108. Periole, X., Cavalli, M., Marrink, S.-J. & Ceruso, M. A. Combining an Elastic Network With a Coarse-Grained Molecular Force Field: Structure, Dynamics, and Intermolecular Recognition. *J. Chem. Theory Comput.* **5,** 2531–2543 (2009).

109. Darden, T., York, D. & Pedersen, L. Particle mesh Ewald: An N·log(N) method for Ewald sums in large systems. *J. Chem. Phys.* **98,** 10089–10092 (1993).

110. Yesylevskyy, S. O., Schäfer, L. V, Sengupta, D. & Marrink, S. J. Polarizable Water Model for the Coarse-Grained MARTINI Force Field. *PLOS Comput. Biol.* **6,** e1000810 (2010).

111. Van Der Spoel, D. *et al.* GROMACS: Fast, flexible, and free. *J. Comput. Chem.* **26,** 1701–1718 (2005).

112. Parrinello, M. & Rahman, A. Polymorphic transitions in single crystals: A new molecular dynamics method. *J. Appl. Phys.* **52,** 7182–7190 (1981).

113. Bussi, G., Donadio, D. & Parrinello, M. Canonical sampling through velocity rescaling. *J. Chem. Phys.* **126,** 14101 (2007).

114. Kitagawa, T. *et al.* Resonance Raman Spectra of Metallooctaethylporphyrins . Low Frequency. **80,** (1976).

115. Nagai, K., Kagimoto, T., Hayashi, A., Taketa, F. & Kitagawa, T. Resonance raman studies of hemoglobins M: evidence for iron-tyrosine charge-transfer interactions in the abnormal subunits of Hb M Boston and Hb M Iwate. *Biochemistry* **22,** 1305–1311 (1983).

116. Sezer, M. *et al.* Distinct structural and redox properties of the heme active site in bacterial dye decolorizing peroxidase-type peroxidases from two subfamilies: resonance Raman and electrochemical study. *Biochemistry* **52,** 3074–3084 (2013).

117. Zámocký, M. *et al.* High conformational stability of secreted eukaryotic catalase-peroxidases: Answers from first crystal structure and unfolding studies. *J. Biol. Chem.* **287,** 32254–32262 (2012).

118. Chuang, W. J., Johnson, S. & Van Wart, H. E. Resonance Raman spectra of bovine liver catalase: Enhancement of proximal tyrosinate vibrations. *J. Inorg. Biochem.* **34,** 201–219 (1988).

119. Ly, H. K. *et al.* Thermal fluctuations determine the electron-transfer rates of cytochrome c in electrostatic and covalent complexes. *ChemPhysChem* **11,** 1225–1235 (2010).

120. Döpner, S., Hildebrandt, P., Mauk, A. G., Lenk, H. & Stempfle, W. Analysis of vibrational spectra of multicomponent systems. Application to pH-dependent resonance Raman spectra of ferricytochrome c. *Spectrochim. Acta A* **51,** 573–584 (1996).

121. Sharma, K. D., Andersson, L. A., Loehr, T. M., Terner, J. & Goff, H. M. Comparative Spectral Analysis of Mammalian, Fungal, and Bacterial Catalases. *J. Biol. Chem.* **264,** 12772–12779 (1989).

122. Arnoux, P. *et al.* The crystal structure of HasA, a hemophore secreted by Serratia marcescens. *Nat. Struct. Biol.* **6,** 516–20 (1999).

123. Bandara, D. M. I., Sono, M., Bruce, G. S., Brash, A. R. & Dawson, J. H. Coordination modes of tyrosinate-ligated catalase-type heme enzymes: Magnetic circular dichroism studies of Plexaura homomalla allene oxide synthase, Mycobacterium avium ssp. paratuberculosis protein-2744c, and bovine liver catalase in their ferric and fe. *J. Inorg. Biochem.* **105,** 1786–1794 (2011).

124. Kassner, R. J. Effects of Nonpolar Environments on the Redox Potentials of Heme Complexes. *Proc. Natl. Acad. Sci. U. S. A.* **69,** 2263–2267 (1972).

125. Trasatti, S. Work function, electronegativity, and electrochemical behaviour of metals. II. Potentials of zero charge and 'electrochemical' work functions. *J. Electroanal. Chem.* **33,** 351–378 (1971).

126. Valette, G. Hydrophilicity of metal surfaces. Silver, gold and copper electrodes. *J. Electroanal. Chem.* **139,** 285–301 (1982).

127. Gámiz-Hernández, A. P., Kieseritzky, G., Galstyan, A. S., Demir-Kavuk, O. & Knapp, E. W. Understanding properties of cofactors in proteins: Redox potentials of synthetic cytochromes b. *ChemPhysChem* **11,** 1196–1206

(2010).

128. Battistuzzi, G., Borsari, M., Sola, M. & Francia, F. Redox thermodynamics of the native and alkaline forms of eukaryortic and bacterial class I cytochromes c. *Biochemistry* **36,** 16247–16258 (1997).

129. Oellerich, S., Wackerbarth, H. & Hildebrandt, P. Spectroscopic characterization of nonnative conformational states of cytochrome c. *J. Phys. Chem. B* **106,** 6566–6580 (2002).

130. Todorovic, S., Jung, C., Hildebrandt, P. & Murgida, D. H. Conformational transitions and redox potential shifts of cytochrome P450 induced by immobilization. *J. Biol. Inorg. Chem.* **11,** 119–127 (2006).

131. Rivas, L. *et al.* Electric-Field Induced Redox Potential Shifts of Tetraheme Cytochromes c3 Immobilised on Self-Assembled Monolayers. Surface Enhanced Resonance Raman Spectroscopy and Simulation Studies. *Biophys. J.* **88,** 4188–4199 (2005).

132. Oellerich, S., Wackerbarth, H. & Hildebrandt, P. Conformational equilibria and dynamics of cytochrome c induced by binding of sodium dodecyl sulfate monomers and micelles. *Eur. Biophys. J.* **32,** 599–613 (2003).

133. Kranich, A., Ly, H. K., Hildebrandt, P. & Murgida, D. H. Direct Observation of the Gating Step in Protein Electron Transfer : Electric-Field-Controlled Protein Dynamics. *JACS* 9844–9848 (2008).

134. Stark, A. C., Andrews, C. T. & Elcock, A. H. Toward optimized potential functions for protein-protein interactions in aqueous solutions: osmotic second virial coefficient calculations using the MARTINI coarse-grained force field. *J. Chem. Theory Comput.* **9,** 10.1021/ct400008p (2013).

135. Murgida, D. H. & Hildebrandt, P. Electron-transfer processes of cytochrome c at interfaces. New insights by surface-enhanced resonance Raman spectroscopy. *Acc. Chem. Res.* **37,** 854–861 (2004).

136. Cescau, S. *et al.* Heme acquisition by hemophores. *BioMetals* **20,** 603–613 (2007).

137. Eriksson, K. E., Pettersson, B. & Westermark, U. Oxidation: An important enzyme reaction in fungal degradation of cellulose. *FEBS Lett.* **49,** 282–285 (1974).

138. Bao, W., Usha, S. N. & Renganathan, V. Purification and Characterization of Cellobiose Dehydrogenase, a Novel Extracellular Hemoflavoenzyme from the White-Rot Fungus Phanerochaete chrysosporium. *Arch. Biochem. Biophys.* **300,** 705–713 (1993).

139. Harreither, W. *et al.* Catalytic properties and classification of cellobiose dehydrogenases from ascomycetes. *Appl. Environ. Microbiol.* **77,** 1804–1815 (2011).

140. Rotsaert, F. a J. *et al.* Biophysical and structural analysis of a novel heme B iron ligation in the flavocytochrome cellobiose dehydrogenase. *J. Biol. Chem.* **278,** 33224–31 (2003).

141. Ludwig, R., Harreither, W., Tasca, F. & Gorton, L. Cellobiose dehydrogenase: a versatile catalyst for electrochemical applications. *Chemphyschem* **11,** 2674–97 (2010).

142. Zámocký, M. *et al.* Cloning, sequence analysis and heterologous expression in Pichia pastoris of a gene encoding a thermostable cellobiose dehydrogenase from Myriococcum thermophilum. *Protein Expr. Purif.* **59,** 258–65 (2008).

143. Sulej, J. *et al.* Characterization of Cellobiose Dehydrogenase from a Biotechnologically Important Cerrena unicolor Strain. *Appl. Biochem. Biotechnol.* **176,** 1638–1658 (2015).

144. Coman, V. *et al.* A Direct Electron Transfer-Based Glucose/Oxygen Biofuel Cell Operating in Human Serum. *Fuel Cells* 9–16 (2010). doi:10.1002/fuce.200900121

145. Samejima, M. & Eriksson, K. E. L. A comparison of the catalytic properties of cellobiose:quinone oxidoreductase and cellobiose oxidase from Phanerochaete chrysosporium. *Eur. J. Biochem.* **207,** 103–107 (1992).

146. Clark, L. C. & Lyons, C. Electrode systems for continuous monitoring in cardiovascular surgery. *Ann. N. Y. Acad. Sci.* **102,** 29–45 (1962).

147. Wang, J. Electrochemical Glucose Biosensors. *Chem. Rev.* **108,** 814–825 (2007).

148. Wang, J. Glucose biosensors: 40 Years of advances and challenges. *Electroanalysis* **13,** 983–988 (2001).

149. Tasca, F. *et al.* Highly Efficient and Versatile Anodes for Biofuel Cells Based on Cellobiose Dehydrogenase from Myriococcum thermophilum. **112,** 13668–13673 (2008).

150. Ludwig, R. *et al.* Cellobiose dehydrogenase modified electrodes: advances by materials science and biochemical engineering. *Anal. Bioanal. Chem.* **405,** 3637–3658 (2013).

151. Kovacs, G. *et al.* Graphite electrodes modified with Neurospora crassa cellobiose dehydrogenase: comparative

electrochemical characterization under direct and mediated electron transfer. *Bioelectrochemistry* **88,** 84–91 (2012).

152. Tasca, F., Harreither, W., Ludwig, R., Gooding, J. J. & Gorton, L. Cellobiose Dehydrogenase Aryl Diazonium Modified Single Walled Positively Charged Surface. **83,** 3042–3049 (2011).

153. Safina, G., Ludwig, R. & Gorton, L. A simple and sensitive method for lactose detection based on direct electron transfer between immobilised cellobiose dehydrogenase and screen-printed carbon electrodes. *Electrochim. Acta* **55,** 7690–7695 (2010).

154. Igarashi, K. *et al.* ENZYMOLOGY : Cellobiose Dehydrogenase from the Fungi Phanerochaete chrysosporium and Humicola insolens : A FLAVOHEMOPROTEIN FROM 6-HYDROXY-FAD AS THE DOMINANT ACTIVE COFACTOR Cellobiose Dehydrogenase from the Fungi Phanerochaete chrysosporium and Humicola. (1999).

155. Stoica, L., Dimcheva, N., Haltrich, D., Ruzgas, T. & Gorton, L. Electrochemical investigation of cellobiose dehydrogenase from new fungal sources on Au electrodes. *Biosens. Bioelectron.* **20,** 2010–8 (2005).

156. Matsumura, H. *et al.* Direct Electrochemistry of Phanerochaete chrysosporium Cellobiose Dehydrogenase Covalently Attached onto Gold Nanoparticle Modi fi ed Solid Gold Electrodes. **28,** 10925–10933 (2012).

157. Yue, H., Waldeck, D. H., Petrović, J. & Clark, R. a. The effect of ionic strength on the electron-transfer rate of surface immobilized cytochrome C. *J. Phys. Chem. B* **110,** 5062–5072 (2006).

158. Sezer, M. *et al.* Redox properties and catalytic activity of surface-bound human sulfite oxidase studied by a combined surface enhanced resonance Raman spectroscopic and electrochemical approach. *Phys. Chem. Chem. Phys.* **12,** 7894–7903 (2010).

159. Baldwin, R. L. How Hofmeister Ions Affect Protein Stability. *Biophys. J.* **71,** 2056–2063 (1996).

160. Ahmad, A., Akhtar, S. & Bhakuni, V. Monovalent cation-induced conformational change in glucose oxidase leading to stabilization of the enzyme. *Biochemistry* **40,** 1945–1955 (2001).

161. Mould, A. P., Garratt, A. N., Puzon-McLaughlin, W., Takada, Y. & Humphries, M. J. Regulation of integrin function: evidence that bivalent-cation-induced conformational changes lead to the unmasking of ligand-binding sites within integrin alpha5 beta1. *Biochem. J.* **828,** 821–8 (1998).

162. Jeuken, L. J. C. Conformational reorganisation in interfacial protein electron transfer. *Biochim. Biophys. Acta - Bioenerg.* **1604,** 67–76 (2003).

163. Maheshwari, R., Bharadwaj, G. & Bhat, M. K. Thermophilic Fungi: Their Physiology and Enzymes. *Microbiol. Mol. Biol. Rev.* **64,** 461–488 (2000).

164. Harreither, W., Coman, V., Ludwig, R., Haltrich, D. & Gorton, L. Investigation of Graphite Electrodes Modified with Cellobiose Dehydrogenase from the AscomyceteMyriococcum thermophilum. *Electroanalysis* **19,** 172–180 (2007).

165. Schulz, C., Ludwig, R. & Gorton, L. Polyethyleneimine as a Promoter Layer for the Immobilization of Cellobiose Dehydrogenase from Myriococcum thermophilum on Graphite Electrodes. *Anal. Chem.* **86,** 4256–4263 (2014).

166. Coman, V., Harreither, W., Ludwig, R., Haltrich, D. & Gorton, L. Investigation of Electron Transfer Between Cellobiose Dehydrogenase From Myriococcum Thermophilum and Gold Electrodes. *Chem. Analityczna* **945,** 945–960 (2007).

167. Larsson, T., Lindgren, A. & Ruzgas, T. Spectroelectrochemical study of cellobiose dehydrogenase and diaphorase in a thiol-modified gold capillary in the absence of mediators. *Bioelectrochemistry* **53,** 243–249 (2001).

168. Schulz, C. *et al.* Enhancement of enzymatic activity and catalytic current of cellobiose dehydrogenase by calcium ions. *Electrochem. commun.* **17,** 71–74 (2012).

169. Sezer, M., Millo, D., Weidinger, I. M., Zebger, I. & Hildebrandt, P. Analyzing the catalytic processes of immobilized redox enzymes by vibrational spectroscopies. *IUBMB Life* **64,** 455–464 (2012).

170. Sezer, M. *et al.* Redox properties and catalytic activity of surface-bound human sulfite oxidase studied by a combined surface enhanced resonance Raman spectroscopic and electrochemical approach. *Phys. Chem. Chem. Phys.* **12,** 7894–903 (2010).

171. Sezer, M. *et al.* Role of the HoxZ subunit in the electron transfer pathway of the membrane-bound [NiFe]-hydrogenase from Ralstonia eutropha immobilized on electrodes. *J. Phys. Chem. B* **115,** 10368–10374 (2011).

172. Hrabakova, J., Ataka, K., Heberle, J., Hildebrandt, P. & Murgida, D. H. Long distance electron transfer in cytochrome c oxidase immobilised on electrodes. A surface enhanced resonance Raman spectroscopic study. *Phys. Chem. Chem. Phys.* **8,** 759–66 (2006).

173. Millo, D., Hildebrandt, P., Pandelia, M.-E., Lubitz, W. & Zebger, I. SEIRA spectroscopy of the electrochemical activation of an immobilized [NiFe] hydrogenase under turnover and non-turnover conditions. *Angew. Chem. Int. Ed. Engl.* **50,** 2632–2634 (2011).

174. Wisitruangsakul, N. *et al.* Monitoring catalysis of the membrane-bound hydrogenase from Ralstonia eutropha H16 by surface-enhanced IR absorption spectroscopy. *Angew. Chem. Int. Ed. Engl.* **48,** 611–613 (2009).

175. Knöös, P. *et al.* Quantifying the release of lactose from polymer matrix tablets with an amperometric biosensor utilizing cellobiose dehydrogenase. *Int. J. Pharm.* **468,** 121–132 (2014).

176. Cohen, J. D., Bao, W., Renganathan, V., Subramaniam, S. S. & Loehr, T. M. Resonance Raman spectroscopic studies of cellobiose dehydrogenase from Phanerochaete chrysosporium. *Arch. Biochem. Biophys.* **341,** 321–328 (1997).

177. Wisitruangsakul, N. *et al.* Redox-linked protein dynamics of cytochrome c probed by time-resolved surface enhanced infrared absorption spectroscopy. *Phys. Chem. Chem. Phys.* **10,** 5276–5286 (2008).

178. Owusu-nkwantabisah, S., Gammana, M. & Tripp, C. P. Dynamics of Layer-by-Layer Growth of a Polyelectrolyte Multilayer Studied in Situ Using Attenuated Total Re fl ectance Infrared Spectroscopy. *Langmuir* **30,** 11696–11703 (2014).

179. Petrović, J., Clark, R. a, Yue, H., Waldeck, D. H. & Bowden, E. F. Impact of surface immobilization and solution ionic strength on the formal potential of immobilized cytochrome C. *Langmuir* **21,** 6308–6316 (2005).

180. Alvarez-Paggi, D. *et al.* Disentangling electron tunneling and protein dynamics of cytochrome c through a rationally designed surface mutation. *J. Phys. Chem. B* **117,** 6061–6068 (2013).

181. Hunter, C. L. *et al.* Introduction and characterization of a functionally linked metal ion binding site at the exposed heme edge of myoglobin. *Proc. Natl. Acad. Sci. U. S. A.* **100,** 3647–3652 (2003).

182. Hallberg, B. M., Henriksson, G., Pettersson, G. & Divne, C. Crystal structure of the flavoprotein domain of the extracellular flavocytochrome cellobiose dehydrogenase. *J. Mol. Biol.* **315,** 421–34 (2002).

183. Satyapal, S., Petrovic, J., Read, C., Thomas, G. & Ordaz, G. The U.S. Department of Energy's National Hydrogen Storage Project: Progress towards meeting hydrogen-powered vehicle requirements. *Catal. Today* **120,** 246–256 (2007).

184. Artero, V. & Fontecave, M. Solar fuels generation and molecular systems: is it homogeneous or heterogeneous catalysis? *Chem. Soc. Rev.* **42,** 2338–56 (2013).

185. Eckenhoff, W. T. & Eisenberg, R. Molecular systems for light driven hydrogen production. *Dalt. Trans.* **41,** 13004–13021 (2012).

186. Bediako, D. K. *et al.* Role of pendant proton relays and proton-coupled electron transfer on the hydrogen evolution reaction by nickel hangman porphyrins. *Proc. Natl. Acad. Sci. U. S. A.* **111,** 15001–15006 (2014).

187. Lee, C. H., Dogutan, D. K. & Nocera, D. G. Hydrogen generation by hangman metalloporphyrins. *J. Am. Chem. Soc.* **133,** 8775–8777 (2011).

188. Solis, B. H., Maher, A. G., Dogutan, D. K., Nocera, D. G. & Hammes-Schiffer, S. Nickel phlorin intermediate formed by proton-coupled electron transfer in hydrogen evolution mechanism. *Proc Natl Acad Sci U S A* **113,** 485–492 (2016).

189. Solis, B. H. *et al.* Theoretical analysis of cobalt hangman porphyrins: Ligand dearomatization and mechanistic implications for hydrogen evolution. *ACS Catal.* **4,** 4516–4526 (2014).

190. Mahammed, A., Mondal, B., Rana, A., Dey, A. & Gross, Z. The cobalt corrole catalyzed hydrogen evolution reaction: surprising electronic effects and characterization of key reaction intermediates. *Chem. Commun. (Camb).* **50,** 2725–7 (2014).

191. Sengupta, K., Chatterjee, S., Samanta, S., Bandyopadhyay, S. & Dey, A. Resonance Raman and electrocatalytic behavior of thiolate and imidazole bound iron porphyrin complexes on self assembled monolayers: functional modeling of cytochrome P450. *Inorg. Chem.* **52,** 2000–14 (2013).

192. Rigsby, M. L., Wasylenko, D. J., Pegis, M. L. & Mayer, J. M. Medium Effects Are as Important as Catalyst Design for Selectivity in Electrocatalytic Oxygen Reduction by Iron-Porphyrin Complexes. *J. Am. Chem. Soc.* **137,** 4296–4299 (2015).

193. Levy, N. *et al.* Metallocorroles as Non-Precious Metal Electrocatalysts for Highly Efficient Oxygen Reduction in Alkaline Media. 2832–2837 (2016). doi:10.1002/cctc.201600556

194. Wang, D. & Groves, J. T. Efficient water oxidation catalyzed by homogeneous cationic cobalt porphyrins with

critical roles for the buffer base. *Proc. Natl. Acad. Sci. U. S. A.* **110,** 15579–84 (2013).

195. Raugei, S. *et al.* Experimental and Computational Mechanistic Studies Guiding the Rational Design of Molecular Electrocatalysts for Production and Oxidation of Hydrogen. *Inorg. Chem.* **55,** 445–460 (2016).

196. Marinescu, S. C., Winkler, J. R. & Gray, H. B. Molecular mechanisms of cobalt-catalyzed hydrogen evolution. *Proc. Natl. Acad. Sci.* **109,** 15127–15131 (2012).

197. Hu, S., Morris, I. K., Singh, J. P., Smith, K. M. & Spiro, T. G. Complete assignment of cytochrome c resonance Raman spectra via enzymic reconstitution with isotopically labeled hemes. *J. Am. Chem. Soc.* **115,** 12446–12458 (1993).

198. Terekhov, S. N. *et al.* Resonance Raman characterization of cationic Co(II) and Co(III) tetrakis(N-methyl-4-pyridinyl)porphyrins in aqueous and non-aqueous media. *J. Raman Spectrosc.* **34,** 868–881 (2003).

199. Terekhov, S. N., Galievsky, V. a., Chirvony, V. S. & Turpin, P.-Y. Resonance Raman and absorption characterization of cationic Co(II)-porphyrin in its complexes with nucleic acids: binding modes, nucleic base specificity and role of water in Co(II) oxidation processes. *J. Raman Spectrosc.* **36,** 962–973 (2005).

200. Chang, C. J., Chng, L. L. & Nocera, D. G. Proton-coupled O-O activation on a redox platform bearing a hydrogen-bonding scaffold. *J. Am. Chem. Soc.* **125,** 1866–1876 (2003).

201. Zhou, W. *et al.* Reducing zirconium(IV) phthalocyanines and the structure of a Pc4−Zr complex. *Dalt. Trans.* **2,** 13955–13961 (2015).

202. Frisch, M. J. *et al. Gaussian 09, Revision B.01; Gaussian. Inc.: Wallingford, CT* 2009–2009 (2010). doi:111

203. Perdew, J. P. Density-functional approximation for the correlation energy of the inhomogeneous electron gas. *Phys. Rev. B* **33,** 8822–8824 (1986).

204. Becke, A. D. Density-functional exchange-energy approximation with correct asymptotic behavior. *Phys. Rev. A* **38,** 3098–3100 (1988).

205. Rauhut, G. & Pulay, P. Transferable Scaling Factors for Density-Functional Derived Vibrational Force-Fields. *J. Phys. Chem.* **99,** 3093–3100 (1995).

206. Weigend, F. & Ahlrichs, R. Balanced basis sets of split valence, triple zeta valence and quadruple zeta valence quality for H to Rn: Design and assessment of accuracy. *Phys. Chem. Chem. Phys.* **7,** 3297–305 (2005).

207. Tomasi, J., Mennucci, B. & Cammi, R. Quantum mechanical continuum solvation models. *Chem. Rev.* **105,** 2999–3093 (2005).

208. Polavarapu, P. L. Ab initio vibrational Raman and Raman optical activity spectra. *J. Phys. Chem.* **94,** 8106–8112 (1990).

209. Rush, T. S. *et al.* Computational modeling of metalloporphyrin structure and vibrational spectra: Porphyrin ruffling in NiTPP. *J. Phys. Chem. B* **104,** 5020–5034 (2000).

210. Lin, C., Spiro, T. G. & April, R. V. Structural Distortion of the Vanadyltetraphenylporphine Anion Radical Probed by Resonance Raman Spectroelectrochemistry. **1669,** 5237–5243 (1996).

211. Reed, R. A., Purrello, R., Prendergast, K. & Spiro, T. G. Resonance Raman characterization of the radical anion and triplet states of zinc tetraphenylporphine. *J. Phys. Chem.* **95,** 9720–9727 (1991).

212. Stallard, B. R., Callis, P. R., Champion, P. M. & Albrecht, A. C. Application of the transform theory to resonance Raman excitation profiles in the Soret region of cytochrome-c. *J. Chem. Phys.* **80,** 70 (1984).

213. Kozlowski, P. M., Bingham, J. R. & Jarzecki, A. A. Theoretical Analysis of Core Size Effect in Metalloporphyrins. *J. Phys. Chem. A* **112,** 12781–12788 (2008).

214. Perutz, R. N. & Procacci, B. Photochemistry of Transition Metal Hydrides. *Chem. Rev.* **116,** 8506–8544 (2016).

215. Siebert, E. *et al.* Resonance raman spectroscopy as a tool to monitor the active site of hydrogenases. *Angew. Chemie - Int. Ed.* **52,** 5162–5165 (2013).

216. Schulz, C., Kittl, R., Ludwig, R. & Gorton, L. Direct Electron Transfer from the FAD Cofactor of Cellobiose Dehydrogenase to Electrodes. *ACS Catal.* **6,** 555–563 (2016).

217. Bode, D. D., Andersen, T. N. & Eyring, H. Anion and pH effects on the potentials of zero charge of gold and silver electrodes. *J. Phys. Chem.* **71,** 792–797 (1967).

VI. APPENDIX

6.1 Appendix for chapter 4.1

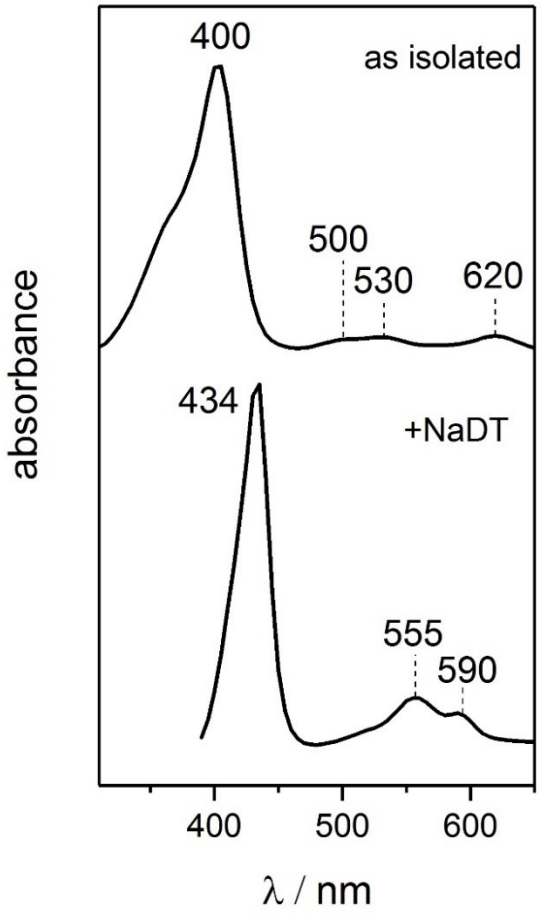

Figure 6.1.1 UV-VIS absorbance spectra of (top) as isolated HTHP and (bottom) after addition of 3 times excess of NaDT in anaerobic conditions to HTHP solution, at 20 mM pH 8 Tris buffer.

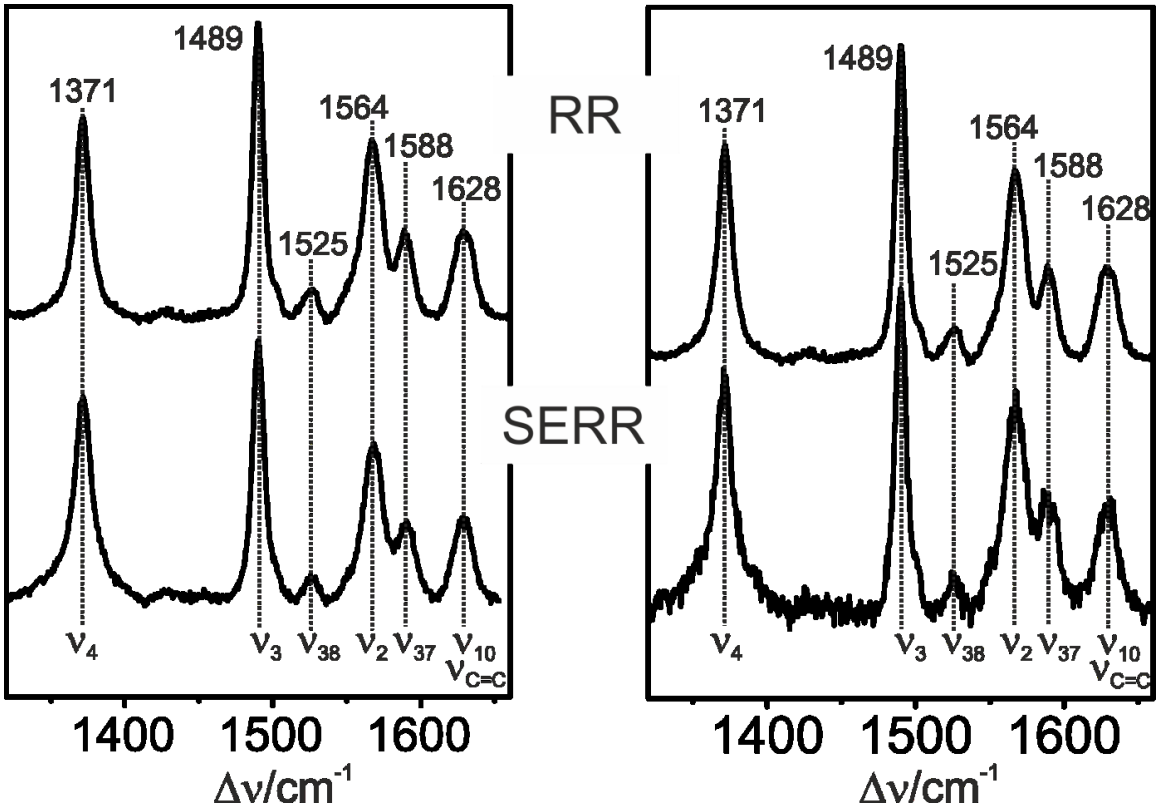

Figure 6.1.2 SERR spectra of the covalently (left) and electrostatically bound HTHP (right) compared with the RR spectra

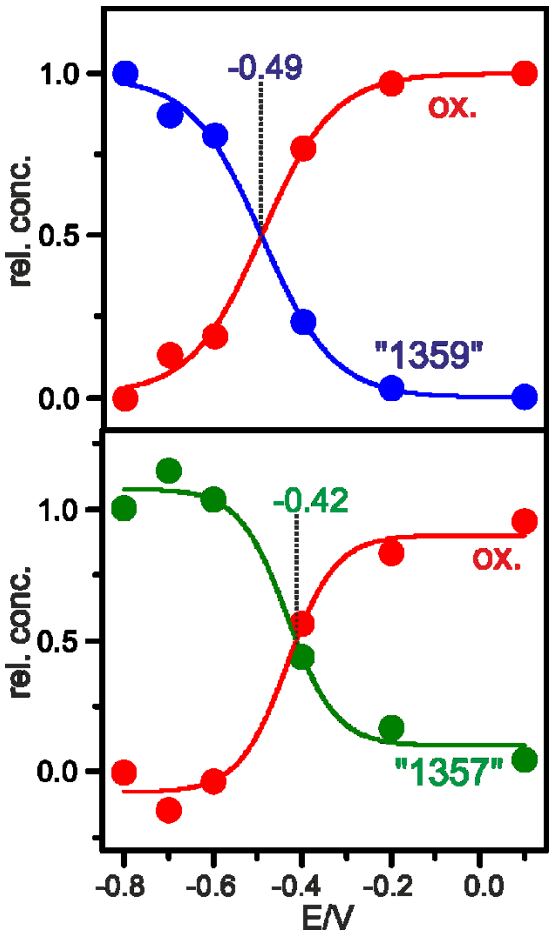

Figure 6.1.3 Nernstian analysis of the redox transition of the species I and II in covalently bound HTHP, as described in detail below.

Details of component analysis

Component analysis of ν_4 band region in SERR potential dependent spectra of covalently bound HTHP revealed three components, two for reduced species : '1357' present at 1357 cm^{-1} and '1359' at 1359 cm^{-1} and one for oxidizes species present at 1371 cm^{-1}. To convert these obtained intensities from band fitting into the relative concentrations, intensities of oxidizes species were multiplied by a factor (R_f) of 1.19 and the intensities of the reduced species were taken as obtained from the spectra. The total concentration c_{tot} of the adsorbed protein was a summation of all obtained intensities of reduced and oxidized species at each potential, according to (1):

$$c_{tot} = R_f * c_{ox} + c_{red\ 1357} + c_{red\ 1359} \qquad (1)$$

The result of summation at each potential slightly differed, therefore it was normalized to the c_{tot} value at 100mV potential and kept constant in further calculations.

The oxidized species in the spectra contain a fraction, which is potential independent and present in all spectra (2). Hence, it was assumed that this fraction is redox inactive and its contribution was subtracted from the intensities of the oxidized species.

$$c_{ox} = c_{active} + c_{inactive} \qquad (2)$$

The mole fractions of the reduced species were not equal, and were determined by inspection of their intensities at most negative potentials (-800 mV). There we can see that contribution of '1359' species is equal to *ca*. 0.466 and '1357' species of *ca*. 0.22.

The obtained mole fractions were kept constant as sum of oxidized and reduced species for each two species at each potential.

Relative concentration as (3) were calculated and plotted against the potential. Fitting the results with Nernst equation allowed to obtain the redox equilibria for each redox active couple and were found to be at -0.49 V for '1359' redox couple and at -0.42 V for '1357' redox couple.

$$c_{red\ 1} = \frac{c_{red\ 1}}{c_{red\ 1} + c_{red\ 2} + c_{ox\ active}} \qquad (3)$$

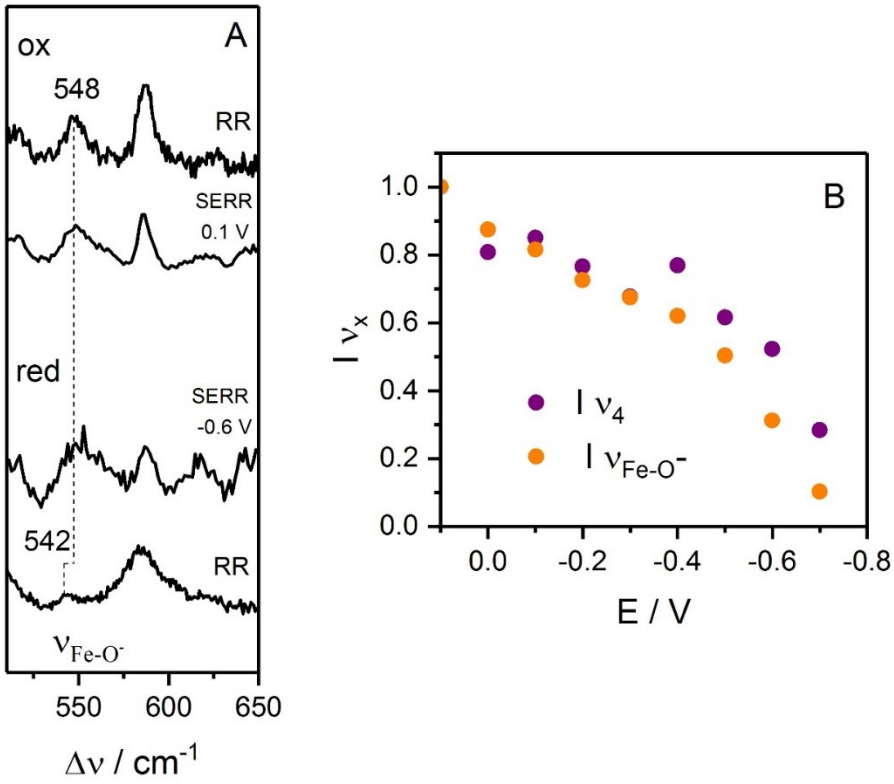

Figure 6.1.4 (A) Low frequency region of the SERR spectra of covalently bound HTHP at positive and negative potential compared to RR spectra of HTHP in solution. (B) Potential-dependent change of normalized intensity of ν_4 and ν_{Fe-O}- vibrations measured at +0.1 V potential after each potential step.

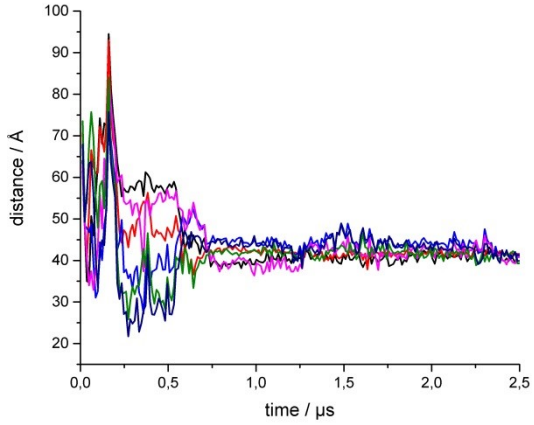

Figure 6.1.5[5] Temporal evolution of the distances between the central beads of the hemes and the gold surface during a CG MD simulation. After initial reorientation, HTHP adopted the "reverse disc". In this state, differences in the heme-Au distances of more than 10 Å were observed.

[5] Done by Dr. T. Utesch (TU Berlin)

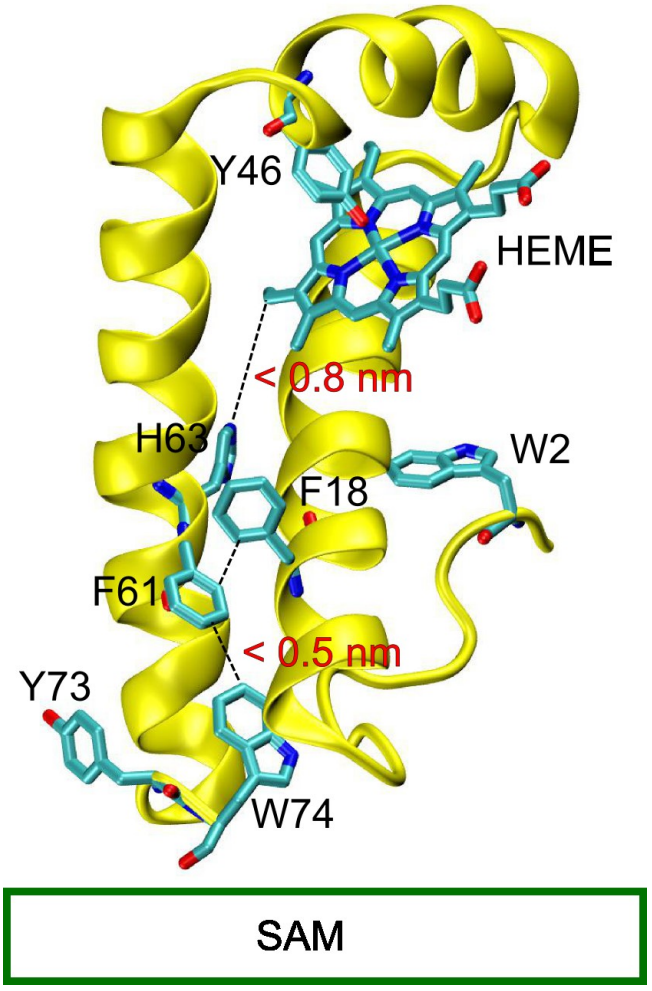

Figure 6.1.6[6] HTHP monomer. The protein backbone is shown in yellow and the heme and all aromatic residues are highlighted.

[6] Done by Dr. T. Utesch (TU Berlin)

6.2 Appendix for chapter 4.2

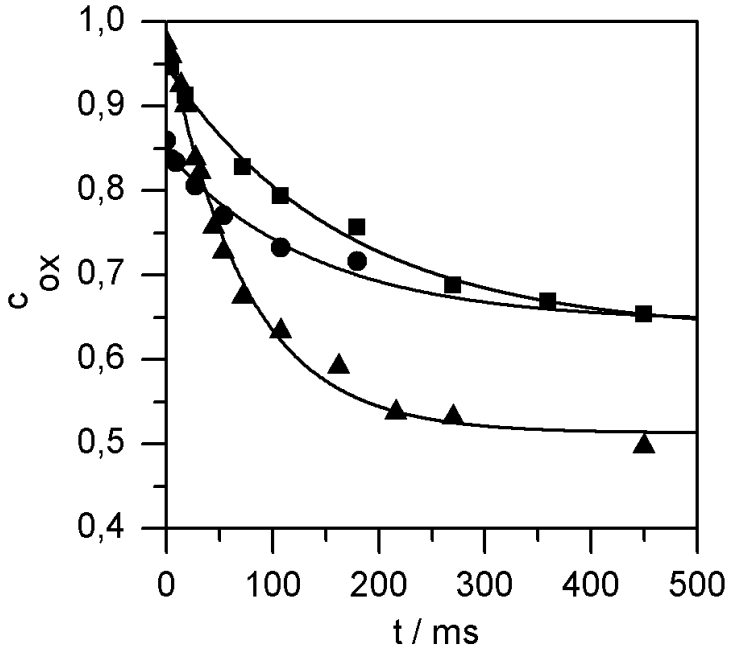

Figure 6.2.1 Time-dependent changes of the relative concentrations of the oxidized form of *Mt*CDH immobilized on an silver electrode followed by potential jump from 100 mV to respective midpoint potentials, in (●) 50 mM acetate buffer + 10 mM $CaCl_2$ (■) 50 mM acetate buffer (▲) 200 mM acetate buffer.

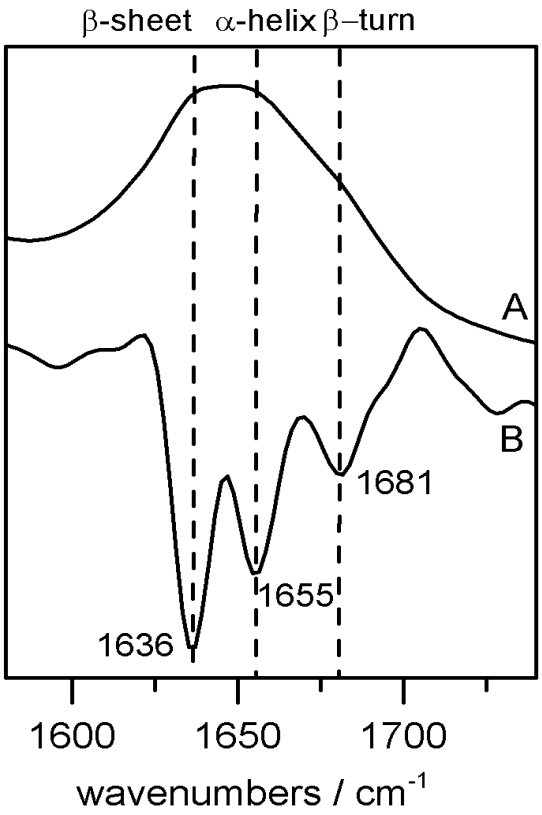

Figure 6.2.2 SEIRA spectrum of immobilized *Mt*CDH on gold in the Amide I region. A: absorbance; B: second derivative.

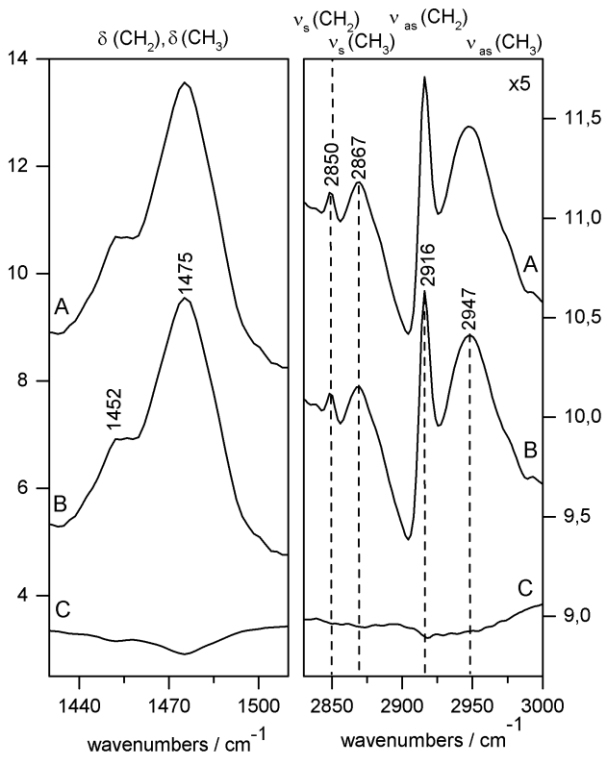

Figure 6.2.3 SEIRA spectra of PDADMAC on a gold electrode before (A) and after (B) the addition of 10 mM $CaCl_2$ in 50 mM acetate buffer. (C) displays the corresponding difference spectrum (B-A). The dashed line (---) indicates position of the aliphatic C-H stretching and bending vibrations of PDADMAC:

6.3 Appendix for chapter 4.3

Potential–dependent composition of the compounds on the electrode surface

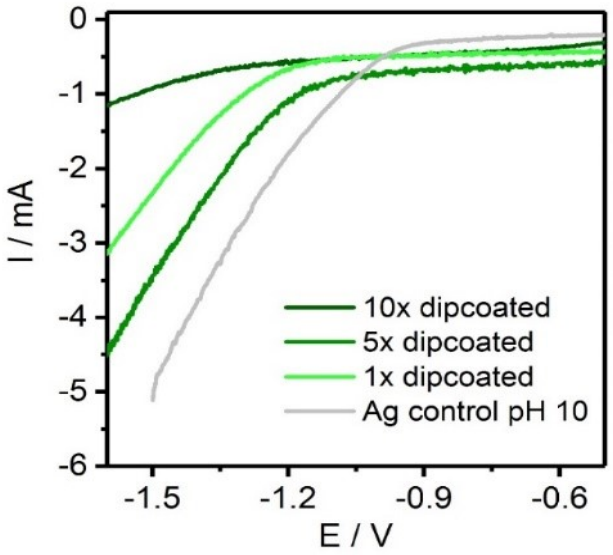

Figure 6.3.1 The catalytic current measured at 5 mV/s scan rate at pH 10 conditions of electrode dip-coated one time (light green), five times (darker green), and ten times (darkest green) in CoPCOOH diluted in acetonitrile solution. Grey line corresponds to catalytic current of bare roughened silver electrode.

With increasing the number of dip-coating insertions of an electrode into a compound containing (in relatively low concentrations) solution, the amount of attached layer of catalyst increases, which is represented by Figure S2 by increased intensity of SERR spectra. Increased amount of compounds on the electrode surface result in increased catalytic activity (measured at pH 10 conditions) up to the certain amount (5 times dip-coated electrode) and then the catalytic rate decreases. For compounds dip-coated in highly concentrated solution, the catalytic activity is found to be the lowest. It seems that due to the high amount of catalyst on the surface, the activity of some layers is inactivated. By plotting normalized (in respect to the ν_4/ν_2 ratio of compounds measured at open circuit) intensity of ν_4 porphyrin vibration (Figure S3), the potential points of reverse intensity behavior are observed. The observation is the same for certain pH (-1.1 V at pH 10 and -0.8 V at pH 4), regardless of the type of compound. The value of potential would fit to reported in literature values for the pH-dependent potential of zero charge of silver.[217] The fact that the observation is pH-dependent might further suggest that compounds are not uniformly distributed over the electrode surface, forming rather condensed islands with unoccupied spots of bare silver. Another interesting observation is significantly decreased intensity of vibrational mode below indicated potential values. To further speculate, the result could be explained based on formed catalytic intermediates during the experiment. Reduction of Co^{II} to Co^{I} state leads to change of total net charge of compounds from neutral to negatively charged. This might further induce repulsion of Co^{I} species from the electrode surface below indicated potentials and cause overall reorientation of layers of species giving rise to the overall decrease of intensity.

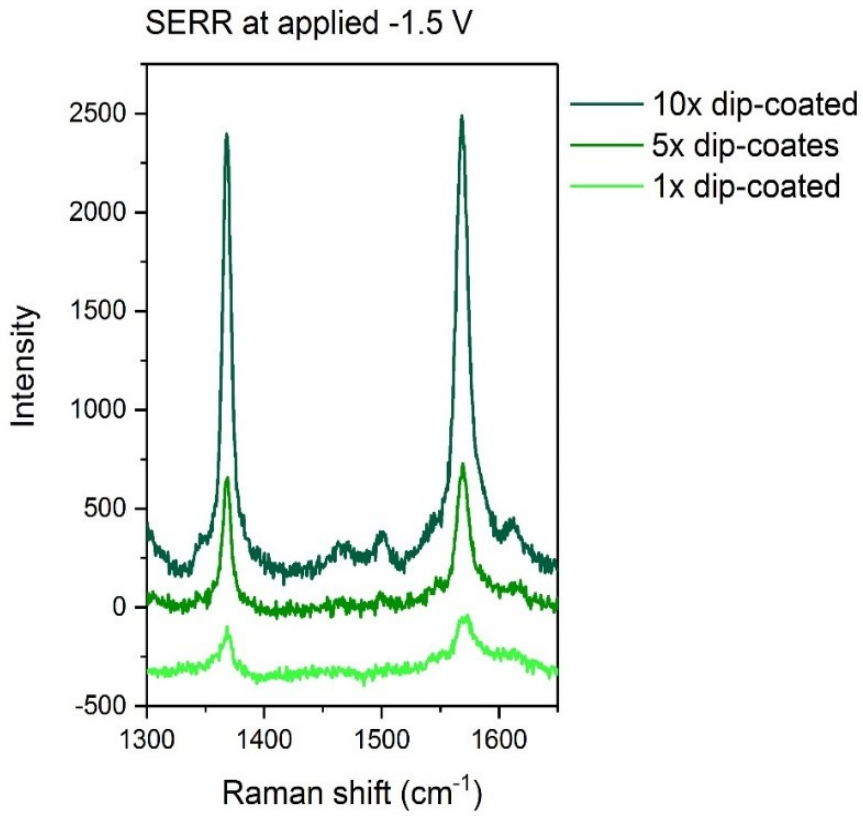

Figure 6.3.2 SERR spectra of CoPCOOH immobilized on the electrode via dip-coating method (light green: electrode dip-coated one time, darker green: electrode dip-coated five times, darkest green: electrode dip-coated ten times), measured at applied -1.5 V at pH 10 conditions. All spectra were accumulated 6 times for 10 s and averaged, with 600μW laser power.

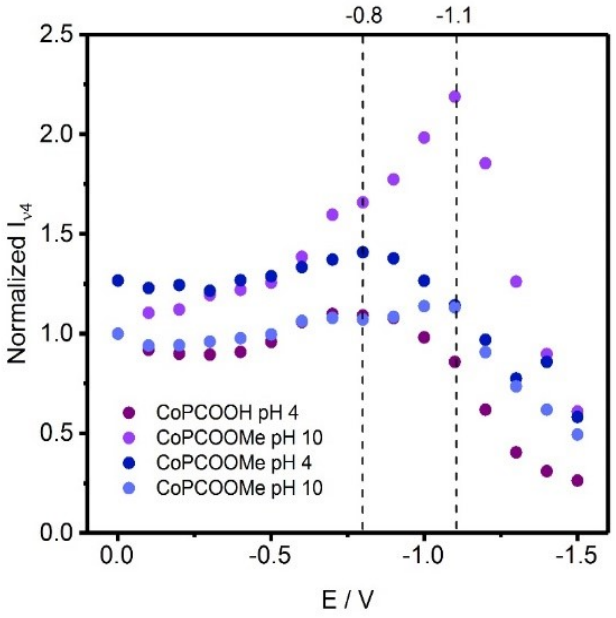

Figure 6.3.3 Potential-dependent normalized intensity of ν_4 mode obtained from SERR spectra of CoPCOOH and CoPCOOMe physisorbed on the electrode, measured at pH 4 and pH 10 conditions.

Planarity of cobalt porphyrin structure and assignment of vibrational bands

For comparison and further understanding of experimental resonance Raman spectra, quantum mechanical calculations, using DFT methods, of CoTPP structures in different oxidation states have been performed. As presented in Figure S4, CoTPP (cobalt tetraphenylporphyrin) in Co^{II} state exhibit ideal porphyrin planarity of D_{4h} symmetry, with equal perpendicular C_{meso}-C_{meso} distances. Calculated by DFT methods spectra of this state display all Raman active modes, in contrast to experimental spectra, which show dominantly the resonance enhanced ones. Hence, characteristic totally symmetric porphyrin vibrations belonging to the A_{1g} symmetry group (ν_4, ν_3, ν_2) could be assigned, with the rest of modes originating primarily from peripheral substituents of the porphyrin macrocycle. In contrast, Co^{I} state reveals distortion of porphyrin symmetry, which is as well reflected by not uniform C_{meso}-C_{meso} distances. Ruffling of the porphyrin would describe the best observed planarity change. This lowered symmetry could be represented either by C_{4v} or S_4 point group.[209,213] It is known that different features can influence such porphyrin deformations, namely size of the core size, type of substituents or axial coordination of the metal.[16,18,67,209] At this state is difficult to assume which of the parameters are responsible for the presented here porphyrin distortion. Note that the structure lacks xanthene linker, which might as well influence planarity of the porphyrin. However, the lowered symmetry of the CoTPP results in the appearance of new modes in the calculated spectra, out of which one is particularly interesting and might be a candidate for assignment of a new mode in experimental spectra. Careful inspection of the atoms displacements of this mode allowed to observe that it is mostly composed of non-totally symmetric vibrations of C_β–C_β stretches. Based on reported in literature anomalously polarized skeletal porphyrin vibrations composed of similar normal mode coordinates allows further assign it to ν_{11} B_{1g}-derived porphyrin vibration.[211]

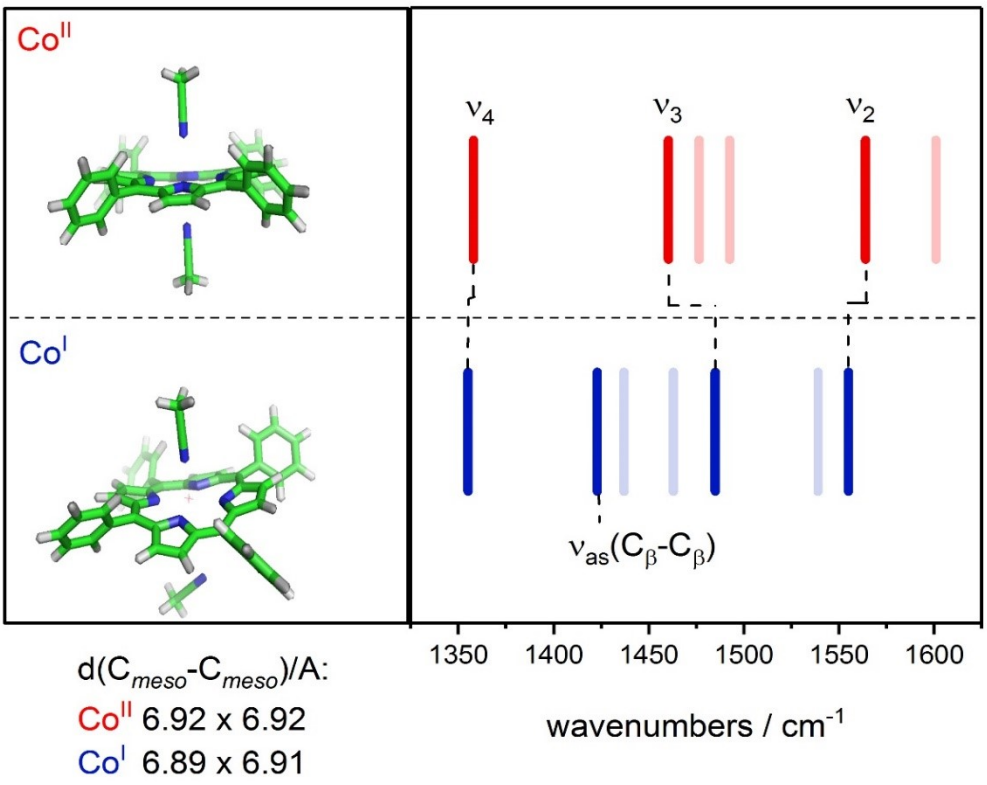

Figure 6.3.4 On the left side: optimized structures of CoTPP in Co^{II} and Co^{I} state axially coordinated by two and one acetonitrile molecules, respectively. On the right side: corresponding calculated Raman vibrational modes with indicated ν_4, ν_3, ν_2 porphyrin vibrations and new non-totally symmetric modes composed mostly of $C_\beta - C_\beta$ stretches. [7]

[7] Done by R. Goetz

ACKNOWLEDGEMENT

Firstly, I would like to thank Prof. Inez Weidinger for supervision, scientific guidance, time, considerateness and giving me the opportunity to independently conduct the research but also make my own mistakes. My sincere thanks as well to Prof. Peter Hildebrandt for giving the opportunity to join the group, support and scientific discussions.

Besides my advisors, I would like to especially thank Dr. Murat Sezer without whom I would not start this journey. Thanks for, firstly, being my 'Raman teacher', always having time to share the scientific knowledge and experience and secondly, for all the help and being a good friend in daily life.

I would like to thank my collaborators: Roland Ludwig for providing CDH samples, Holger Dobbek and his group for providing HTHP samples. Special thanks to Pierre Wrzolek and Dr. Matthias Schwalbe for synthesis of cobalt hangman compounds and pleasant collaboration.

I would like to express my acknowledgement for everyone with whom I had the opportunity to discuss my projects, especially Dr. Ingo Zebger, Prof. Ulla Wollenberger, Prof. Friedel Scheller, Prof. Maria Andrea Mroginskki, Dr. Tillman Utesch, Dr. Marius Horch

Many thanks to Dr. Uwe Kuhlmann for help with Raman equipment and lasers in the lab, Jürgen Krauss for taking care of computers, Claudia Schulz for help with ordering chemicals and Marina Böttcher for administrative help.

Thanks to all nice colleagues and friends from the lab who shared the daily lab life and contributed to home-like atmosphere: David, Christine, Halil, Dimitra, Robert, Jana, Johannes, Cathi, Kathryn, Barbara, Enrico, Michal, Christian, Marius, Francisco, Khoa, Nina, Tomos.

Thanks to Daria and Alejandra for sharing first steps in PhD life.

Special thanks to Sagie and Alex for friendship, many unforgettable moments, for sharing not only PhD-related ups and downs but an overall Berlin-related journey.

Special thanks as well to Maria for the being the best office mate which quickly turned into unique friendship, for support, all the talks, laughs and runs.

Szczególne podziękowania dla Lidii za przyjaźń i ogromne wsparcie, za wszystkie godziny na telefonie i pomoc w trzymaniu dystansu do siebie i codziennych spraw.

Szczególne podziękowania dla Jacka, za najpierw dobre rady a później przyjaźń, pomoc i wsparcie i mądrą uważność która potrafi pokazać kiedy gubię swoją drogę.

Moim siostrom, ktorym dedykuje tę pracę, Kamili i Kasi za siostrzaną miłość ktora pozwoliła mi wierzyć w niemożliwe i pokazała ze limity są tylko perspektywą. Moim rodzicom, dziękuje, za to że w calej rodzicielskiej miłości i chęci jak najlepszej dla mnie drogi umożliwili mi podejmowanie własnych decyzji i wyborów.

Statement of Authorship

I hereby declare that I am the sole author of this doctoral thesis and I have not used any sources other than those listed in the bibliography and identified as references. I further declare that I have not submitted this thesis to any other institution in order to obtain a degree.

Berlin, 10.05.2017